

PHOTOELECTRON SPECTROSCOPY OF
HIGHLY ORIENTED PYROLYTIC
GRAPHITE USING INTENSE
ULTRASHORT LASER PULSES

by

EMMA LOUISE CATTON

A thesis submitted to
The University of Birmingham
for the degree of
DOCTOR OF PHILOSOPHY

Nanoscale Physics Research Laboratory
School of Physics and Astronomy
The University of Birmingham
January 2010

UNIVERSITY OF
BIRMINGHAM

University of Birmingham Research Archive

e-theses repository

This unpublished thesis/dissertation is copyright of the author and/or third parties. The intellectual property rights of the author or third parties in respect of this work are as defined by The Copyright Designs and Patents Act 1988 or as modified by any successor legislation.

Any use made of information contained in this thesis/dissertation must be in accordance with that legislation and must be properly acknowledged. Further distribution or reproduction in any format is prohibited without the permission of the copyright holder.

Abstract

This thesis describes photoelectron emission measurements made at the surface of Highly Oriented Pyrolytic Graphite (HOPG) using ultrashort laser pulses. It concentrates on the observation and understanding of a new phenomenon whereby infrared laser pulses of just 1.5eV photon energy can be used to generate photoelectrons with kinetic energies of up to 80eV.

Intensity dependence measurements depict a highly nonlinear excitation process and for p-polarised light observations can be explained by a high-order multiphoton excitation mechanism. Comparisons with photoelectron spectra taken using XUV pulse trains show a striking resemblance suggesting that the same final states excited by multiple IR pulses can also be reached by a single XUV photon.

Interferometric autocorrelation measurements of the photoemission signal show increasingly high nonlinearity at greater photoelectron energies and a simulation of the interferometric data constructed using Optical Bloch Equations agreed with experiments showing that in the highly non-linear regime the autocorrelation shape depends almost exclusively on the nonlinearity of the excitation. XUV-IR pump-probe measurements are also presented and the technical difficulties of such measurements discussed.

Finally a novel technique of velocity map imaging of photoemission from a surface has been demonstrated for the first time at the HOPG surface.

Acknowledgements

Most importantly I am grateful to Dr. Andrey Kaplan for his support, guidance and encouragement. I would like to thank Prof. Richard Palmer for providing me with the opportunity to work on such an exciting collaborative project and also Dr. Quanmin Guo for his supervision especially during the early “STM” stages of my PhD.

I would also like to convey my appreciation to Prof. Jonathan Marangos and Dr. John Tisch for making me feel welcome during my time based at Imperial College and for their assistance and fruitful discussions.

I have been lucky to work with a number of great people during my PhD research. Special thanks must go to Dr. Miklos Lenner and to the now Dr. Christophe Huchon as well as Dr. Joe Robinson, Dr Eva Heesel and Chris Arrell who made the long days and nights in the basement lab so enjoyable. Also to Dimitri Chekulaev, Tom Roger and My Sandberg with whom I worked in Birmingham and to Neil Kilpatrick and Dr. Feng Yin.

I am grateful for the support of office-mates and friends made throughout my studies including Mi Yeon, James, Chris, Sung Jin, Fran and Ian in Birmingham and also Phil, Hank, Matthias, Thomas and Natty in London. Also to my former housemates Louise and Tanya and of course to Sarah and Dave.

I would like to thank my Dad who introduced me to science, my Mum for her continuing belief and my siblings Richard, Andrew and Mariëlla. I'd also like to thank my future in-laws the Graham family for their help and interest.

Finally my thanks go to my fiancé James for everything he has done to help me get through the last 4 years.

Contents

Abstract	i
Acknowledgements	ii
List of Figures	vii
Abbreviations	x
1 Introduction	1
1.1 The UK Attosecond Project	2
1.2 Overview of Thesis Structure	3
1.3 Author's Contribution	5
1.4 Papers Resulting from the Thesis	6
2 Background Theory	7
2.1 Ultrashort Laser Pulses	7
2.1.1 Motivation for Ultrashort Pulses	7
2.1.2 Mathematical Description of an Ultrashort Pulse	8
2.1.3 Choice of Gain Medium to Support Ultrashort Pulses	11
2.1.4 Dispersion of Ultrashort Pulses	12
2.2 Ionisation Processes in Strong Laser Fields	15
2.3 Photoemission from Surfaces	17
2.3.1 The Photoelectric Effect	17
2.3.2 Time Resolved Photoelectron Spectroscopy at Surfaces	18
2.4 Surface Plasmons and Field Enhancement	21
2.4.1 The Basic Properties of Surface Plasmons	21
2.4.2 The Derivation of Field Enhancement as a Result of Surface Plasmons	22
2.4.3 Localised Surface Plasmons	26
2.5 The Generation of High Kinetic Energy Photoelectrons at Surfaces Using Femtosecond Laser Pulses	27
2.5.1 Ponderomotive Acceleration of Electrons Mediated by Surface Plasmons	27
2.5.2 Field Enhancement	29

2.5.3	Space Charge	30
2.5.4	High Kinetic Energy Photoelectrons Observed at Insulating Materials	31
2.6	Attosecond Physics	33
2.6.1	High-order Harmonic Generation: The 3 Step Model	33
2.6.2	Attosecond Pulse Trains vs. Single Attosecond Pulses	36
2.6.3	Attosecond Measurements at Surfaces	37
2.7	Autocorrelation Techniques	40
2.8	Graphite	43
3	Photoelectron Spectroscopy of the HOPG surface	46
3.1	Introduction	46
3.2	Technical Background	47
3.2.1	The Production and Characterisation of Few Cycle Laser Pulses	47
3.2.1.1	Chirped Pulse Amplification	48
3.2.1.2	The Titanium Sapphire Laser System	50
3.2.1.3	Pulse Compression using a Hollow Fibre	52
3.2.1.4	Pulse-Characterisation by Frequency Resolved Op- tical Gating	53
3.2.2	The Production of XUV Attosecond Pulse Trains	55
3.2.3	The Surface Science Apparatus	59
3.2.3.1	The Time of Flight Mass Spectrometer	60
3.2.3.2	Surface Preparation Techniques	64
3.2.3.3	Scanning Tunnelling Microscopy	64
3.2.3.4	Ultra High Vacuum Techniques	65
3.2.4	The Attenuation of Ultrashort Pulses	67
3.3	Photoelectron Spectroscopy Measurements Using 13fs Infra Red Laser Pulses	68
3.3.1	A Description of the Photoelectron Spectra	68
3.3.2	Nonlinearity Calculations	71
3.3.3	Pulse Duration Dependence of Photoelectron Measurements from the HOPG Surface	74
3.4	Photoelectron Spectroscopy Using XUV Pulse Trains	76
3.5	Analysis and Discussion of the Photoelectron Spectra taken at the HOPG Surface	78
3.5.1	Comparisons with Band Structure	78
3.5.2	Space Charge	82
3.5.3	A Discussion of Different Excitation Mechanisms in Relation to the HOPG Photoelectron Measurements	84
3.5.4	Experimental Evidence for Field Enhancement	88
3.6	Summary and Discussion	91
4	Interferometric Measurements and Optical Bloch Simulations of Photoelectron Emission from the HOPG surface	93

4.1	Introduction	93
4.2	Interferometric Autocorrelation Measurements of the Photoemission Signal Generated by 13fs IR Pulses	95
4.2.1	Experimental Method: Interferometric Autocorrelation Mea- surements using 13fs IR Pulses	95
4.2.2	Results: Interferometric Autocorrelation Measurements us- ing 13fs IR Pulses	97
4.3	IR/XUV Pump Probe Measurements	102
4.3.1	Experimental Method: IR-XUV Pump Probe Measurements	102
4.3.2	Results and Discussion: IR-XUV Pump-Probe Measurements	105
4.4	The Optical Bloch Equations	109
4.4.1	Background	109
4.4.2	Standard Optical Bloch Equations for a Two Level System .	112
4.4.3	A Numerical Solution to the Optical Bloch Equations	116
4.4.4	The Pulse Area	118
4.4.5	Damping Terms	120
4.4.6	A Two-Level OBE Model of a Multi-Level System	122
4.5	Comparison between Experimental Data and Simulations	127
4.5.1	Modelling the Interferometric Autocorrelation of High Ki- netic Energy Photoelectrons Generated at the HOPG Sur- face using 13 fs Infra Red Pulses	127
4.5.2	An OBE Simulation of IR Pump-XUV Probe Experiment at the HOPG Surface	131
4.6	Summary and Discussion	134
4.6.1	Summary: Interferometric Autocorrelation Measurements of the Photoelectron Emission Generated at the HOPG sur- face by 13 fs IR pulses	134
4.6.2	Summary: IR Pump-XUV Probe of the HOPG Surface . . .	135
5	Velocity Map Imaging at the HOPG Surface	137
5.1	Introduction	137
5.2	Background	138
5.2.1	Ion Imaging and Velocity Map Imaging	138
5.2.2	Image Analysis Methods	139
5.2.3	The Slicing Technique	141
5.3	The Velocity Map Imaging Experimental Set-Up	141
5.3.1	The Laser System: Spitfire Regenerative Amplifier	141
5.3.2	The Experimental Beamline	142
5.3.3	VMI Detector	144
5.3.3.1	SIMION Simulations of the Paths taken by Elec- trons in The VMI Detector due to Different Elec- trostatic Potentials Applied	146
5.3.3.2	Time Gating of the VMI Detector	147
5.4	VMI Measurements at the HOPG Surface	148

5.4.1	Intensity Autocorrelation Measurements in Velocity Mapping and Microscope Imaging Modes	148
5.4.2	Intensity Dependence Measurements	151
5.5	Summary and Discussion	153
6	Conclusion	155
6.1	Chapter 3 Conclusion: Photoelectron Spectroscopy of the HOPG Surface	156
6.2	Chapter 4 Conclusion: Interferometric Measurements and Optical Bloch Simulations of Photoelectron Emission from the HOPG Surface	157
6.3	Chapter 5 Conclusion: Velocity Map Imaging of the HOPG Surface	158
6.4	Continuation of Work and Future Plans	159
A	Derivation of the Dispersion Parameter, β and the Polarisation Conditions of a Surface Plasmon Polariton at a Metal/Dielectric Interface	161
B	Second Harmonic Generation (SHG)	166
C	Estimating the Uncertainty of Experimental Measurements	168
C.1	Kinetic Energy of Electrons using Time of Flight Mass Spectrometry	168
C.2	Laser Intensity Measurements	170
	References	172

List of Figures

1.1	Summary of the UK Attosecond Technology Project	3
2.1	An Overview of Processes Occurring at Ultrafast Timescales	8
2.2	The Direct Measurement of a Light Wave	9
2.3	A Diagram of a Few Cycle Pulse	10
2.4	A Schematic to Show the Manipulation of Chirped Pulses to Create Short Pulses	14
2.5	An Illustration of Different Ionisation Processes	16
2.6	A Summary of the Different Regimes of Nonlinear Optics	17
2.7	A Schematic Representation of Time Resolved Two Photon Photoelectron Emission	19
2.8	Diagrams to Summarise the Basic Properties of Surface Plasmon Properties	22
2.9	Excitation of A Surface Plasmon	23
2.10	Surface Plasmon Assisted Photoelectron Emission: Ponderomotive Acceleration of Photoelectrons	29
2.11	Space Charge	31
2.12	High Kinetic Energy Photoelectrons Generated at Insulator Surfaces	32
2.13	A Schematic Diagram of the Semi-Classical Description of High-order Harmonic Generation	34
2.14	A Typical HHG Spectrum	35
2.15	A Summary of Excitation and Relaxation Processes in Solids on an Attosecond Timescale	38
2.16	Attosecond Measurements in Condensed Matter	40
2.17	An Overview of Intensity Autocorrelation Measurements	41
2.18	An Overview of Interferometric Autocorrelation Measurements	42
2.19	A Diagram to show the Structure of Graphite	44
2.20	The Band Structure of Graphite	45
3.1	An Overview of the Laser System at Imperial College	48
3.2	A Schematic Diagram of Chirped Pulse Amplification	49
3.3	A Diagram of the Oscillator and Stretcher	50
3.4	A Diagram of the Multi-pass Amplifier	51
3.5	A Schematic Diagram of the Differentially Pumped Hollow Fibre	52
3.6	A Diagram of the Frequency Resolved Optical Gating (FROG) Set-up used for Measurements of Pulse Duration	54

3.7	An Example of FROG measurements	55
3.8	A Diagram of the Beamline at Imperial College London	57
3.9	A Diagram of the High Order Harmonic Imaging Technique	57
3.10	Measurements of High Order Harmonics	58
3.11	A Diagram of the Surface Science Chamber	60
3.12	Time of Flight	61
3.13	An Explanation of the Attenuation of Ultrashort Pulses using Reflective Optics	68
3.14	Photoelectron Spectra Taken at the HOPG Surface Using 13 fs IR pulses with p-polarisation	69
3.15	Photoelectron Spectra Taken at the HOPG Surface Using 13fs IR pulses with s-polarisation	70
3.16	Intensity Dependence of the Photoelectron Spectra from the HOPG Surface: Nonlinearity of the Excitation Process	73
3.17	IR Photoelectron Spectra: Pulse Duration Dependence	75
3.18	Photoelectron Spectra Generated by an XUV Pulse Train	77
3.19	Comparison of Experimental Data with the Graphite Bandstructure	79
3.20	Photoelectrons Detected per Pulse at Different Laser Intensities	83
3.21	A Theoretical Study of Above-Threshold Surface Emission	86
4.1	A Schematic Diagram of the Interferometer Used for Autocorrelation Measurements	96
4.2	Photoelectron Emission Interference Autocorrelation Measurements for P-Polarised Light	98
4.3	Photoelectron Emission Interference Autocorrelation Measurements for S-Polarised Light	99
4.4	Interferometric Autocorrelation Shape: P-Polarisation	100
4.5	Interferometric Autocorrelation Shape: S-Polarisation	100
4.6	A Schematic Diagram of the Annular Interferometer used for IR-XUV Pump-Probe Experiments	104
4.7	Individual Contributions from the IR Pump and XUV Probe Pulses	106
4.8	IR/XUV Pump-Probe Measurements: Raw Data	107
4.9	IR/XUV Pump-Probe Measurements	108
4.10	Examples of OBE Simulations from the Literature	111
4.11	A Demonstration of Rabi Oscillations	117
4.12	A Demonstration of Pulse Area	119
4.13	One Pulse OBE Simulation: Lifetime Dependence	121
4.14	OBE Simulation of Interferometric Autocorrelation: Lifetime Dependence	122
4.15	One Pulse OBE Model: Nonlinearity Dependence	124
4.16	OBE Simulation of Interferometric Autocorrelation: Nonlinearity Dependence	125
4.17	Extraction of Nonlinearity From Experimental Data	128
4.18	A Comparison Between Experimental Data and OBE Simulations of Interferometric Autocorrelation Measurements	129

4.19	The Lifetime of Conduction Band States in HOPG	132
4.20	Experimental Data from IR pump-XUV Probe Measurements . . .	133
5.1	A Schematic Diagram to Show the Principle of Velocity Map Imaging	138
5.2	A Schematic Diagram of Traditional Ion Imaging Apparatus	139
5.3	A Schematic Overview of the Spitfire Laser System used for Velocity Map Imaging Experiments	142
5.4	The Experimental Beamline used for Velocity Map Imaging Mea- surements	143
5.5	A Schematic Diagram of the Velocity Map Imaging Detector	144
5.6	Simulation of Velocity Map Imaging from the HOPG Surface	146
5.7	Simulation of Microscope Mode Imaging from the HOPG Surface .	147
5.8	Comparison of Photoemission Signal from the HOPG Surface Mea- sured by the VMI Detector using two Different sets of Potentials . .	149
5.9	Intensity Autocorrelation of Photoelectrons from the HOPG Sur- face Using a Velocity Map Imaging Detector	151
5.10	Intensity Autocorrelation of Photoelectrons from the HOPG Sur- face Using a VMI Detector in Microscope Mode	152
5.11	Laser Intensity Dependence of the VMI Photoemission Signal from the HOPG Surface	153

Abbreviations

ATI	A bove T hreshold I onisation
ATP	A bove T hreshold P hotoemission
PES	P hoto- E lectron S pectroscopy
CEP	C arrier E nvelope P hase
CPA	C hirped P ulse A mplification
FROG	F requency R esolved O ptical G ating
FWHM	F ull W idth H alf M aximum
GDD	G roup D elay D ispersion
HHG	H igh-order H armonic G eneration
HOPG	H ighly O riented P yrolytic G raphite
IAC	I nterferometric A uto- C orrelation
IR	I nfra R ed
KLM	K err L ens M odelocking
LSP	L ocalised S urface P lasmon
MCP	M icro C hannel P late
NPRL	N anoscale P hysics R esearch L aboratory
OBE	O ptical B loch E quations
PEEM	P hoto- E lectron E mission M icroscopy
SHG	S econd H armonic G eneration
SPM	S elf P hase M odulation
SPP	S urface P lasmon P olariton
STM	S canning T unnelling M icroscopy
ToF	T ime o f F light
(TR)-2PPE	(T ime R esolved) 2 - P hoton P hoto- E mission
UHV	U ltra H igh V acuum
VMI	V elocity M ap I maging
XUV	e Xtreme U ltra V iolet

Chapter 1

Introduction

In order to capture and record any ‘fast’ event occurring on a short timescale it is necessary to use a tool that operates at an even shorter timescale. For example, when photographs are taken at sporting events it is common to observe blurring of fast moving objects such as a ball in the image. This occurs when the shutter speed of the camera is slower than the motion of the ball and as such it is impossible to capture the exact position of the ball at a given time.

Ultrashort pulses provide the means to measure the fundamental dynamics of nature in real time. Over the past 20 years, the widespread ability to generate pulses of femtosecond duration ($1\text{fs} = 10^{-15}$ seconds) has given rise to the field of femtochemistry [1], the real-time study of molecular dynamics and structural changes in chemical reactions that occur on femtosecond timescales. In 1999 the Nobel prize for chemistry was given to Professor Ahmed H. Zewail “for showing that it is possible with rapid laser technique to see how atoms in a molecule move during a chemical reaction” [2].

For a given power, the electric field strength of a laser pulse increases as the pulse duration decreases. Over the past decade significant developments have been made with regards to the production of these intense few-cycle laser pulses and the

understanding of their interactions with atomic systems [3]. One important result of such strong field interactions is High-order Harmonic Generation (HHG) where it has been shown that pulses of sub-femtosecond duration can be achieved by the generation of few-cycle pulses at a higher carrier frequency [4]. This discovery has underpinned the growth of “attosecond science” where the production of pulses with an attosecond duration (1 attosecond= 10^{-18} seconds) allows the measurement of electron transitions from one state to another [5].

1.1 The UK Attosecond Project

The research presented in this PhD thesis was carried out as part of the UK Attosecond Technology Project. This was a collaborative project funded by the Basic Technology Programme to produce the first source of attosecond laser pulses in the UK. The collaboration was made up of 6 different universities and institutions whose roles are summarised in Figure 1.1. The main aims of the collaboration were split into three: 1) the production of XUV (eXtreme Ultra Violet) pulses, 2) the characterisation of XUV pulses and 3) demonstration experiments. The beamline was based at the Blackett Laboratory, Imperial College London.

This thesis concentrates on research carried out between the Nanoscale Physics Research Laboratory (NPRL), University of Birmingham and Imperial College London to demonstrate the use of few-cycle infra red pulses and XUV pulse trains at surfaces. Experiments reported concentrate on photoelectron emission from the surface of Highly Oriented Pyrolytic Graphite (HOPG) and in particular to an effect observed whereby photoelectrons with kinetic energies of up to 80 eV could be generated by infrared photons of just 1.5 eV.

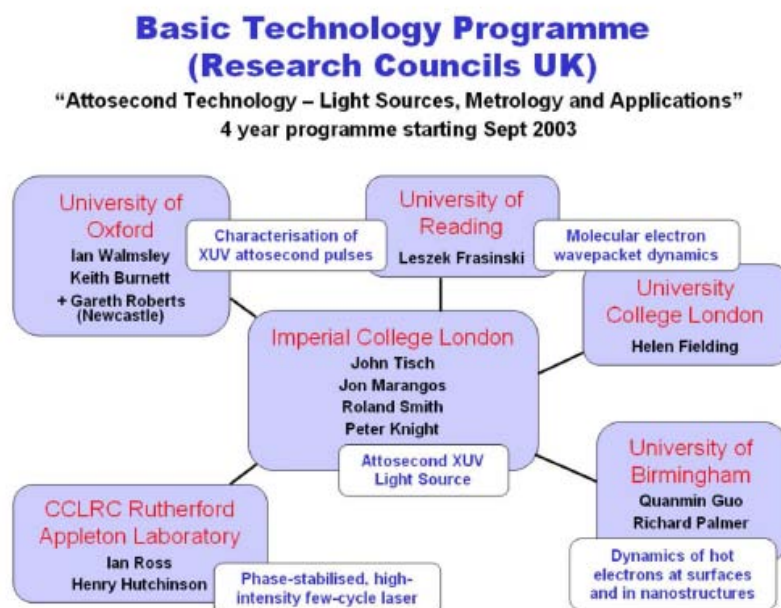


FIGURE 1.1: Summary of the UK Attosecond Technology Project: A collaboration of six universities and research institutions to work towards the production, measurements and demonstration of attosecond duration pulses (figure taken from the original project plan).

1.2 Overview of Thesis Structure

Following on from this introduction chapter, Chapter 2 outlines the relevant background theory required for a full understanding of the experiments carried out including: few-cycle laser pulses, the production of attosecond pulses, the HOPG surface and strong field effects occurring at laser-surface interactions.

As previously discussed the main emphasis of this thesis is placed on work carried out at Imperial College London. This data is presented in Chapter 3 and Chapter 4.

Chapter 3 is entitled “Photoelectron Spectroscopy of the HOPG Surface”. A technical background section describes the experimental apparatus and special techniques used. Photoelectron emission spectra taken from the HOPG surface are then presented. It is found that infra red (IR) pulses of just 1.5 eV energy can

be used to generate photoelectrons with surprisingly high kinetic energies of up to 80 eV. Intensity dependence measurements are presented and found to depict a highly non-linear excitation process. The polarisation dependence of photoelectrons generated at the surface is also presented. For p-polarised light the kinetic energies of electrons measured match up with nonlinearity estimates calculated from the intensity dependence measurements so that the high kinetic energy photoelectrons can be explained by a high-order multiphoton excitation mechanism. For s-polarised light however it is thought that competing excitation processes such as tunnel ionisation or thermal effects also contribute to the signal. Relevant strong field phenomena such as space charge and ponderomotive acceleration are also discussed. Comparisons between photoelectron spectra generated by IR pulses and those taken by XUV pulse trains aid identification of the conduction band states excited. It appears that the same states accessed by single-photon excitation by XUV photon can also be probed by the high-order IR multi-photon process in the strong-field regime suggesting some kind of final-state selection effect.

Chapter 4 is entitled “Interferometric Measurements and Optical Bloch Simulations of Photoelectron Emission from the HOPG Surface”. This chapter concentrates on time-dependent photoelectron measurements at the HOPG surface. Firstly interferometric autocorrelation (IAC) measurements of the photoemission signal generated by 1.5 eV IR pulses are presented. The autocorrelation shape produced is found to vary with increasing photoelectron kinetic energy with the regions of high kinetic energy displaying high orders of nonlinearity. An initial attempt at an IR pump-XUV probe experiment is also presented where it is shown that an XUV pulse can be used to probe the excitation by the IR pulse of low lying states below the vacuum level. Experimental difficulties overcome and potential improvements to the beamline are also discussed. In the final part of chapter 4, the Optical Bloch Equations (OBE) have been used to model laser interactions

at the surface. The method used to create the model is explained including the incorporation of the high orders of suspected multi-photon transitions observed experimentally. Simulations are then compared to both the IAC data and also to the XUV-IR experiment.

Chapter 5 presents some additional data taken at the NPRL laboratory in Birmingham. Velocity map imaging of photoemission from the HOPG surface has been demonstrated and it can be seen that photoelectrons are emitted at angles of up to 30 degrees from the HOPG surface. This is the first time, to the authors knowledge that such measurements have been made at a surface. A demonstration is given of different modes of operation of the detector along with simulations. Where possible, comparisons are made with the photoelectron spectroscopy data taken at Imperial College (described in Chapter 3 and 4)

Finally overall conclusions are presented for each chapter along with a discussion of how the research could progress in the future.

1.3 Author's Contribution

All data presented in this thesis have been taken by myself with assistance from various other collaboration members. All plots made and analysis carried out have been done by myself unless otherwise referenced. Where computer programs used have been written by other members of the collaboration it has been stated in the text.

The beamline at Imperial College was built by Dr. Joseph Robinson and Dr. Charles Haworth and the surface science system initially assembled by Dr. Christophe Huchon.

1.4 Papers Resulting from the Thesis

Band structure effects in highly non-linear photoelectron emission from graphite with femtosecond laser pulses

Emma L. Catton, Andrey Kaplan, Joseph S. Robinson, Miklos Lenner, Christophe Huchon, Christopher Arrell, Jonathan P. Marangos, John W. G. Tisch and Richard E. Palmer

Re-draft in preparation following rejection by Physical Review Letters

Interferometric studies of high kinetic energy electron emission generated by intense few-cycle laser pulses

Emma L. Catton, Andrey Kaplan, Joseph S. Robinson, Miklos Lenner, Christophe Huchon, Christopher Arrell, Jonathan P. Marangos, John W. G. Tisch and Richard E. Palmer

Final draft in preparation

Chapter 2

Background Theory

2.1 Ultrashort Laser Pulses

2.1.1 Motivation for Ultrashort Pulses

Improvements in laser technology have paved the way for the production of increasingly shorter pulses [6]. As the temporal duration of pulses that can be achieved is reduced, the time resolution with which molecular, atomic or electronic processes can be probed is improved, opening up doors to new areas of science that can be studied in real-time. Fig. 2.1 shows the characteristic lifetimes of various processes that can be studied using ultrashort pulses.

In the past ten years significant developments have been made and the “femtosecond barrier” has been broken [3]. The production of pulses with sub-femtosecond durations has led to the ability to investigate the electronic motion occurring at these ultrashort timescales, giving rise to the field collectively known as “attosecond science” [7] or “attosecond physics” [5]. Key measurements made to date include the measurement in real time of an atomic core hole [8], the direct measurement of a light wave [9] (summarised in Fig. 2.2) and more recently the first

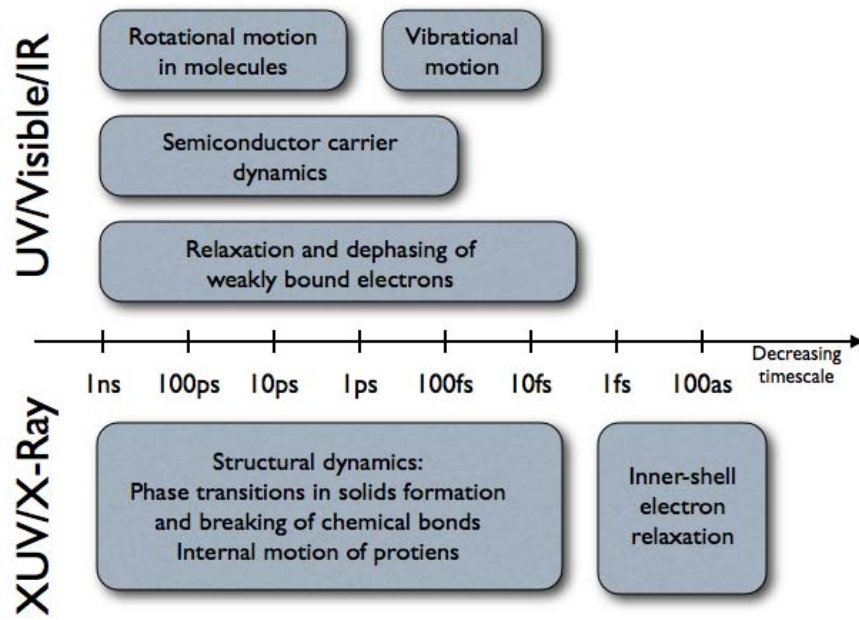


FIGURE 2.1: Ultrafast Timescales: A summary of the characteristic lifetimes of various processes that can be probed using light pulses in either the UV/Visible/IR regime or using XUV/X-Rays (adapted from[6])

attosecond measurements made at a solid which will be discussed in more detail on page 37 [10, 11].

2.1.2 Mathematical Description of an Ultrashort Pulse

An ultrashort pulse travelling in the z direction may be described by Eq. 2.1 where the term $A(z,t)$ contains a description of the pulse envelope, ω is the frequency of the carrier wave, k is the wavenumber ($k = 2\pi/\lambda$) and ϕ_0 is the Carrier-Envelope phase (CEP) [6].

$$E(z, t) = A(z, t)e^{i(\omega t - kz + \phi_0)} \quad (2.1)$$

The pulse envelope is usually assumed to be Gaussian in shape whereby the temporal intensity profile can be given by $e^{-\frac{2t^2}{\Delta t_P^2}}$ [12]. An example of such a pulse with

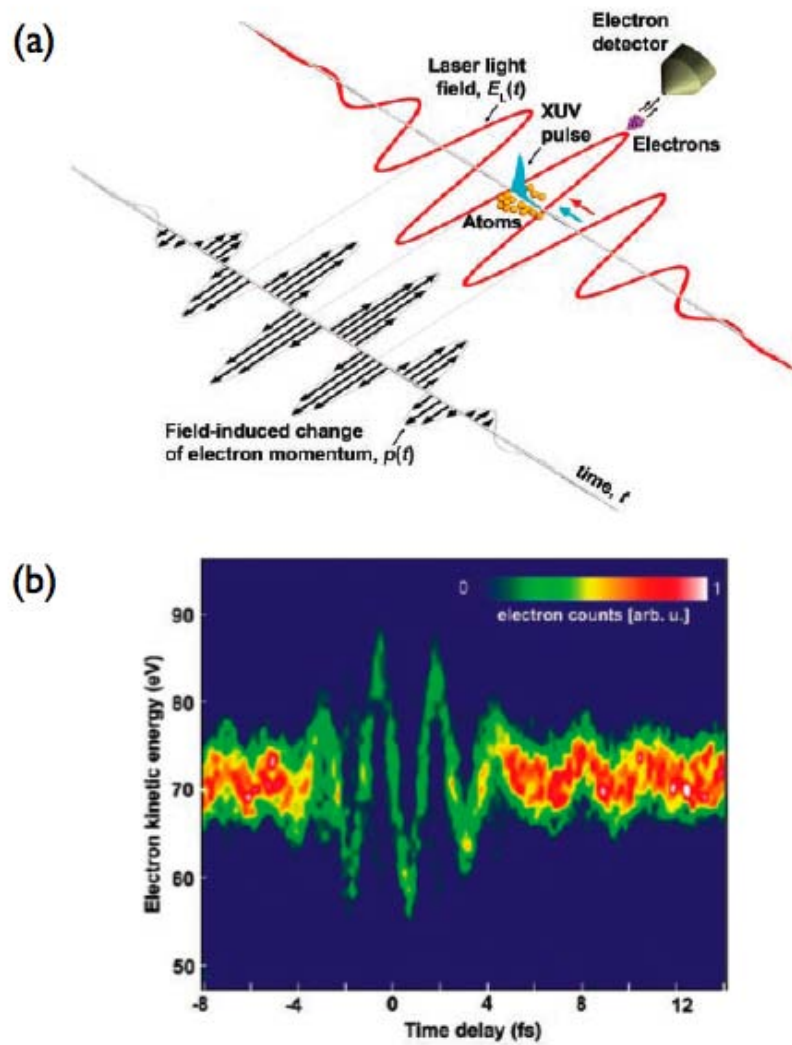


FIGURE 2.2: [9] Direct Measurement of a Light Wave (a) Experimental method: photoelectrons generated in neon gas by a 93 eV (250 attosecond) single pulse are measured in the presence of a sub 5 fs 750 nm infra red pulse as a function of pump-probe delay between the two pulses (b) The photoelectrons measured experience a shift in kinetic energy due to the presence of the IR field. This kinetic energy shift directly represents the amplitude of the IR laser pulse.

a duration of 8 fs (3 cycles) is shown in Fig. 2.3.

The carrier-envelope phase, ϕ_0 , as shown in Figure 2.3 is given by the difference in time between the maxima of the carrier and that of the envelope.

For ease of use in derivations it is common [13] to define the temporal phase, $\phi(z, t)$ as:

$$\phi(z, t) = \omega t - kz + \phi_0 \quad (2.2)$$

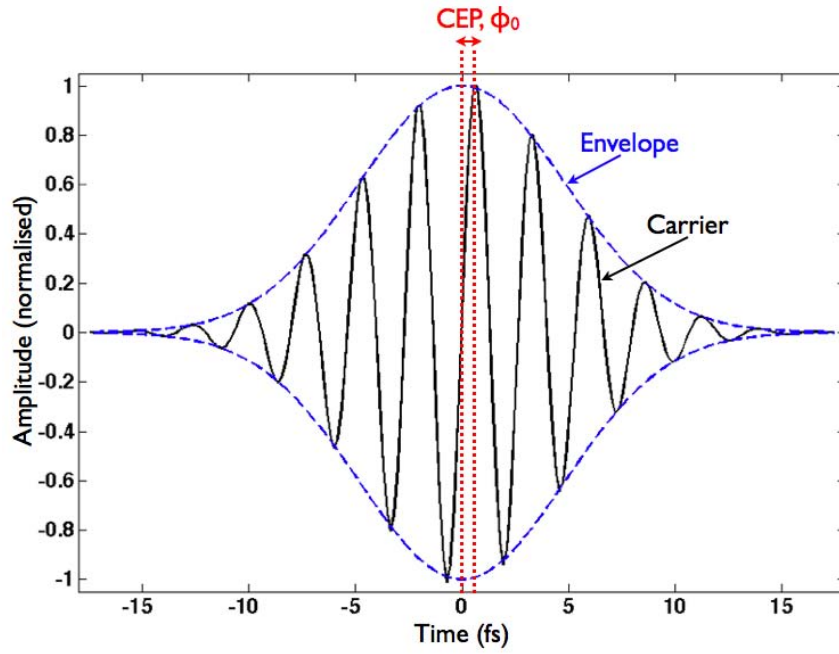


FIGURE 2.3: A Diagram of a 3-cycle (8 fs at 800 nm) Pulse: The phase difference between the Carrier and Envelope is given by Φ , the Carrier-Envelope Phase

where $\phi(z, t)$ describes the changes in carrier frequency over time, so Eq. 2.1 can simply be written as:

$$E(z, t) = A(z, t)e^{i\phi(z, t)} \quad (2.3)$$

The instantaneous frequency can be calculated from the differential of the temporal phase to give:

$$\omega(z, t) = \frac{d\phi(z, t)}{dt} \quad (2.4)$$

For a fuller understanding of the behaviour of ultrashort pulses and the way in which they can be manipulated it can be useful to describe the pulse in the spectral domain. The temporal and spectral descriptions are related by the Fourier and inverse Fourier transforms:

$$E(t) = \frac{1}{2\pi} \int_{-\infty}^{+\infty} E(\omega) e^{-i\omega t} d\omega \quad (2.5)$$

$$E(\omega) = \int_{-\infty}^{+\infty} E(t) e^{i\omega t} dt \quad (2.6)$$

From this relationship it can be shown [14] that the spectral width of the pulse, $\Delta\omega$ and the pulse duration Δt can be combined to give the inequality $\Delta t \Delta\omega \geq \frac{1}{2}$. As it is easier in the laboratory to measure the FWHM of the frequency spectrum, $\Delta\nu$ and the FWHM of the pulse duration, Δt , the relationship is often quoted as the time-bandwidth product, TBP where $TBP = \Delta t \Delta\omega$ and its value depends on the pulse shape used (TBP = 0.441 for a Gaussian pulse shape, 0.315 for a *sech*² pulse and 0.886 for a square pulse). When the inequality is satisfied i.e. when the pulse duration is as short as the spectral profile will allow, the pulse is said to be transform limited.

Where Equation 2.1 gave a description of the pulse in the temporal domain, the pulse can similarly be described in the spectral domain by Equation 2.7, where $A(z, \omega) \propto e^{-\frac{\ln(16)\omega^2}{\Delta\omega^2}}$ and $\phi(z, \omega)$ is the spectral phase.

$$E(z, \omega) = A(z, \omega) e^{i\phi(z, \omega)} \quad (2.7)$$

2.1.3 Choice of Gain Medium to Support Ultrashort Pulses

Commercial lasers that can output pulses of ~ 30 fs duration are now readily available. The generation of such short pulses can be attributed to the properties of the gain medium chosen, usually Titanium Sapphire $\text{Ti:Al}_2\text{O}_3$, a sapphire (Al_2O_3) crystal doped with titanium so that Ti^{3+} ions replace some of the Al^{3+} ions. The

titanium sapphire lasers used in the experimental work of this thesis are described in much more detail in experimental chapters 3 and 5.

The large gain bandwidth (the range of frequencies over which optical amplification can take place) is the primary feature of $\text{Ti:Al}_2\text{O}_3$ that makes it so suitable for the generation of ultrashort pulses [15]. When irradiated with visible light, the absorption band is extremely wide, ranging from ~ 450 nm - 600 nm with a peak at around 500 nm (A pump laser lying in the blue-green part of the visible spectrum is chosen to excite the medium). The unusually broad range in photon energies which can be absorbed occurs due to electric field effects that are caused by the bigger size of the Ti ions as compared to the original Al ions [16].

The emission band of the medium, centred at 750 nm, is also extremely broad with a width of 200 nm. This large bandwidth is the essential factor for the generation of such short pulses due to the time-bandwidth product. Another advantage of $\text{Ti:Al}_2\text{O}_3$ as a gain medium is that sapphire has good thermal conductivity, this means that at the high peak powers of the pump lasers used, thermal effects do not present a problem.

2.1.4 Dispersion of Ultrashort Pulses

From the definition of the time-bandwidth product, a pulse with an ultrashort duration will have a large spectral bandwidth. Great care has to be taken when choosing suitable optics for the short pulses as the propagation through any optical medium can vary for different wavelength components and can therefore lead to significant changes in the profile of the pulse and its duration.

It is possible to describe the dispersion of a pulse in a medium using the spectral phase which can be expanded by the following Taylor expansion around a central reference frequency, ω_0 and where n is an integer [13]:

$$\phi(\omega) = \phi_0 + \sum_{n=1}^{\infty} \frac{1}{n!} \left. \frac{d^n \phi(\omega)}{d\omega^n} \right|_{\omega_0} (\omega - \omega_0)^n \quad (2.8)$$

The first term in the expansion, ϕ_0 is the Carrier-Envelope Phase (CEP). Whilst this can be important in experiments using few-cycle pulses [17] it does not contribute to dispersion of the pulse as it does not change the pulse shape.

The second term in the expansion is the group delay $\left(\left. \frac{d\phi(\omega)}{d\omega} \right|_{\omega_0} \right)$ which describes the time taken for the pulse to propagate through the material. The group delay is given by the propagation distance divided by the group velocity v_G where:

$$v_G(\omega) = \left(\frac{dk}{d\omega} \right)^{-1} \quad (2.9)$$

The third term in the expansion, $\left(\left. \frac{d^2 \phi(\omega)}{d\omega^2} \right|_{\omega_0} \right)$ is commonly known as the group delay dispersion (GDD) (although is sometimes referred to as second-order dispersion). It describes the rate at which a pulse is stretched as it propagates through a medium due to different spectral components of the pulse propagating at different group velocities. GDD is dependent on the material through which the pulse is travelling and is measured in fs^2 . The effect that GDD has on a pulse propagating through a medium is given by equation 2.10 where τ_i is the initial pulse duration before the wavepacket enters the medium and τ_f the duration afterwards [15].

$$\tau_f = \tau_i \sqrt{1 + \left(4 \ln 2 \frac{GDD}{\tau_i^2} \right)^2} \approx 4 \ln 2 \frac{GDD}{\tau_i} \quad (2.10)$$

For IR pulses travelling through an optical medium such as silica the GDD will have a positive value, indicating that shorter wavelengths will be delayed relative to longer wavelengths. If the instantaneous frequency of a pulse (the derivative of the phase with respect to time as seen in Equation 2.4) varies as a linear function of time then the pulse is described as being ‘‘chirped’’ where a positive GDD will

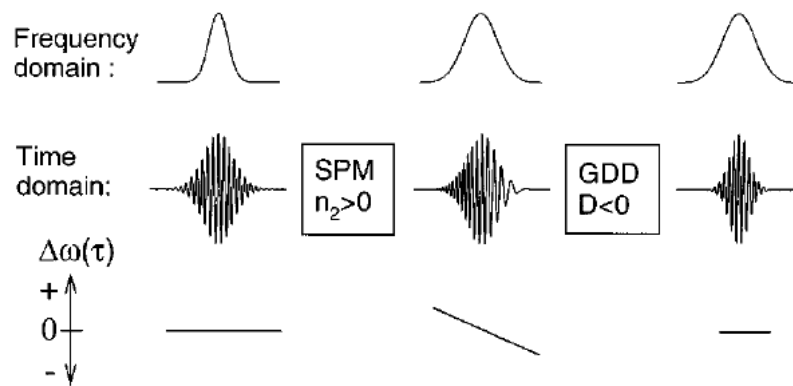


FIGURE 2.4: Manipulation of Chirped Pulses to Create Short Pulses: A schematic showing a transform limited pulse which is broadened by Self Phase Modulation (SPM) resulting in down-chirp of the pulse. The chirp is then compensated for by transmission through an optical media such as a prism pair which introduces negative Group Delay Dispersion (GDD) The end result is a temporally compressed pulse. Figure taken from [6]

introduce an up-chirp meaning that the instantaneous frequency increases with time. Optical components such as prism pairs, grating pairs and chirped mirrors can be used to apply negative GDD to a pulse and therefore to compress it in time. To some extent this can be used to pre-compensate for unavoidable dispersive optics placed in the beam path. As pulses become shorter and therefore have a greater bandwidth dispersion effects will increase, for example, a 30 fs pulse travelling through 580 cm air and 0.3 cm glass will be stretched to 38 fs. For an 8 fs pulse travelling the same path the resulting pulse will have stretched to 78 fs [18]. Control of the GDD is the underlying mechanism behind the production of ultrashort laser pulses using Chirped Pulse Amplification and must also be an important consideration during experiments in order to preserve the time resolution of the pulse. Fig. 2.4 shows a schematic representation of the pulse compression of a transform limited pulse achieved via the exploitation of dispersion effects. Further details of the experimental methods used are given in Chapter 3.

2.2 Ionisation Processes in Strong Laser Fields

Ionisation of an atomic system by an intense laser (and therefore in the presence of a strong electric field) may be described by different processes depending on the intensity of laser used.

At intensities of around 10^{12} W/cm² to 10^{13} W/cm² a multiphoton process will dominate where multiple photons are absorbed by a bound electron until it has been given enough energy to escape the potential. If excess photons are absorbed the photoelectron will leave the potential with excess energy. A schematic of the process is shown in Figure 2.5 (a)). If the same initial state of a system is excited by different multiples of the number of photons then the resulting photoelectron spectrum will contain repeated features, separated by the energy of the photon that are known as Above Threshold Ionisation (ATI) peaks.

At higher laser intensities of roughly 10^{14} W/cm² to 10^{15} W/cm² for atomic systems, the dominant excitation mechanism will be tunnel ionisation. A schematic of the process is shown in Figure 2.5 (b). At these field strengths the presence of the electric field will cause a distortion of the atomic potential (shown by the solid black line in Figure 2.5) until a potential barrier is formed. It is then possible for some of the wave packet to tunnel out into the continuum. The onset of such behaviour marks the start of the Strong Field regime [6]. At even higher laser intensities the atomic potential will become distorted to such an extent that there is no longer a barrier present and the electron may escape, a process known as above threshold ionisation. In contrast to the photoelectron spectrum with a periodic structure (ATI) generated by multiphoton ionisation the spectrum produced in the case of tunnel ionisation is expected to be smoother in appearance [19].

The Keldysh parameter γ , may be used to distinguish between the two regimes [20, 21], and is given by given by Equation 2.11 where I_p is the ionisation potential,

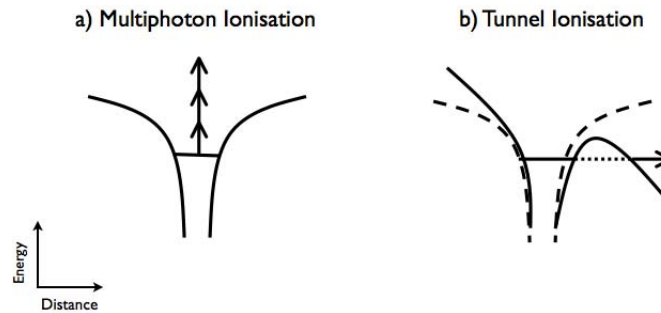


FIGURE 2.5: Ionisation Processes: a) Multiphoton ionisation: an electron bound in a potential may absorb multiple photons giving it enough energy to escape b) Tunnel ionisation: in the strong field regime the potential in which the electron is bound may become distorted forming a potential barrier through which the electron wavepacket can tunnel to escape.

m_e is the electron mass, ω the laser frequency, and E is the electric field amplitude. It is derived from the ratio of the binding potential (the work function for a solid and ionisation potential for a gas) and the quiver energy (potential energy gained in the E-Field). If the quiver energy is much less than the binding potential then a perturbative approach is valid [22] i.e. a value of $\gamma \ll 1$ or $\gamma \gg 1$ would indicate that the transition lies in the tunnelling or multiphoton regime respectively. It has however recently been shown that the two regimes may overlap [23] and are not mutually exclusive.

$$\gamma = \frac{\omega}{E} \frac{\sqrt{2m_e I_p}}{e} \quad (2.11)$$

Since γ is dependent on the laser pulse duration it is more likely that the tunnelling regime can be reached at intensities below the damage threshold of the surface if the pulses are ultrashort. Figure 2.6 shows a summary of the different regimes according to the laser intensities used.

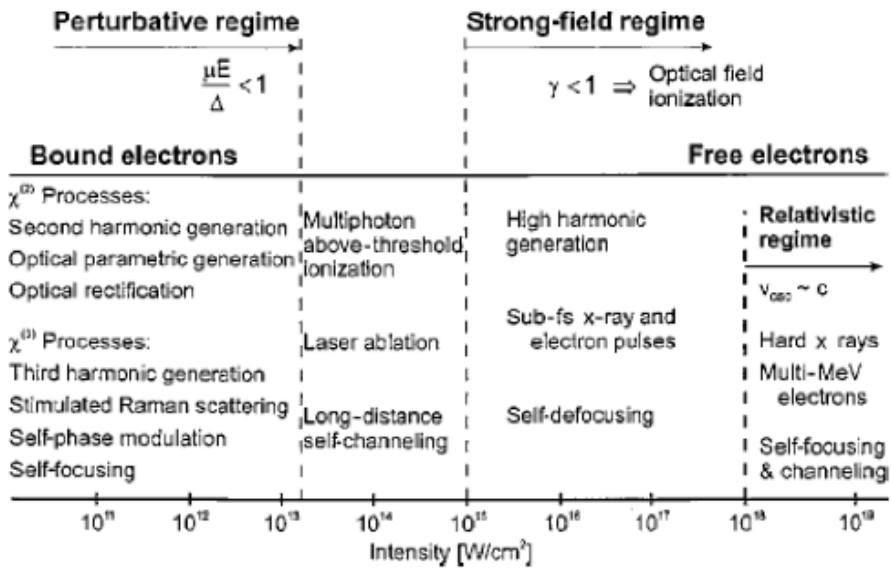


FIGURE 2.6: Regimes of Nonlinear Optics: An illustration of the different nonlinear effects observed with respect to laser intensity. The boundaries shown are for guidance and do not represent a sharp cut off. For the strong field regime shown the intensities correspond to visible and near-infrared light. (figure taken from [6])

2.3 Photoemission from Surfaces

2.3.1 The Photoelectric Effect

When a surface is illuminated by photons of known energies the distribution of the kinetic energies of photoelectrons emitted provides direct information about it's electronic structure. The binding energy E_B of an electron can be extracted from the measured kinetic energy using Einstein's photoelectric equation:

$$E_K = h\nu - E_B - \phi \quad (2.12)$$

where $h\nu$ is the energy of the photon and ϕ is the work function.

The type of surface states that can be probed by the photons will depend on their wavelength. Ultraviolet Photoelectron Spectroscopy (UPS) [24] is used to study

valence band states whereas the states that can be probed by X-Ray Photoelectron Spectroscopy (XPS) range from the valence band to core levels [25]. Clearly for the laser based PES experiments reported in this thesis the XUV pulses will be able to probe states which lie further into the valence band than infrared pulses will however it should also be noted that IR light has a penetration depth on a micron scale and so the PES will contain contributions from the bulk as well as the surface. For XUV wavelengths all photoelectrons will be generated from the upper layers of the surface.

In order to obtain a good energy resolution it is important that the photons are monochromatic. The ease of interpretation of the photoelectron spectrum depends on the bandstructure of the surface of interest. In some cases which are harder to analyse the kinetic energy spectrum will correspond to a map of the energy levels and density of states of both the valence band and the conduction band.

2.3.2 Time Resolved Photoelectron Spectroscopy at Surfaces

Two-Photon Photoemission (2PPE) has proved to be a popular technique over the past two decades combining the ability to measure excited state energies by standard photoemission techniques with measurements of the lifetimes of the states [26, 27, 28].

Uses of the technique have included the measurements of excited surface states and image potential states [29, 30, 31, 32], coherent excitation of wave packets [33], observation of polarization effects [34] and electronic states of molecular adsorbates on surfaces [35].

In 2PPE electrons are excited from an initial state lying below the Fermi level by the first photon (the pump pulse) to an intermediate state and then the second

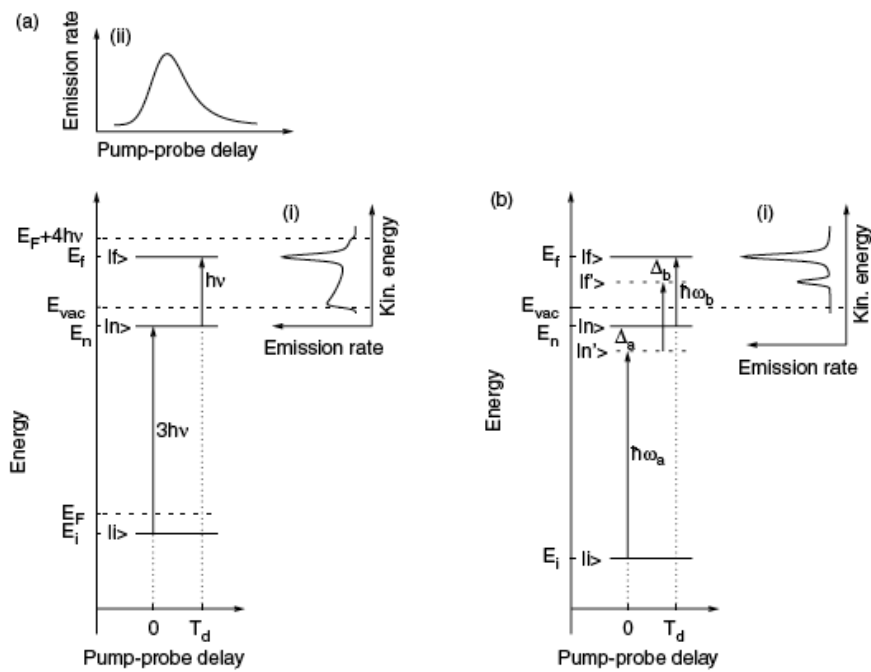


FIGURE 2.7: Schematic Representation of Time Resolved Two Photon Photoelectron Emission: (a) An electron is excited by a pump pulse (in this case with energy $3h\nu$) from an initial state $|i\rangle$ to an intermediate state $|n\rangle$ and then from $|n\rangle$ to a final state $|f\rangle$ by a probe pulse ($h\nu$). Photoelectron spectra can be taken in two ways (i) at a constant pump-probe delay as a function of kinetic energy (ii) at a fixed kinetic energy as a function of pump-probe delay. (b) A diagram to show the general model used to calculate the 2PPE spectra (of the experiment shown in part (a)) where Δ_a and Δ_b are finite detuning of the relevant states. Figure taken from [27].

photon (the probe pulse) further excites it to a state above the Fermi level from which it can be detected. Because of the nature of this second order process, where it is the intermediate level that is being probed, the energies of states that can be studied are limited as it is only possible to probe those unoccupied surface states that are found above the Fermi level but below the vacuum level. The two photons used are of different energies, their wavelength can be chosen to a certain extent by frequency doubling or tripling of the initial pulse [27].

Figure 2.7 shows a schematic of the 2PPE method which can be separated into two variations: Energy resolved 2PPE involves taking the photoelectron spectrum at a fixed pump-probe delay time over all kinetic energies (labelled (i) in Figure

2.7 (a)). For time resolved 2PPE (TR-2PPE) on the other hand, electrons are recorded at a fixed kinetic energy as a function of pump-probe delay (labelled (ii) in Figure 2.7 (a)).

The width of a pump-probe spectra will depend not only on the population lifetime of the excited state but also on scattering effects. Scattering processes will result in a decay of coherence, for inelastic scattering this will result in a decay of the population itself, whereas quasidelectric scattering is defined as that which destroys phase coherence whilst leaving the population of an excited state unchanged. The overall dephasing rate can be extracted from the linewidth of an energy dependent 2PPE measurement [36]. Accurate extraction of lifetime parameters from the experimental data, can be achieved by comparison of the experimental spectrum with a model of the excitation process, usually simulated using solutions of the Optical Bloch Equations (OBE) [34, 36, 37]. It is even possible for excited state lifetimes shorter than the pulse duration to be extracted [31]. A full explanation of the OBE's including different decay parameters is given in Chapter 4.

Although TR-2PPE is a popular method for measuring femtosecond-scale lifetimes, at present it is not transferable to shorter (sub fs) measurements because both the pump and the probe pulse must have a duration smaller than the process to be probed. At present it is not technically possible to produce two such isolated pulses of attosecond duration that can be delayed with respect to each other so less direct methods such as “attosecond streaking” are necessary [10].

2.4 Surface Plasmons and Field Enhancement

2.4.1 The Basic Properties of Surface Plasmons

This section describes the theory of surface plasmons and field enhancement which will later prove to be an important consideration when interpreting experimental observations of photoelectrons with high kinetic energies generated at a surface. A surface plasmon polariton is an electromagnetic wave that propagates along the interface between a conductor and a dielectric. When an incident light wave is coupled to a surface plasmon mode the free electrons at the surface of the conductor will oscillate collectively at the frequency of the incident light wave [38, 39]. Using Maxwell's equations and appropriate boundary conditions it can be shown (Appendix 1) that only p-polarised light can be coupled to surface plasmons.

The wave vector k_{SP} for a surface plasmon can also be derived from Maxwell's Equations (Appendix 1) and is frequency dependent [39]:

$$k_{SP} = \frac{\omega}{c} \left(\frac{\epsilon_1 \epsilon_2}{\epsilon_1 + \epsilon_2} \right)^{1/2} \quad (2.13)$$

where ϵ_1 is the dielectric constant of the dielectric e.g. air and ϵ_2 is the dielectric constant of the conductor, usually a metal.

This is shown in Figure 2.8 (c) compared to the linear wave vector of a free photon. In order for a light wave (with wave vector, k) to be coupled to a SP the momentum mismatch between the two has to be solved. Two such methods of phase-matching are prism coupling [40] which makes use of the higher dielectric constant of a glass prism (the in-plane momentum of the metal is $k_x = k\sqrt{\epsilon} \sin \theta$), and grating coupling [41] where a grating with a lattice spacing = a is patterned onto a surface and phase matching achieved when $k_{SP} = k \sin \theta \pm n\frac{2\pi}{a}$ (n is the

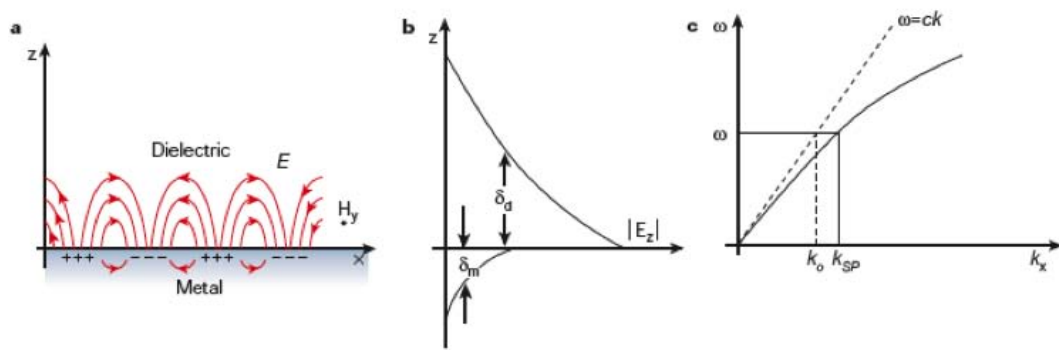


FIGURE 2.8: Schematic diagram showing the basic properties of a surface plasmon. (a) The plasmon wave is transverse magnetic (TM) where \mathbf{H} is in the y direction and the electric field is normal to the surface. The E -field component is enhanced close to the surface and decays exponentially with increasing distance in the z direction. (b) The decay length δ_d of the electric field away from the metal surface is $\sim 0.5 \times$ the wavelength of the incident light whereas the decay length into the metal (δ_m) is much less, determined by the skin depth of the material, this is the cause of the enhanced E -field field. (c) The solid line shows the dispersion curve for a surface plasmon mode compared to a free photon (dashed line). The momentum mismatch between the two at a single frequency is shown. This must be overcome in order to couple the light to a plasmon mode. Figure taken from [38]

order; 1, 2, 3... and g is the grating parameter $g = 2\pi/a$ where a is the periodicity of the grating).

2.4.2 The Derivation of Field Enhancement as a Result of Surface Plasmons

The following derivation (taken from [42]) shows that the excitation of plasmons at a metal surface by p-polarised light can produce a significant enhancement in the optical electric field. This is significant at strong laser intensities as a field enhancement of a few orders of magnitude can result in different behaviour of the surface [43, 44, 45].

Figure 2.9 is a schematic diagram of the coupling process. It is assumed for this derivation that the plasmons are excited at an air/metal interface. The dielectric

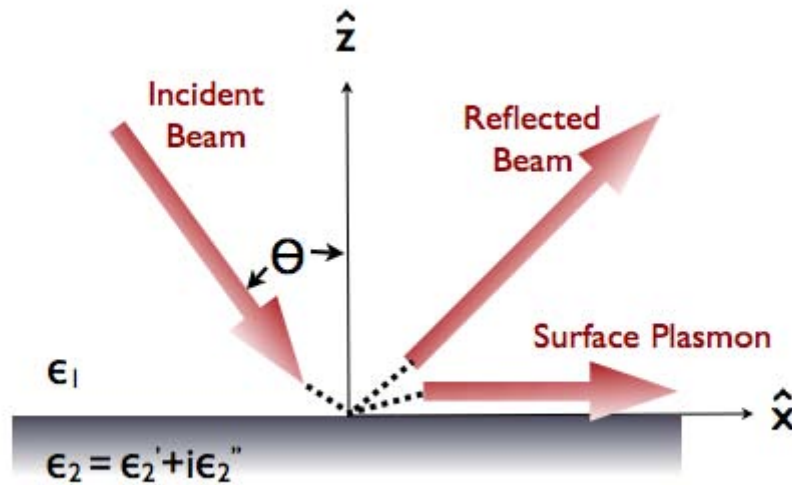


FIGURE 2.9: Excitation of A Surface Plasmon: Schematic diagram to show the excitation of a surface plasmon using a coupler (dashed lines) such as a prism or a grating including random surface roughness. In this case the upper medium e.g. air has a real dielectric constant ϵ_1 whereas the solid medium (e.g. a metal) has a complex dielectric constant defined as $\epsilon_2 = \epsilon_2' + i\epsilon_2''$ (figure and caption adapted from [42])

constant of the air is real and is given by ϵ_1 but that of the metal is complex and can be defined as $\epsilon_2 = \epsilon_2' + i\epsilon_2''$. For a propagating surface mode the conditions $\epsilon_2' < -\epsilon_1$ and $\epsilon_2'' \ll -\epsilon_2'$ must be valid. The derivation does not depend on the type of coupler (depicted in Figure 2.9 as the dashed black line) and is therefore valid for coupling by random surface roughness.

Assuming a very small amount of intrinsic damping, the effect of the optimised coupler will be small and therefore can be ignored so that the electromagnetic fields of an excited surface plasmon mode propagating in the x direction can be given by Equation 2.14 and Equation 2.15 where \mathbf{E} is the electric field, \mathbf{H} is the magnetic field and H_y the magnetic field component in the y direction.

$$\mathbf{H}_{SP} = H_y \hat{y} \exp[i(k_{SP}x - \omega t)] \begin{cases} \exp(-q_1 z) & \text{if } z > 0 \\ \exp(+q_2 z) & \text{if } z < 0 \end{cases} \quad (2.14)$$

$$\mathbf{E}_{SP} = \frac{cH_y}{\omega} \exp[i(k_{SP}x - \omega t)] \begin{cases} (iq_1\hat{x} - k_{SP}\hat{z})\exp(-q_1z)/\epsilon_1 & \text{if } z > 0 \\ (-iq_2\hat{x} - k_{SP}\hat{z})\exp(+q_2z)/\epsilon_2 & \text{if } z < 0 \end{cases} \quad (2.15)$$

k_{SP} and q_i are given by Equation 2.16 and Equation 2.17 and their real components satisfy $\Re(k_{SP}), \Re(q_i) > 0$.

$$k_{SP} = \frac{\omega}{c} \left(\frac{\epsilon_1\epsilon_2}{\epsilon_1 + \epsilon_2} \right)^{1/2} \quad (2.16)$$

$$q_i = \frac{\omega}{c} \left(\frac{-\epsilon_i^2}{\epsilon_1 + \epsilon_2} \right)^{1/2} \quad (2.17)$$

The time-averaged power flow per unit length in the y direction (i.e. perpendicular to the direction of propagation) can be calculated using Equations 2.14-2.17 by:

$$\mathcal{P}_{SP} = \frac{c}{8\pi} \int_{-\infty}^{+\infty} dz \Re\{\mathbf{E}_{SP} \times \mathbf{H}_{SP}^*\} \cdot \hat{x} \quad (2.18)$$

Which gives the following where $\mathbf{E}_{SP}(0^+)$ is the electric vector just outside of the surface.

$$\mathcal{P}_{SP} = \frac{\omega\epsilon_1}{16\pi} \frac{|\mathbf{E}_{SP}(0^+)|^2}{|q_1|^2 + |k_{SP}|^2} \Re\left\{ \frac{k_{SP}(\epsilon_1 q_1' + \epsilon_2 q_2')}{\epsilon_2 q_1' q_2'} \right\} \quad (2.19)$$

Throughout this derivation a prime indicates a real component and a double prime indicates an imaginary component. The power dissipated in the ‘metal’ by the plasmon mode per unit area is given as by Equation 2.20 where the power attenuation coefficient, $\alpha = 2k_{SP}$.

$$-\frac{d\mathcal{P}_{SP}}{dx} = \alpha\mathcal{P}_{SP} \quad (2.20)$$

Next the net power added to the metal per unit area by coupling of the light wave i.e. the intensity must be considered. This is given by Equation 2.21 where \mathbf{E}_0 is the electric vector of the incident beam and R is the power reflectance.

If a steady-state system is assumed then Equation 2.20 and Equation 2.21 should be balanced:

$$I = \frac{c}{8\pi}\epsilon_1^{1/2}\cos\theta|\mathbf{E}_0|^2(1-R) \quad (2.21)$$

$$\alpha\mathcal{P}_{SP} = \frac{c}{8\pi}\epsilon_1^{1/2}\cos\theta|\mathbf{E}_0|^2(1-R) \quad (2.22)$$

Which can be re-arranged making use of all previous equations and assumptions to give the ratio of $\frac{|\mathbf{E}_{SP}(0^+)|^2}{|\mathbf{E}_0|^2}$ i.e. the field enhancement:

$$\frac{|\mathbf{E}_{SP}(0^+)|^2}{|\mathbf{E}_0|^2} = \frac{2\cos\theta(\epsilon_2')^2(1-R)}{\epsilon_1^{1/2}\epsilon_2''(-\epsilon_2' - \epsilon_1)^{1/2}} \quad (2.23)$$

If $-\epsilon_2' \gg \epsilon_1$ is true then the maximum increase in intensity of the surface plasmon can be given approximately by the ratio of distance along the surface that the wave can coherently propagate, α^{-1} to the spread of the wave in the z direction:

$$\frac{|\mathbf{E}_{SP}(0^+)|^2}{|\mathbf{E}_0|^2} \cong \frac{2q_1'}{2k_{SP}} \cong \frac{2(-\epsilon_2')^{1/2}(-\epsilon_2' - \epsilon_1)}{\epsilon_1^{1/2}\epsilon_2''} \quad (2.24)$$

2.4.3 Localised Surface Plasmons

Localised surface plasmons (LSP) are non-propagating modes of oscillation that may be excited naturally (i.e. without the need for coupling techniques) at sub-wavelength sized structures or defects on a surface when an oscillating electromagnetic field is present [46].

Unlike surface plasmon polaritons it is possible for localised plasmons to be excited by both s- and p-polarised light. Excitation by s-polarised light will occur at the defect/structure due to the inhomogeneity in the z dependence of ϵ which acts as a confining potential for the surface wave (analogous to a particle bound in a quantum mechanical potential well) [47, 48]. In many cases the photoemission signal from a rough or purposely structured surface is shown to be greater for s-polarised light than for p-polarised light [49, 50, 51, 52].

Field Enhancement due to LSP is important and it is well known that a system excited by a femtosecond pulse can lead to these extremely localised fields known as “hot spots ” where the magnitude of the local field can exceed the exciting field by many orders (up to 10^6 [53]). The high field strengths reached are a result of the localisation in three dimensions rather than the one dimensional localisation of a SPP. The hot spots are known to produce enhanced nonlinear responses [54] and it should also be pointed out that the extreme spatial dependence is thought to break the translational invariance of the system thereby offering a continuous source of momentum such that the dipole approximation no longer holds i.e. non-vertical transitions can take place [53].

2.5 The Generation of High Kinetic Energy Photoelectrons at Surfaces Using Femtosecond Laser Pulses

The generation of photoelectrons using ultrashort pulses is of growing interest [55, 56] where there are clear uses for ultrashort electron pulses such as time resolved electron diffraction [57].

Despite the fact the ultrafast surface dynamics is a relatively large and well established field there are still areas of nonlinear photoemission from surfaces that are not yet fully understood [22]. There are several different cases [41, 50, 58, 59, 60] where photoelectrons with somewhat surprisingly high kinetic energies have been reported. In most cases explanations can be given for these observations however for others [61, 62], the excitation or acceleration mechanism is not clear, highlighting the need for a better understanding of high-order nonlinear excitation processes.

This section discusses a selection of excitation and acceleration mechanisms by which ultrashort laser pulses can be used to generate photoelectrons with high kinetic energies.

2.5.1 Ponderomotive Acceleration of Electrons Mediated by Surface Plasmons

Photoelectrons with high kinetic energies of up to 25 eV [41] and 0.4 keV [58] have been reported from metal films when laser pulses of with durations of 60 fs-800 fs and 27 fs respectively have been used to excite surface plasmons in the film via a grating or by prism coupling.

The high kinetic energies of the photoelectrons measured are attributed to those which have first overcome the work function by multiphoton excitation (Intensity dependence measurements give an order of nonlinearity corresponding to the number of photons required to overcome the workfunction) and subsequently gained ponderomotive energy due to the oscillating field of the plasmon.

Figure 2.10 shows examples of data taken by Kupersztych et al. [41] where it can be seen that the kinetic energies of the photoelectrons generated by this mechanism are strongly dependent on both the laser intensity and also the pulse duration. The kinetic energy of the photoelectron is given by the sum of its initial multiphoton energy (after overcoming the work function) and its quiver energy also known as the ponderomotive potential, U_P which is given in Equation 2.25. The longer the time that an electron spends in the field of the plasmon the more potential energy it can gain.

$$U_P = \frac{e^2 E_0^2}{4m_e \omega^2} \quad (2.25)$$

For a typical laser intensity used in these experiments of $I = 1.6 \times 10^{11}$ W/cm² the electric field due to the laser can be calculated from the relationship ($I = \frac{1}{2\sqrt{\mu_0 \epsilon_0}} E^2$ to be $E = 1.13 \times 10^9$ V/m). If this value is put into Equation 2.25 along with the laser frequency of $\omega = 2\pi c/800$ nm An estimate for the ponderomotive energy gained at the HOPG surface is just 0.01 eV. However the inclusion of a conservative estimate for the field enhancement at the surface of 1 order of magnitude would bring this value up to 1eV.

For few cycle pulses it has been shown that the ponderomotive electron acceleration may be directly controlled by the Carrier-Envelope Phase (CEP) of the pulse [17]. It has also been shown [63] that polarization gating using two elliptically polarised pulses coupled to a film by a prism coupler can improve upon the original prism coupling method demonstrated by Irvine et al. [17] by increasing the effective

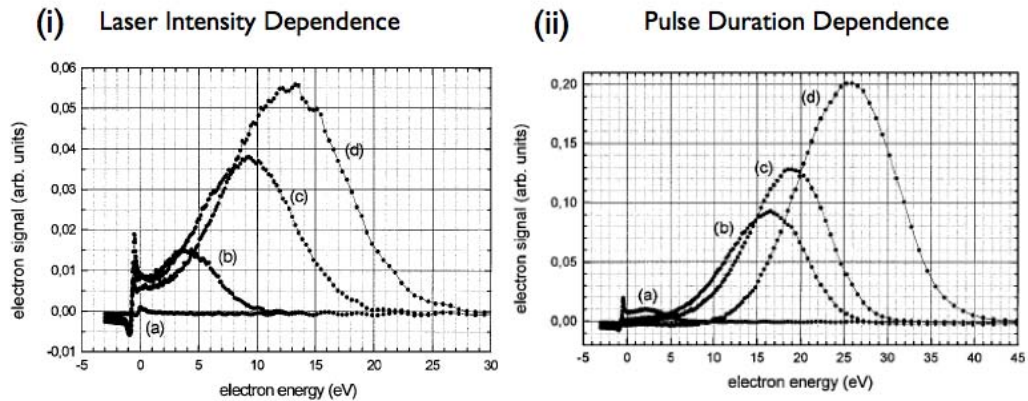


FIGURE 2.10: Ponderomotive acceleration of photoelectrons generated by surface plasmon assisted multiphoton photoelectron emission at a gold film. A sinusoidal grating was used to couple light into the 200nm film. (i) Laser Intensity Dependence: Photoelectron spectra generated by a 60fs laser pulse at intensities of (a) 1.67×10^9 W/cm², (b) 4×10^9 W/cm², (c) 6.5×10^9 W/cm² and (d) 8×10^9 W/cm² (ii) Pulse Duration Dependence: Photoelectron spectra generated at a laser intensity of 3.2×10^9 W/cm² by pulses with durations of (a) 60fs, (b) 190fs, (c) 400fs and (d) 800fs. Figure taken from and caption adapted from [41]

intensity, generating a high-gradient evanescent field that will accelerate electrons allowing them to obtain double the maximum kinetic energy as compared to the one pulse method. The symmetrical experimental set-up of the two pulses also ensures that the electrons propagate in the direction of the surface normal.

2.5.2 Field Enhancement

In other cases where photoelectrons with high kinetic energies have been observed it is suspected that field enhancement due to localised surface plasmons can play a part in the excitation of an electron (rather than the acceleration of an already liberated electron as described above). Aeschlimann et al. observed photoelectrons with excessive kinetic energy at the Cu(110) and Cu(100) surfaces [50] and explained their existence proposing localised hotspots due to surface roughness. They suggested that at such hotspots, field enhancement would bring the electric field ‘felt’ by the electron up to a value at which tunnelling ionisation would be

possible, this would otherwise not be plausible at the relatively low (10^8 W/cm²) laser intensities used. The smoothed nature of their photoelectron spectra (no ATI peaks) was used to support this argument.

2.5.3 Space Charge

When multiple photoelectrons are generated at a surface in close proximity to each other in a vacuum they will experience a mutual Coulomb repulsion. The kinetic energies of electrons in an electron cloud above the surface will be affected differently by this repulsion which causes an overall broadening and shift in the photoelectron spectrum where electrons from the part of the electron cloud that is closest to the surface will slow down, whereas electrons further away from the crystal surface will be accelerated. An example of a typical shift and distortion of a photoelectron spectrum due to space charge effects is that given by Petite et al. [60] who studied the photoelectron spectrum from metallic targets at intensities of 10^6 - 10^8 W/cm². A copy of their data is shown in Figure 2.11.

Space charge is a more important concern for intense laser interactions at metal surfaces due to the greater current densities involved. Riffe et al. [64] reported femtosecond thermionic electron emission from metal surfaces in the presence of strong space charge fields (They measured a current density of 550 A/cm²). By choosing to work with the HOPG surface rather than transition metals (which have the benefit of well-defined features in the photoelectron spectrum [26]) it is possible to avoid Coulomb explosion effects that would occur at the laser intensities used.

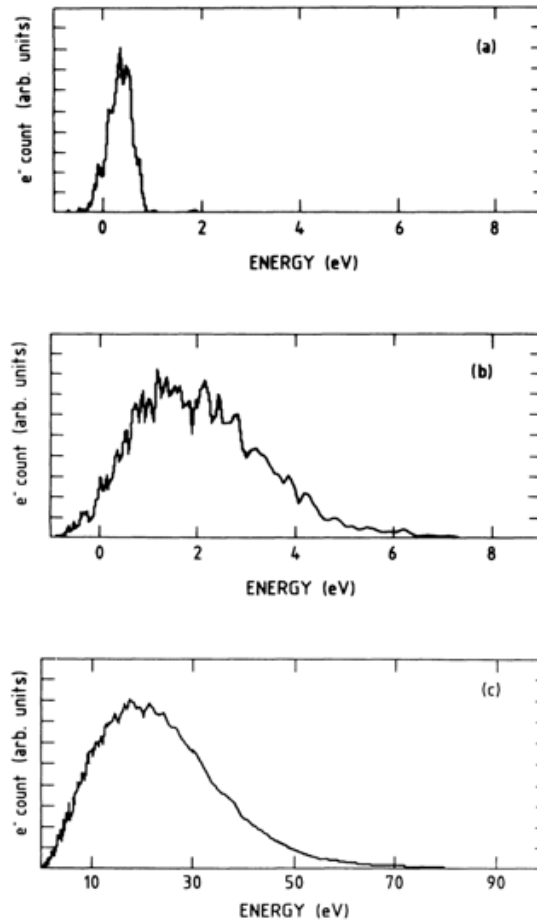


FIGURE 2.11: High Energy Photoelectrons generated by Space Charge: Experimental data taken from Petite et al. [60] using 35 picosecond pulses of 2.34eV energy incident on an aluminium surface. Laser intensities shown are (a) $5 \times 10^6 \text{ W/cm}^2$, (b) $3.5 \times 10^7 \text{ W/cm}^2$ and (c) $1.2 \times 10^8 \text{ W/cm}^2$. The origin of the high energy photoelectrons observed was explained by the energy broadening of the electron cloud generated at the surface.

2.5.4 High Kinetic Energy Photoelectrons Observed at Insulating Materials

Photoelectron spectroscopy of the CsI surface to investigate electron excitation dynamics at intensities close to the optical breakdown threshold [59] showed that electrons with kinetic energies of up to 24 eV could be generated. 40 fs laser pulses with a wavelength of 800 nm were used at intensities of $3 \times 10^{12} \text{ W/cm}^2$. Fig. 2.12 shows the photoelectron spectra. Similar behaviour was also reported at other insulating materials such as diamond [65].

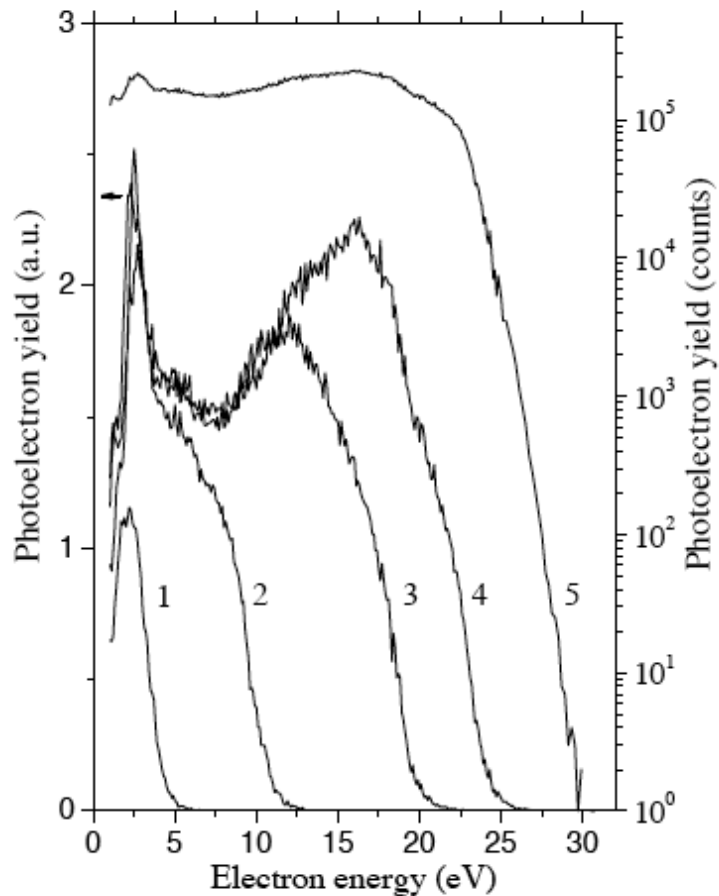


FIGURE 2.12: High Kinetic Energy Photoelectrons Generated at Insulator Surfaces: Photoelectron Spectra taken at the CsI surface using 800nm pulses at intensities of (1) 0.6 TW/cm^2 , (2) 1.2 TW/cm^2 , (3) 2.4 TW/cm^2 , (4) and (5) 3 TW/cm^2 . (Spectrum (5) is shown on a log scale whereas (1)-(4) are given on a linear scale) Figure taken from [59]

The possibility of space charge effects was ruled out as such effects should cause the entire spectrum to broaden i.e. to extend towards lower energies as well as higher energies. The low energy peak in the CsI however remains at a constant energy. Ponderomotive acceleration of photoelectrons was also ruled out and the photoelectrons were interpreted as the result of complex, interbranch transitions within the conduction band.

2.6 Attosecond Physics

Whilst the Ti:Al₂O₃ laser can be used to routinely produce pulses of ~ 30 fs [15] and these pulses can be compressed down to durations of 5 fs [66] an absolute limit exists at this value which corresponds to only two laser cycles.

There are two main methods by which this “femtosecond barrier” can be broken. One of these, stimulated Raman scattering has been shown to successfully produce sub-femtosecond pulse trains [67] however this thesis will concentrate on the alternative method; the generation of attosecond pulses via High-order Harmonic Generation (HHG).

2.6.1 High-order Harmonic Generation: The 3 Step Model

High-order Harmonic Generation (HHG) involves the focusing of a few cycle laser pulse onto a target to generate harmonics with such a high order that their wavelength lies in the XUV regime. A few-cycle pulse in the XUV regime will have a sub-femtosecond duration. Commonly the target used will be a gas jet of a gas such as argon or neon whereby laser intensities of 1×10^{14} W/cm² are required for HHG to occur [68].

The process can most easily be explained using the semi-classical “Three Step Model” first suggested by Paul Corkum in 1993 [4]. This model describes a single atom’s response when excited by a laser pulse in the strong-field regime.

Under the influence of the strong electric field of the laser, particularly at the peaks of the electric field amplitude the Coulomb potential that binds a valence electron to the core of an atom can become distorted to such an extent that the electron can tunnel out of the barrier (shown as step 1 in Figure 2.13). Once free in the continuum the electron will be accelerated under the influence of the

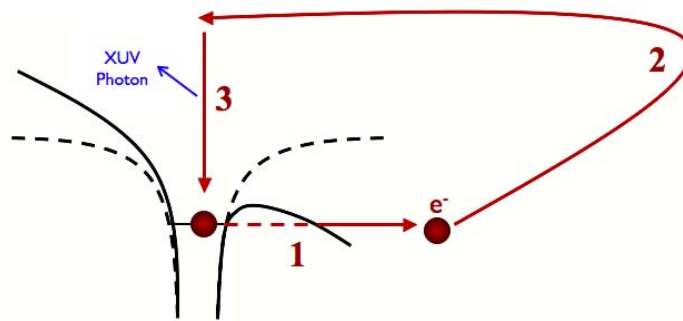


FIGURE 2.13: Schematic of the 3-step semi-classical explanation of High Harmonic Generation: 1) Tunnel ionisation possible due to distortion of the atomic potential by the strong laser field (the original Coulomb potential shown by black dashed line and the distorted potential by the solid black line). 2) Acceleration of the free electron in the laser field firstly away from the original atom and then back as the field changes direction. 3) There is a probability that the returning electron will recombine with the parent ion. Potential energy gained by the electron during the acceleration process can be released as an XUV photon.

oscillating field of the laser and when the linearly polarised field changes direction the electron will be accelerated back in the direction of the original atom (step 2 in Figure 2.13). Once the electron returns there is a chance that it will combine with the parent ion, in this case, the energy gained during the acceleration can be released as an XUV photon (step 3 in Figure 2.13), the re-collision process can also result in other effects such as secondary electron emission or the excitation of bound electrons.

Figure 2.14 is a schematic portrayal of a typical HHG spectrum. The intensity of the odd harmonics generated starts to fall initially before reaching a plateau where the harmonic intensity stays constant with increasing harmonic order (frequency) until the cut-off region is reached. Since an electron can be released around each peak amplitude and since the pulse is symmetric about the axis of propagation, the HHG process will repeat itself at every half cycle giving rise to a train of attosecond pulses with a separation in time of half the laser period, this has been demonstrated experimentally by Paul et al [69] and will correspond, in the spectral

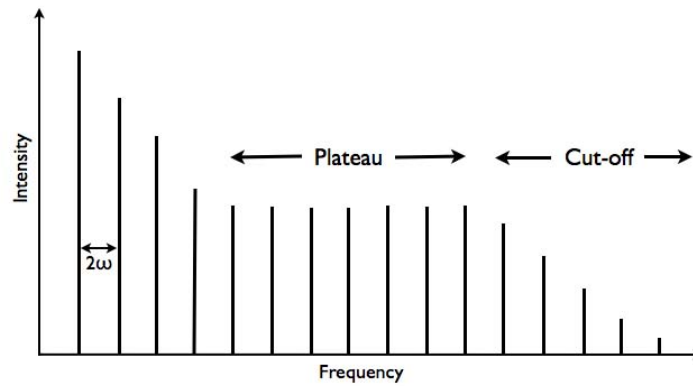


FIGURE 2.14: Diagram of the HHG Spectrum: Odd harmonics are produced, separated by twice the frequency of the driving laser. After an initial fall in intensity with increasing harmonic order the intensity stays stable forming a plateau until finally reaching a cut-off value which is dependent on the gas used and the experimental conditions.

domain, to a separation in harmonics of 2ω [70].

The energy of the XUV photon depends directly on the energy gained by the electron during the acceleration process. Depending on the time at which an electron is released it will follow a different trajectory, spending a different amount of time in the presence of the field. The energy gained by the electron “wiggling” in the electric field, known as the ponderomotive energy depends on the time that the electron spends in the field. “Long trajectories” are followed when the electron is released around the very peak of the E-field and “short trajectories” occur when the electron is released at slightly later times and have a shorter time of transit [3, 71]. The maximum photon energy possible (corresponding to the cut-off point in Fig. 2.14) is given by $I_P + 3.17U_P$ [4], where I_P is the Ionisation potential of the gas used as a target and U_P is the ponderomotive potential (sometimes called the ponderomotive energy or quiver energy) given by Equation 2.25.

2.6.2 Attosecond Pulse Trains vs. Single Attosecond Pulses

As shown in Fig. 2.14, High Harmonic Generation gives rise to a comb of different harmonics. In the time domain this will correspond to a train of attosecond pulses. In the experiments reported in this thesis such pulse trains have been used to investigate the surface however it should be pointed out that it is possible to isolate single attosecond pulses which are required for attosecond time-resolved experiments [9, 72].

There are two main ways in which isolated attosecond pulses may be produced. The first is by filtering part of the HHG spectrum. If the IR driving laser pulse has a duration of ~ 5 fs then the HHG spectrum will have a smooth continuum at the highest harmonic orders instead of the tail in individual peaks shown at the cut-off in Figure 2.14 [73]. This continuum occurs for very short pulse only because there is only one re-collision at the maximum energy. For a longer pulse there are many re-collisions around the maximum energy. By filtering out the rest of the HHG spectrum to keep only this cut-off continuum region a single pulse is selected. The second method is polarisation gating. This method works by modulating the polarisation of the driving IR pulse so that the electron/wavepacket collision can be controlled and only a single return occurs. Again, this single re-collision event is the condition for a single attosecond pulse [74]. An advantage of the polarisation gating method is that single cycle pulses can be produced so a shorter pulse duration achieved. Sansone et al. have achieved a pulse duration of just 130 as at a 36 eV photon energy (1.2 optical cycles). The ability to isolate pulses within this spectral range is also an advantage because photon energies of 36 eV are useful to study the excitation of the outermost electrons in atoms, molecules and solid state systems [75]. (In comparison the cut-off for neon harmonics is around 90 eV [72]).

Unfortunately the minimum pulse duration which could be achieved by the Imperial College laser was ~ 7 fs which is above that required to generate the continuum in the HHG spectrum so it was not possible to generate single attosecond pulses. One advantage of using the XUV pulse trains is the increased signal as compared to the case of an isolated single pulse.

2.6.3 Attosecond Measurements at Surfaces

To date, the majority of experiments utilising pulses with attosecond timescales have been carried out in the gas phase. With increased understanding and improvements in experimental techniques interest is now turning to their potential use in the more complex solid state systems. There is a wide range in potential applications in solids since many condensed matter phenomena have timescales of a few femtoseconds and below such as plasmons, charge screening, hot electrons and electron-hole dynamics [5].

Figure 2.15 shows examples of surface processes that could be probed using attosecond pulses. Possible measurement techniques are suggested, the first of which is attosecond streaking spectroscopy, where photoelectrons are liberated by the XUV pulse whilst in the presence of an E-field. The emitted electrons will experience a change in momentum that is proportional to the vector potential of the E-field at the instant the electron is released [76]. As such, electrons released at different times experience different initial velocities and so a photoelectron energy spectrum is a map of the initial temporal emission profile of the electrons and hence of the temporal profile of the XUV pulse. In the 2005 experiment by Goulielmakis, attosecond streak spectroscopy is used to map out the intensity profile of a few-cycle IR pulse using a 250 as XUV pulse. In this case the broadening (“streaking”) observed is very small but the recorded photoelectrons also exhibit a significant shift in energy which is linearly proportional to the vector potential of

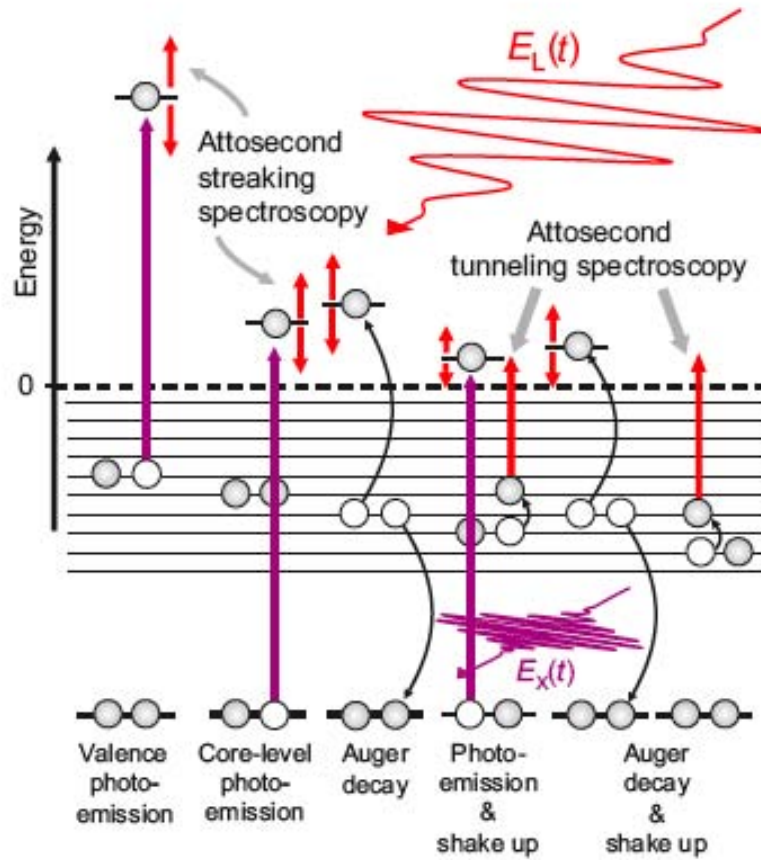


FIGURE 2.15: Excitation and relaxation processes that can be investigated using attosecond pulses. Figure taken from [5]

oscillating IR field at the time at which the electron was liberated [9]. In these type of experiments the laser field is usually chosen to be weak enough to not excite electrons but strong enough to result in a change in momentum of the photoelectrons liberated by the XUV pulse [5]. The other method shown in Figure 2.15 is Attosecond tunnelling spectroscopy. Using this method it is possible to probe the lifetime of bound states by releasing electrons from these bound states by tunnel ionisation [77]. Both of the spectroscopic methods described above require a weak pump pulse (XUV) and strong probe pulse (e.g. a few-cycle IR pulse).

In principle the standard TR-2PPE experiments as described on page 19 would be possible in the attosecond regime providing both pump and probe pulses had

a suitably short duration, at present this is not experimentally feasible. Another prediction for attosecond measurements at surfaces is an experimental method proposed by Stockman et al. [78]. They propose that by combining attosecond streaking spectroscopy and photoelectron emission microscopy (PEEM) into one tool, the “attosecond nanoplasmonic-field microscope”. As in streaking experiments this would involve an initial few-cycle IR pulse and an XUV pulse which would be delayed relative to each other. The few-cycle pulse could be used to excite localised surface plasmons at defects or nanostructures and then the XUV pulse would generate photoelectrons which would be accelerated by the plasmonic field and detected with both spatial (nm) and energy resolution using the PEEM. The combination of the nanometer spatial resolution and ~ 100 as temporal resolution would make the tool extremely useful to study localised plasmon effects including use as a testing device for optoelectronic components, however experimental verification of the method has yet to be published.

Although the future for attosecond surface experiments looks bright there are very few examples to date of successful experiments [5], this is probably due to the high levels of complexity involved. The most significant measurements are those performed by Cavalieri et al. [10]. By using a streaking technique on a tungsten crystal they measured a relative delay between electrons excited by the XUV pulse from the conduction band and from the $4f$ core state as 110 ± 70 as. These measurements are shown in Fig. 2.16. Calculations of the photoelectron spectra made by Zhang et al. [11] also showed a similar temporal shift between the conduction band electrons and the core level electrons.

Solid state systems have also been investigated as targets for HHG [79, 80] and it has been found that by utilising field enhancement due to localised plasmons at nanostructured surfaces it is possible to lower the laser intensities required to only 10^{11} W/cm² [44].

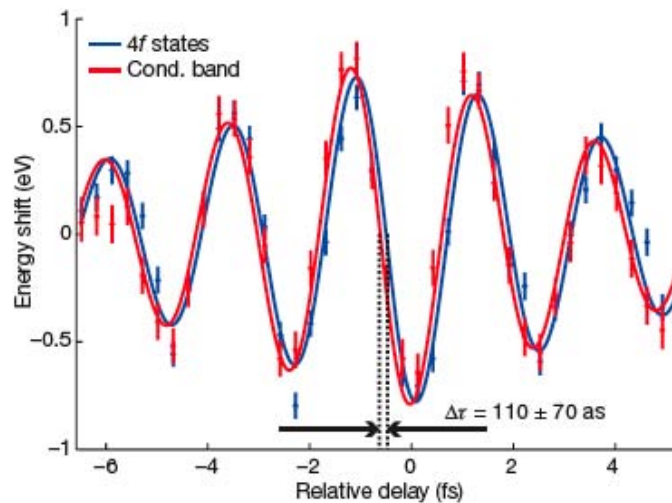


FIGURE 2.16: Delayed photoemission observed by attosecond streaking spectroscopy of the conduction band (red) and 4f states (blue) of a tungsten crystal. Both curves show the shift in kinetic energies of photoelectrons liberated from the respective states in tungsten by an XUV photon in the presence of an IR few cycle pulse. The relative delay between the two curves gives the relative delay of the two excitation processes. Figure taken from [10]

2.7 Autocorrelation Techniques

An autocorrelation measurement is a scan over time of two identical pulses that have been split from one initial pulse and are then recombined in such a way that the relative temporal delay (τ) between the two pulses can be altered. Autocorrelation techniques are primarily used as a tool to measure the duration of a pulse however they can also be used to investigate lifetimes for example of excited surface states [34]. Such measurements can be used to obtain information about the nonlinearity of a process and also the phase (coherence) [81]

The intensity of the re-combined signal from the two pulses as a function of τ is given by:

$$I_1(\tau) = \int_{-\infty}^{+\infty} |E(t) + E(t - \tau)|^2 dt \quad (2.26)$$

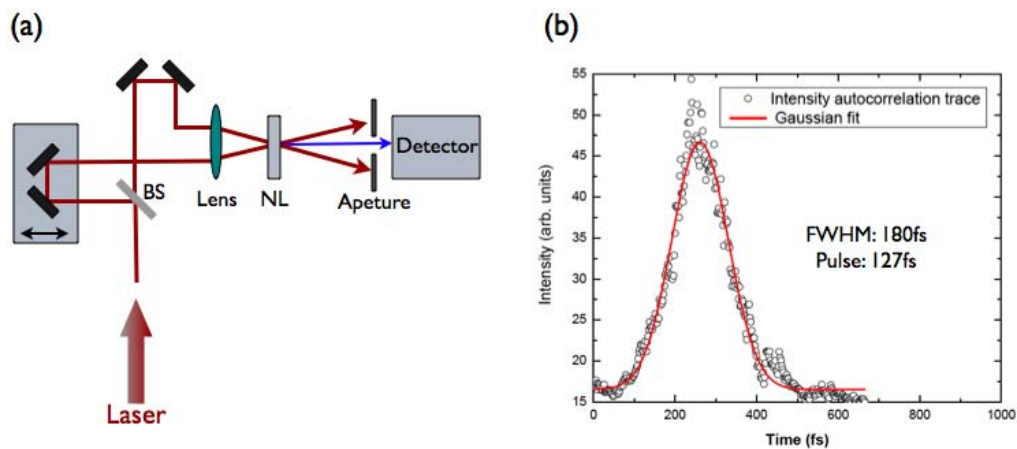


FIGURE 2.17: Intensity Autocorrelation Measurements: (a) A schematic diagram of a second harmonic intensity autocorrelator where BS is a beam splitter and NL is a nonlinear crystal (b) An example of an intensity autocorrelation measurement of a 127 fs pulse where the pulse duration is taken from the FWHM measurement using the $1/\sqrt{2}$ Gaussian factor.

It is common for the two pulses to be recombined at a nonlinear crystal (usually a birefringent second harmonic generation (SHG) crystal such as BBO (beta Barium-Borate) or KDP (Potassium Dihydrogen Phosphate)) resulting in an improvement of the signal to noise ratio. In this case the signal of the second harmonic at the output of the crystal can be described by:

$$I_2(\tau) = \int_{-\infty}^{+\infty} ||E(t) + E(t - \tau)||^2 dt \quad (2.27)$$

which can be expanded to give:

$$I_2(\tau) = \int_{-\infty}^{+\infty} |\{E(t) \exp i[\omega t + \Phi(t)] + E(t - \tau) \exp i[\omega(t - \tau) + \Phi(t - \tau)]\}|^2 dt \quad (2.28)$$

The generation of the second harmonic inside the crystal is discussed in more detail in Appendix B.

There are two different types of autocorrelation measurements; intensity autocorrelation, shown in Fig. 2.17 and interferometric autocorrelation, shown in Figure 2.18. .

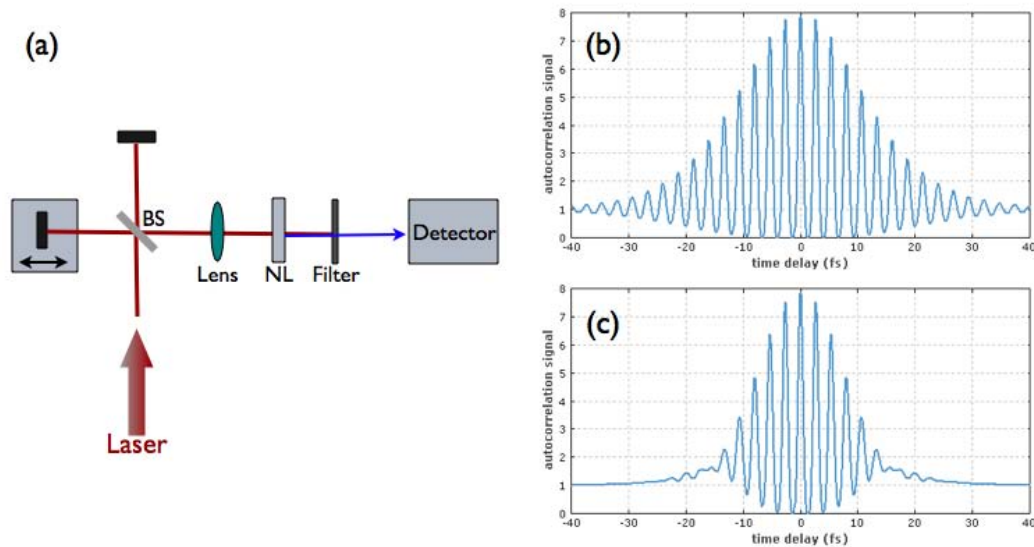


FIGURE 2.18: An Example of Chirp Dependence of an Interferometric Autocorrelation Trace: (a) A schematic diagram of a typical interferometric autocorrelator (b) An interferometric autocorrelation trace (i.e. power measured by the detector as a function of pump-probe delay) of a 15 fs sech^2 pulse with no chirp (c) A trace taken for chirped pulse of identical duration. A smaller width is observed. Figure taken from [15]

The important difference between the two methods lies in the re-combination of the two pulses. For intensity autocorrelation measurements the two pulses are combined on the crystal at an angle to each other so their momentum vectors at the point of spatial overlap are not identical, for interferometric autocorrelation however the combined pulses follow a collinear path. The result of this total overlap is that the AC trace will exhibit bright and dark fringes with a periodicity equal to one cycle of the laser i.e. temporal interference. For linear autocorrelation, at the delay corresponding to the point of maximum constructive interference the amplitude of the field will be twice that of an individual pulse, this will correspond to a measured intensity of four times that of the individual pulse. For SHG autocorrelation this will be equal to 16 times the initial intensity. This leads to the 8:1 ratio as seen in Figure 2.18 since the background is just the sum of the intensity from the two pulses.

Another effect of the collinear geometry is that the trace will be sensitive to the

chirp of the pulse as shown in Figure 2.18(b) and (c). A disadvantage of this is that the trace could be misinterpreted and the pulse duration underestimated however an advantage is that using numerical analysis packages that can be bought commercially, it is possible to extract some limited information about the chirp [15]. The geometrically simplistic design of the interferometric AC technique over its rival makes it the favoured tool for pulse characterisation in the femtosecond regime down to the few cycle regime. For pulses entering the few-cycle regime (~ 15 fs and below) the preferred method of pulse characterisation is frequency resolved optical gating (FROG) which is derived from the SHG intensity autocorrelator but gives a full spectral and temporal description of the pulse simultaneously. It is described in more detail in Chapter 3 .

2.8 Graphite

The work reported in this thesis has been carried out at the surface of HOPG (Highly Oriented Pyrolytic Graphite). There were several factors which influenced the choice of material: The HOPG surface can be easily and reliably prepared, common practice is to use adhesive tape to cleave off the top layers [82, 83] which is considerably easier than other samples which require sputter and annealing cycles. It is also chemically inert so it is less important that low vacuum conditions (below 10^{-9} mbar) are reached as compared to other reactive surfaces. The recent rise in interest surrounding graphine [84, 85] means that graphite is still very much topical however it has also been fairly well studied, no doubt in part due to the ease in which it can be prepared. The band structure has been well characterised previously both theoretically [86, 87] and experimentally [82, 83, 88, 89, 90] and the optical properties studied [91, 92].

The properties of graphite allowing the simple preparation techniques can be explained by its structure. Figure 2.19 (a) shows an example of the stacking sequence

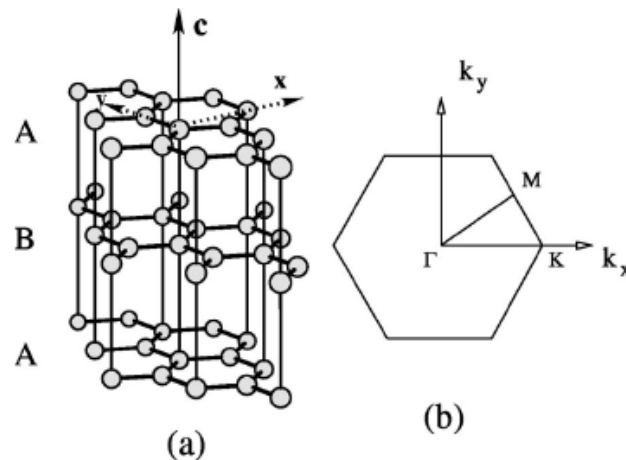


FIGURE 2.19: (a) The ABA stacking of sheets of graphine to form graphite (b) Two-dimensional section of the Brillouin zone taken at the zone centre. Figure and caption taken from [86]

of layers of graphene, each made up of hexagonal lattices of carbon atoms. The carbon atoms in graphite are sp^2 hybridised ($2s$, $2p_x$, $2p_y$ involved in the hybridisation) so that these orbitals take a trigonal planar shape. This results in each carbon atom forming 3 strong σ bonds with other carbon atoms in the same layer forming the hexagonal lattice. The remaining p orbital ($2p_z$) lies normal to the plane of the other orbitals and overlaps sideways with other $2p_z$ from the other carbon atoms to form weaker π bonds above and below each sheet of graphine. The delocalised electrons in these pi bonds are responsible for the semimetallic behaviour of graphite i.e. its electrical conductivity.

Figure 2.20 shows the band structure of graphite as calculated by Marinopoulos et al. [86]. The corresponding points on the Brillouin zone are shown in Figure 2.19 (b).

Previously, ultrashort pulse have been used at the HOPG surface to investigate several effects including: Image potential states [93], Phonon mediated intraband cooling over ~ 100 fs timescale [94] and better understanding of laser-matter interactions such as the formation of sub-wavelength apertures using near-ablation

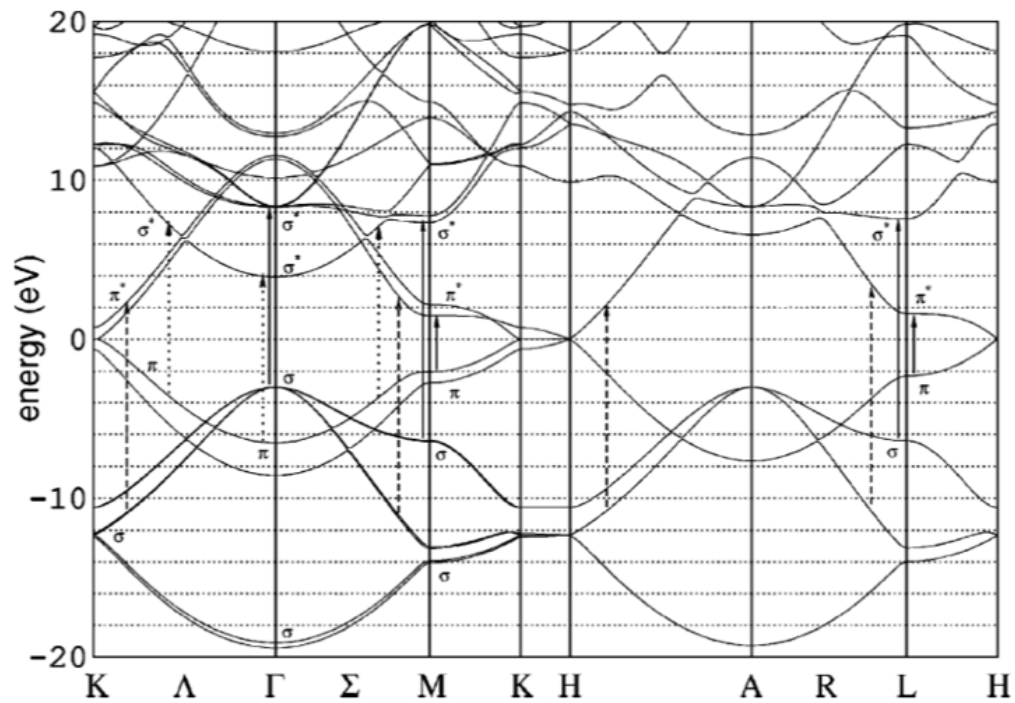


FIGURE 2.20: Graphite Band Structure: shown along high symmetry directions of the Brillouin zone. 0eV corresponds to the Fermi Level and arrows denote interband transitions. Figure and caption taken from[86].

fluences [43]. The work of Huang et al. [43] showed a good example of the change in material properties when in its highly excited state and the need for a better understanding of such laser-matter interactions.

Chapter 3

Photoelectron Spectroscopy of the HOPG surface

3.1 Introduction

Improvements in laser technology have underpinned a trend towards increasingly shorter laser pulses which have traditionally been tested and used in gas phase experiments [3]. Recently a combination of few-cycle IR pulses and attosecond duration XUV pulses have been used to make real-time measurements of electron excitations at the surface of a tungsten crystal [10, 11] highlighting the applications of such short pulses at surfaces. This chapter describes collaborative experiments carried out at the Blakett Laboratory, Imperial College London using surface science equipment belonging to Birmingham University and a beam-line built by Imperial College. The motivation behind the collaboration was to work towards attosecond measurements at surfaces.

The surface of HOPG (Highly Oriented Pyrolytic Graphite) has been investigated by Time of Flight (ToF) photoelectron spectroscopy using both few-cycle infra red laser pulses of 13 fs duration (photon energy = 1.55 eV) and also XUV pulse trains

(photon energy $\sim 30\text{eV} - 45\text{eV}$). In the short pulse/strong field regime produced by IR few-cycle pulses at the surface it was found that these photons of 1.55 eV energy could be used to generate photoelectrons with kinetic energies of up to 80 eV.

A description of the experimental apparatus used is given and the methods used to collect the photoelectron data explained. The photoelectron spectra taken from the HOPG surface are presented and analysed. Finally, possible mechanisms leading to the observation of such high energy photoelectrons are discussed.

3.2 Technical Background

3.2.1 The Production and Characterisation of Few Cycle Laser Pulses

All experiments described in this chapter were carried out at the Attosecond Beamline in the Blackett Laboratory, Imperial College. The beamline was driven by a Titanium:Sapphire CPA (Chirped Pulse Amplification) system (model:CompactPRO) bought from Femtolasers GmbH. The system produced Infra Red (IR) pulses of 30 fs duration at a 1 kHz repetition rate with a central wavelength of 800 nm (spectral range 750-850 nm) and a typical energy of ≤ 1 mJ. As shown in Fig.3.1, the 30 fs duration IR output from the Femtolasers system could be used as standard to perform experiments or by using a hollow fibre pulse compression technique they could be used to generate few-cycle IR pulses with a minimum duration of 7 fs. These temporally compressed pulses could then also be used for surface experiments. Both the original 30 fs pulses and the hollow fibre compressed pulses could be fully characterised (spectrally and temporally) using frequency resolved optical

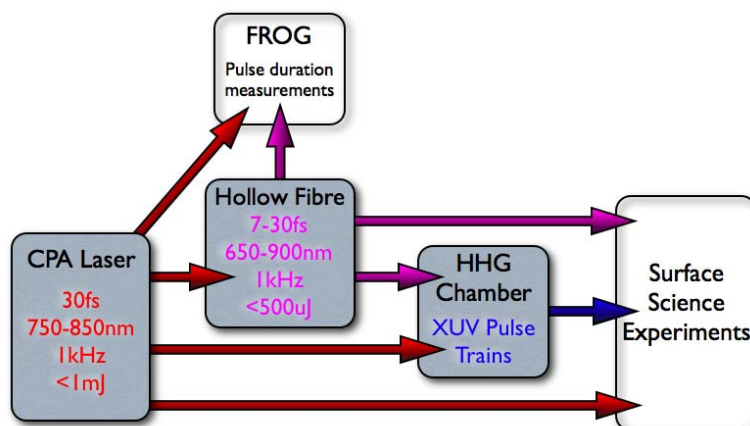


FIGURE 3.1: Overview of the light sources used for surface science experiments at Imperial College. The 30 fs pulses produced by the drive laser can be broadened spectrally using a hollow fibre setup to generate pulses with a tunable duration ranging from 7-30 fs. Experiments may be carried out at the surface using either the 30 fs IR pulses from the drive laser, the shorter pulses from the hollow fibre or alternatively XUV pulse trains generated by High Harmonic Generation (HHG).

gating (FROG). They could also be used to generate XUV pulse trains by High Harmonic Generation (HHG).

Detailed descriptions of the equipment and methods used are given below:

3.2.1.1 Chirped Pulse Amplification

Chirped Pulse Amplification (CPA) provides a mechanism by which the peak power of a laser pulse may be increased to levels that would otherwise cause damage to the Titanium:Sapphire laser crystal. The nonlinear response of the laser crystal forms the basis for Kerr Lens Mode-locking (KLM), a passive method of mode-locking where the chosen mode will correspond to the shortest pulse which the cavity can support. In the laser gain medium, the central most intense part of the gaussian beam profile experiences a different refractive index to the outer part of the beam creating a lensing effect. This effect is what allows for passive mode-locking; for a hard aperture approach a simple aperture blocks the less focused beam paths corresponding to a lower laser intensity. Alternatively for soft

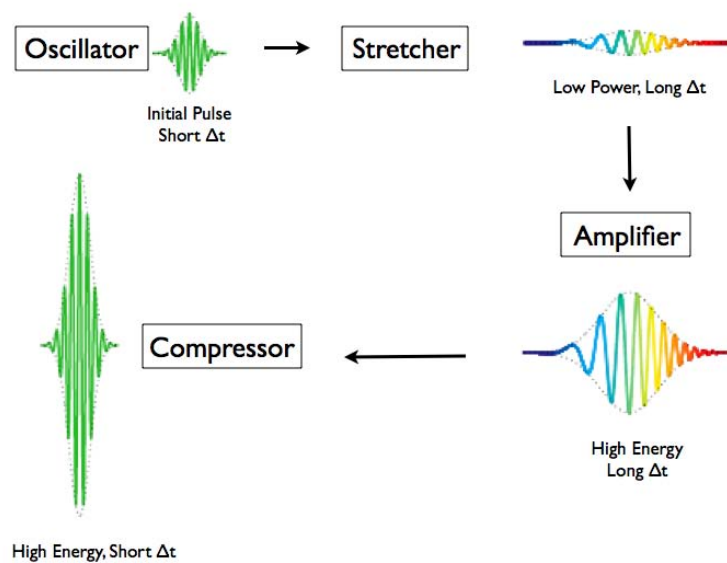


FIGURE 3.2: A Diagram of the Chirped Pulse Amplification Process: The output pulse from the oscillator is stretched temporally before being amplified. Re-compression of the amplified pulse results in an ultrashort pulse with high peak power. Figure adapted from [96].

aperture KLM as used in the CompactPRO system the overlap of the laser pulse and the pump pulse within the gain medium is greatest for the highest intensity more focussed pulses thereby leading to their increased gain until eventually over many complete trips around the laser cavity only one peak, the shortest and most intense, will remain. A problem with the KLM approach is that in extreme cases self-focusing will lead to laser intensities above the damage threshold of the gain medium thereby imposing a limit on the peak power of the pulse which may be generated. Chirped pulse amplification, invented by Donna Strickland and Gerard Mourou in the 1980's [95] allows for this limit to be overcome. The pulse is temporally stretched (chirped), reducing its intensity before amplification and then re-compressed afterwards resulting in an ultrashort pulse with higher peak power than would otherwise have been possible. This is illustrated in Fig 3.2.

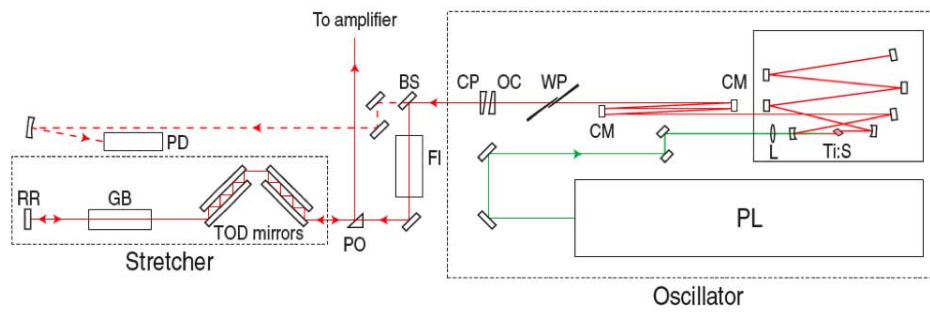


FIGURE 3.3: Schematic of the laser oscillator and stretcher. PL: pump laser (CW, 4 W, 532 nm), L: lens, Ti:S: titanium sapphire crystal, CM: chirped mirror, WP: wedge pair, OC: output coupler, CP: compensating plate, BS: 30:70 beamsplitter, FI: Faraday isolator, TOD mirrors: chirped mirrors for third order phase compensation, GB: 10 cm long SF10 glass block, RR: retro-reflector, PO: pick-off mirror, PD: photodiode. (figure and caption taken from [97]).

3.2.1.2 The Titanium Sapphire Laser System

The oscillator used (Femtosource Scientific PRO Oscillator) consisted of a Kerr lens mode-locked Ti:Sapphire crystal pumped by a Verdi V5 (by Coherent) as illustrated in Fig.3.3. The Verdi pump laser is a frequency doubled Neodymium:Yttrium Orthovanadate (Nd:YV04) with a maximum output of 5 W and a wavelength of 532 nm. The oscillator produces 10 fs IR pulses with a central wavelength of 800 nm (FWHM 100 nm) at a 75 MHz repetition rate with a power of 400-450 mW.

The output pulses from the oscillator pass through a Faraday isolator, preventing back reflections from propagating around the cavity. Before entering the stretcher, multiple reflections off chirped mirrors pre-compensate for third order dispersion (TOD) in the amplifier crystal and compressor prisms. The pulses are then passed through the stretcher, a 10 cm long glass block twice and back through the TOD mirrors to the amplifier.

The amplifier used was a multi-pass Ti:Sapphire amplifier pumped by a Corona (made by Coherent) pump laser. A schematic of the amplification process is shown in Figure 3.4. The Corona is a frequency doubled Q-switched Nd:YAG laser with

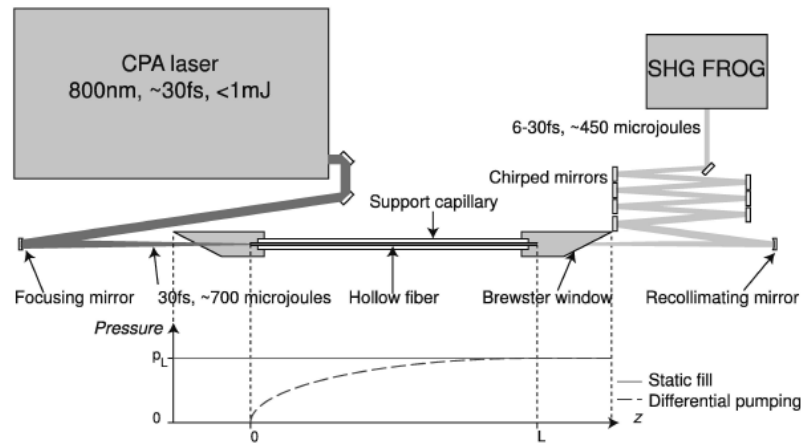


FIGURE 3.5: Schematic diagram showing the final stage of the production of few-cycle pulses [98].

are mounted on a vernier translation stage and translational adjustments can offer some control over pulse duration including pre-compensation for dispersion effects of the final pulses e.g. through air.

3.2.1.3 Pulse Compression using a Hollow Fibre

The laser output of 30 fs duration pulses could be further compressed down to ~ 7 fs using hollow fibre pulse compression. The use of a hollow fibre in the compression of ultrashort pulses was first demonstrated by Nisoli et al. in 1996 [66]. The fibre, filled to a high pressure with noble gas forms a waveguide along which the pulse propagates. During propagation the spectrum of the incident pulse is broadened by self-phase modulation (SPM). Reflections at the inner surface generate significant losses which discriminate against high order modes and for this reason long fibres (e.g. 70 cm - 1 m) are usually chosen to ensure that only the fundamental mode can propagate. The output of the hollow fibre is then compressed using either prisms or chirped mirrors resulting in few cycle pulses.

For the experiments described in this thesis, a variation of this technique was used with the difference being that the gas inside the hollow fibre was differentially

pumped to produce a pressure gradient along the fibre starting with a vacuum (10^{-1} mbar) at the input (Figure 3.5). The hollow fibre is contained in a chamber and the gas is injected into the light exit end of the chamber and pumped out from the entrance. Compared to a more traditional statically filled fibre, differential pumping leads to a higher transmission rate and increased spectral broadening. The energy output of a traditional hollow fibre is limited by plasma formation and damage at the entrance to the fibre so eliminating the gas at the entrance to the fibre allows for higher input power to be used. It has been shown that differentially pumped fibres can be used to produce sub 10 fs pulses with an energy of up to 5 mJ [99]. Another advantage, with more relevance to this work (where the input of the hollow fibre has a maximum of 700-800 μ J) is that by adjusting the pressure of gas in the fibre, the duration of the output pulse may be varied smoothly without affecting the energy of the output.

A series of chirped mirrors are used to compress the pulse resulting in a minimum duration of 7 fs. The final pulses have a bandwidth of FWHM \sim 650-900 nm, 1 kHz repetition rate and an energy of $< 500\mu$ J.

3.2.1.4 Pulse-Characterisation by Frequency Resolved Optical Gating

Second Harmonic Frequency-Resolved Optical Gating (SHG FROG) provided a means of pulse characterisation for infra-red pulses from both the laser output and also the hollow fibre output (see Figure 3.1). As previously described (page 43) a FROG trace displays both spectral and temporal information simultaneously.

The FROG at Imperial College is constructed using high bandwidth components including silver mirrors and a broadband (600-1000 nm) 0.46 mm thick 50:50 beamsplitter used to split the fundamental into two equal IR pulses. A diagram of the set-up is shown in Fig.3.6. The pulse generated by reflection off the beam splitter passes through a compensating plate to ensure equal passage through the

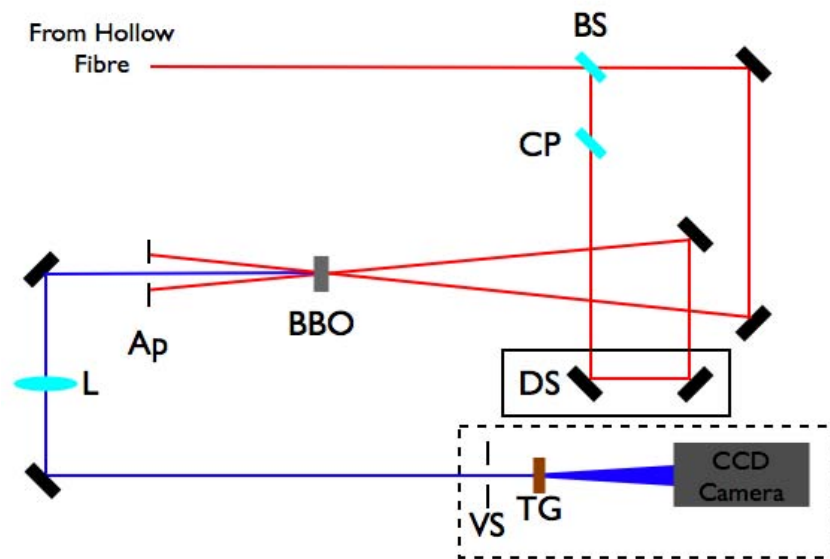


FIGURE 3.6: A Diagram of the FROG Apparatus Used for Measurements of the Pulse Duration. Two equal pulses are generated using a broadband $420\ \mu\text{m}$ beam splitter (BS in diagram). The compensating plate (CP) ensures each pulse passes through the same thickness of glass. The two pulses are then crossed in the BBO crystal, generating a second harmonic. The aperture (Ap) removes IR fundamental. Using the delay stage (DS) a SHG autocorrelation signal is generated which is imaged by an imaging spectrometer made up of variable slit (VS), UV transmission grating (TG) and a CCD camera sensitive to UV light. A lens (L) creates an image of the crystal at the slit (VS) of the spectrometer.

material and therefore equal dispersion of the two pulses. A motorised translation stage with micron precision was used to delay one pulse with respect to the other. The two arms of the autocorrelator were then crossed in a BBO (beta Barium-Borate) crystal. As previously described in the theory section (page 41), when the two non-collinear pulses overlap in the crystal both in space and time, a second harmonic signal is generated. This second harmonic signal is imaged using a thin fused silica lens onto a variable slit entrance of an imaging detector. A transmission grating inside the spectrometer acts to spectrally disperse the signal. As the translation stage is moved this signal is imaged over a range of delays using an imaging spectrometer. The end result is known as a FROG trace where one axis corresponds to the delay, τ between the pulses and the other axis corresponds to wavelength. An example of such a trace is shown in Figure 3.7. Commercial

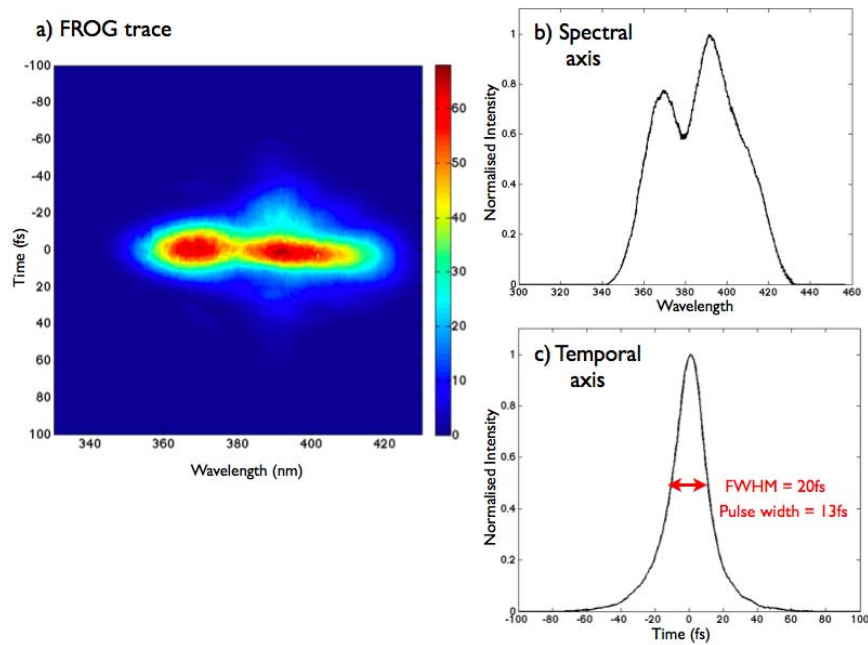


FIGURE 3.7: A FROG measurement taken before an experiment on the graphite surface: a) shows the FROG trace. The air path travelled by the beam from the laser source to the experiment was accounted for along with all optical components used so that any effects occurring due to dispersion were included b) gives the intensity (integrated over time) of the second harmonic signal measured as a function of the wavelength in nm c) gives the signal intensity (integrated over the spectrum) measured by the spectrometer as a function of pump-probe delay (τ) in femtoseconds. After applying a sech^2 fit ($\Delta\tau/\Delta t = 1.54$) the FWHM measured corresponded to a pulse duration of 13 fs.

software by Femtosec Technologies was required to retrieve the pulse duration and temporal phase as well as the pulse spectrum and spectral phase.

3.2.2 The Production of XUV Attosecond Pulse Trains

The vacuum beamline used to generate XUV pulse trains and to focus them and/or few-cycle IR pulses onto the surface is shown in Figure 3.8. The beamline was large with a complex arrangement in order to accommodate the needs of several users but this thesis will concentrate only on those elements required for surface science experiments.

The first chamber of the vacuum beamline (from left to right) was the High Harmonic Generation (HHG) chamber. An off-axis parabolic mirror (labelled M1 in Figure 3.8) was used to focus the few-cycle IR pulses into an argon gas jet. At the focus, at laser intensities of ($\sim 10^{14}$ W/cm²), it was possible to generate trains of odd harmonics in the extreme ultra-violet (XUV) spectrum via High Harmonic Generation (HHG). For more details on the theory behind the HHG process see page 33. Two different varieties of gas jet were used to generate harmonics for experiments. The first was a piezo driven pulsed gas jet with KHz repetition frequency and the second variety a differentially pumped double walled tube target. Both were found to produce comparable HHG spectra. The KHz gas jet had the advantage that the argon gas was only present during the laser pulse therefore less strain was put on the turbo molecular pumps providing the vacuum. As a downside however its constituent parts could be unreliable and fixing faults was both expensive and time-consuming. The double walled tube target was constructed of a thin metal inner tube (~ 5 mm diameter) with small apertures for the focussed beam and a larger outer plastic tube (~ 3 cm diameter) with slightly larger holes for the beam to pass through either side of the focus. The outer tube was differentially pumped using a scroll pump. This design for a continuous flow tube target was found to significantly outperform an earlier tested version made of just the outer tube because it allowed the pressure of argon within the interaction region to be raised without damaging the vacuum pumps. The base pressure of the HHG chamber, with no argon gas present was 1×10^{-6} mbar.

After the production of the XUV harmonics pulse train, the fundamental IR beam had to be removed. This was accomplished using a 200 nm Al filter mounted on a motorised filter wheel (FW in Fig. 3.8) housed in a separate chamber between the HHG chamber and an analytical chamber. The filter removed the IR fundamental and any harmonics with a photon energy 11 eV and below.

It was possible to measure the harmonics and hence the photon energies incident

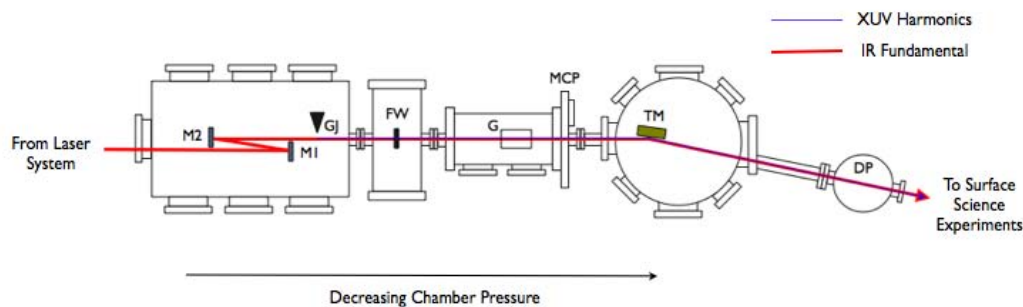


FIGURE 3.8: Diagram of beamline for surface science experiments at Imperial College. Consisting of an off-axis parabolic mirror, M1 which creates a focus of the fundamental at the gas jet, GJ; a flat mirror, M2; motorised filter wheel, FW; grating, G; imaging microchannel plate MCP for imaging of harmonics; gold toroidal mirror, TM and differential pumping chamber, DP.

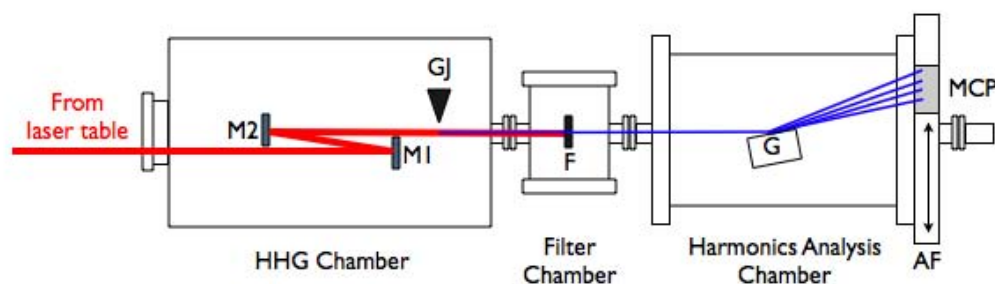


FIGURE 3.9: Diagram of HHG imaging technique: Side view of the HHG process and measurements. The off-axis parabolic mirror, M1 creates a focus of the fundamental beam at the gas jet, GJ. A 200 nm Al filter, F removes the fundamental and selects a range of harmonics. The grating, G imaging microchannel plate MCP for imaging of harmonics; gold toroidal mirror, TM and differential pumping chamber, DP.

on the surface. Figure 3.9 shows a side view of the vacuum beamline. After the filter chamber, the beam entered an analysis chamber. During experiments the beam simply passed through this chamber onto the next where it could be focussed onto the surface. A grating at the base of the analysis chamber (labelled G in Figure 3.9) was attached on a motorized stage and could be controlled from outside the vacuum allowing it to be raised into the path of the beam. The grating separated individual harmonics along the vertical axis, those with lower energy were reflected by a greater angle so were observed furthest away from the initial laser axis. The line spacing of the grating was not constant so that the focal

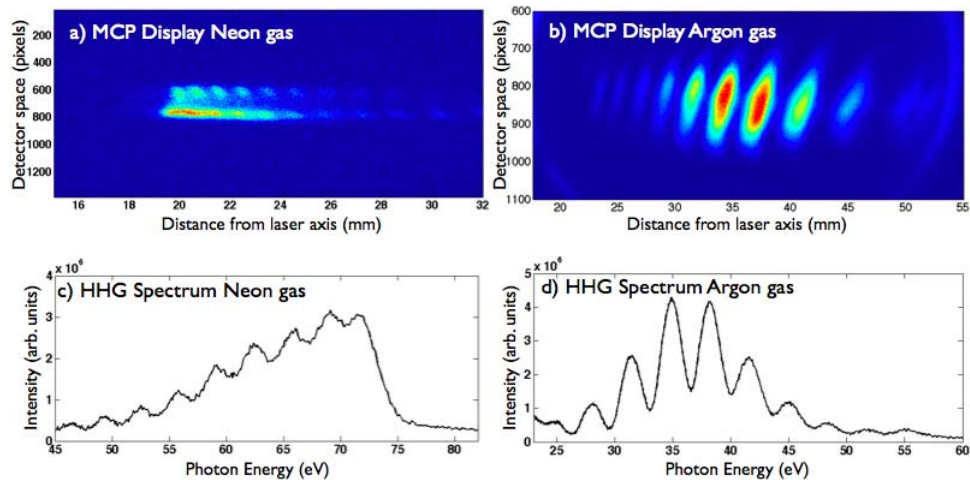


FIGURE 3.10: HHG measurements taken using a flat field spectrometer: Higher order harmonics generated using neon gas created a visible cut-off point at 73eV , the upper transmission limit of the Al filter. (a) Harmonics generated by neon gas, raw MCP data (c) Neon harmonics in eV. This cut off point was used to calibrate the measurements of harmonics generated in argon. (b) Harmonics generated by argon gas, raw MCP data (d) Energy spectrum of harmonics generated in argon gas.

point of each harmonic was imaged along the same plane and could therefore be measured using a standard flat imaging MCP with a phosphor screen. The MCP image was then recorded using a CCD camera. The MCP itself was mounted on a differentially pumped flange which could be moved along the vertical axis to allow a wide range of harmonic energies to be imaged.

Typical measurements taken by the MCP are shown in Figure 3.10 (b). To extract useful information from such an MCP image it was necessary to identify which peak corresponded to which harmonic. For calibration purposes neon gas was used to generate harmonics (Figure 3.10 (a)) and the harmonics transmitted by the Al filter were observed and recorded. The HHG spectrum for neon extends to significantly greater energies than that of argon [100]. At these energies it was possible to observe the upper cut-off of the Al filter which was known to appear at 73 eV [101]. The position on the MCP screen (distance from the initial laser axis) could then be converted to photon energy in eV. The resulting HHG spectra

are shown in Figure 3.10 (c) (neon) and (d) (argon). From the argon spectrum of harmonics used in the experiments it can be seen that the four strongest harmonics incident on the surface are the 21st (32.5 eV), 23rd (35.6 eV), 25th (38.7 eV) and 27th (41.7 eV).

For a typical experiment, the IR laser energy measured at the entrance to the HHG chamber was 0.235 mJ. Assuming a harmonic conversion efficiency of 10^7 incident photons per harmonic (XUV) photon generated, a filter transmission of 30% and a further loss of 30% (i.e. a transport efficiency 70 %) due to the beamline optics it can be estimated, over the harmonic spectrum that each harmonic order will correspond to 5pJ. Over the HHG spectrum shown in Figure 3.10 (d) this corresponded to 1.7×10^5 photons/sec (~ 170 photons/pulse).

3.2.3 The Surface Science Apparatus

The surface science system was a homebuilt system, constructed at the Nanoscale Physics Research Laboratories, University of Birmingham. It consisted of separately bought, commercial parts, mainly from Omicron NanoTechnology GmbH. As shown in Fig. 3.11 the system comprised of three main sections: The main chamber, where photoexcitation experiments were carried out using a Time of Flight (ToF) mass spectrometer; the junction chamber, where surfaces could be treated and prepared and the STM chamber, where samples could be imaged with nanoscale resolution.

During experiments the sample was mounted in the main chamber at the base of a differentially pumped cold finger which could be moved in XYZ directions as well as rotationally. The sample was positioned roughly at the centre of the chamber at the focal point of the laser created by the toroidal mirror (Figure 3.8), such that the ToF was positioned over the laser spot to collect electrons and/or ions at a normal angle of incidence (Figure 3.11).

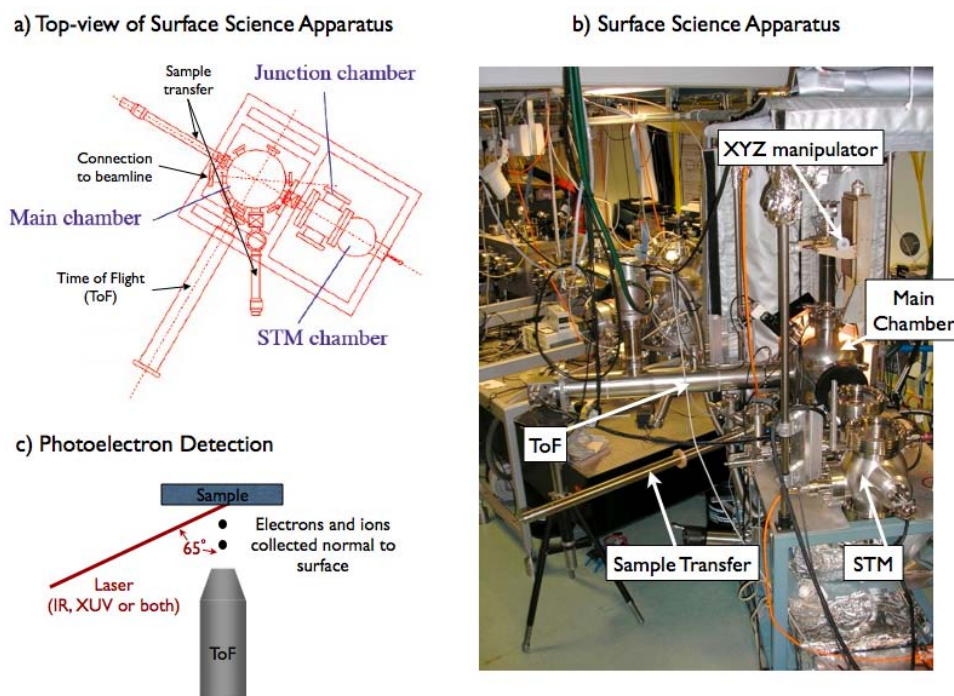


FIGURE 3.11: Surface Science Apparatus: a) Top View diagram: During experiments the sample is located at roughly the centre of the main chamber such that the surface lies at the beam focus and is normal to the Time of Flight. Sample transfer systems including a load lock to allow the sample to be placed inside and moved about the chambers without breaking the vacuum. If required surfaces can be prepared in the junction chamber and imaged using the STM. b) Photograph of the Surface Science Apparatus: Features as before, the XYZ manipulator allows micron scale positioning of the sample in the XY direction, coarse positioning in the Y direction and rotational adjustments. c) Diagram to show Time of Flight detection: Light is incident at a 65° angle with electrons and/or ions detected normal to the surface.

Individual features of the surface science system are described in more detail below:

3.2.3.1 The Time of Flight Mass Spectrometer

The linear time-of-flight (ToF) mass spectrometer is a well established tool for the detection of ions having first been described by Wiley and McLaren in 1955 [102]. For the case of the apparatus used in these experiments, ToF methods can not only be used to detect both positive and negative ions but also to study photoelectrons.

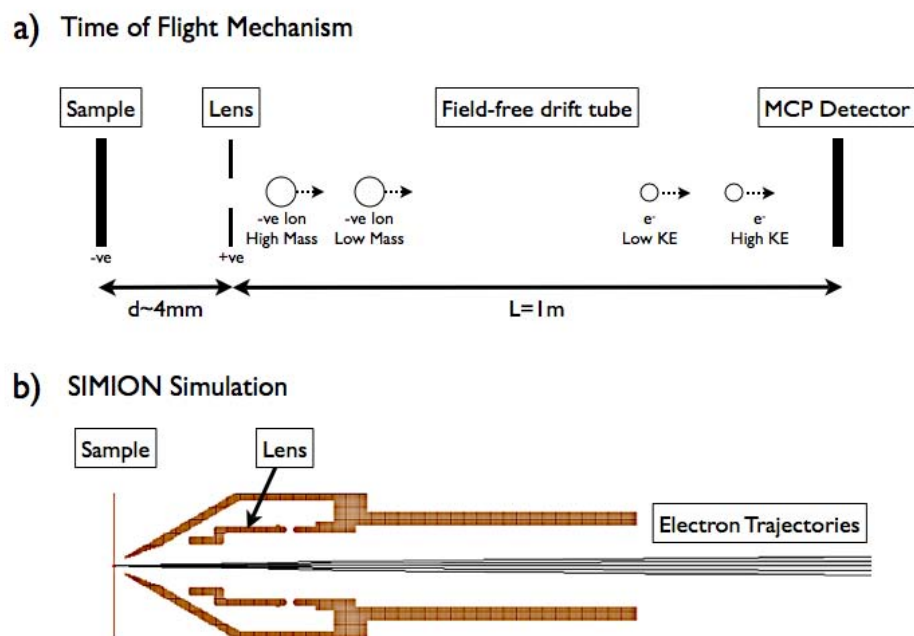


FIGURE 3.12: a) Diagram to show ToF mechanism: Electrons and/or Ions are accelerated away from the sample in the electric field generated by voltages applied to the sample and lens. In the case shown, a -ve sample potential and +ve lens potential facilitates the detection of -ve ions and electrons. Electrons with greater kinetic energy will travel faster in the field free drift tube therefore reaching the detector earlier than their slower counterparts. Similarly Ions with lower mass will arrive before those with higher mass b) Example of SIMION Simulation: 2D cross section of 3D simulation of electron trajectories (electrons shown with angular distribution of ± 2 degrees). The sample is the “initial” position of electrons and the MCP detector (not shown due to scale) is the “final” position. A range of “initial” kinetic energies were used as initial conditions and then the trajectories calculated along with final time of flight values that were then compared to the ToF spectrum.

The principle of ToF is shown in Figure 3.12 (a). Ions and/or electrons are created, in this case by the laser interaction at the surface. Voltages are applied to the lens and sample and the electrons/ions are accelerated by the resulting potential $V = Ed$ where d is the distance between two potentials and E is the electrostatic field created as a result of the voltages applied.

After acceleration, the electrons/ions of mass m and charge, q will have gained potential energy $= qV$ which is converted into kinetic energy as given in Equation 3.1 [103]

$$E_K = \frac{mv^2}{2} = qV = zeV \quad (3.1)$$

The velocity of an ion is therefore:

$$v = \left(\frac{2zeV}{m} \right)^{\frac{1}{2}} \quad (3.2)$$

Once accelerated, the ions/electrons travel through a field free flight tube of length, L. Since they travel at a constant velocity, the time, t taken to travel this distance (shown in Figure 3.12) is given by:

$$t = \frac{L}{v} \quad (3.3)$$

Substituting Eq.3.2 into Eq.3.3 gives:

$$t^2 = \frac{m}{z} \left(\frac{L^2}{2eV} \right) \quad (3.4)$$

Electrons/ions are detected at the end of the flight tube by an MCP detector. From Equation 3.4 it can be seen that that ions with a lower mass/charge ratio will reach the detector before those with a greater mass/charge ratio. For electrons the picture is even more simple, as they all have the same mass, the time of flight depends simply on their kinetic energies with electrons with the greatest kinetic energies arriving first. For the experiments reported in this thesis, the primary interest was electrons so very small voltages were used, typical values of +6 V for the lens and -1.8 V for the sample were chosen to maximise signal and resolution but minimise any distortion effects. (NB to observe positive ions it was possible to reverse polarities).

The apparatus used was a Linear Time of Flight mass spectrometer with a 1m long drift tube, bought from KORE Technology Ltd. A long drift tube gives higher resolution measurements but if made too long this can be at the expense of collection efficiency due to collisions/scattering/dispersion [103]. A Mu metal shield was fitted around the drift tube to minimise any magnetic effects and the separation between the ToF entrance and the sample ranged between 3mm-4mm. A dual microchannelplate (MCP) was used to detect ions /electrons which were then recorded over time by a multiple event time-to-digital converter (P7887 board by FAST Com Tec). The resolution of the transient recorder (time to digital converter) was 250 picoseconds. The actual resolution of the time of flight spectrum (counts vs. time of flight) was given by the time response of the pre-amplifier of the MCP. This gave an error on the time of flight reading of ± 1.5 nanoseconds [104].

SIMION simulations were used to extract the kinetic energies of electrons leaving the surface from the time of flight spectrum. A 3D scaled diagram of the ToF set-up (viewed as a 2D cross section) was created including the lens, entrance aperture, sample and MCP detector. “Potentials” were applied to the sample and lens pieces (the electrodes) so that the electric fields present in the experiment could be calculated. Initial conditions for the charged particles could be set eg. position, energy, angles etc. so that their trajectory in the presence of the calculated field could be determined and hence the arrival times (time of flight) calculated. The calculated arrival times were matched with the corresponding initial conditions to determine which kinetic energies they corresponded to. A matlab program (based on initial LabView programs written by Dr. Miklos Lenner) was written to convert the ToF spectrum into a kinetic energy spectrum. This included a factor of ToF^3 , required by the Jacobian transformation such that the total yield in ToF is equal to that in KE ie. $|f(t)dt| = |f(E)dE|$

For time of flight experiments it was possible to use either p-polarised or s-polarised

light. This was adjusted using a high bandwidth ultrathin zeroth order half wave plate on the laser table where horizontally/vertically polarised light at the laser table corresponded to p/s polarisation at the surface.

3.2.3.2 Surface Preparation Techniques

The HOPG surface was prepared by cleaving of the top layers using adhesive tape immediately prior to its introduction to the main chamber.

A small load lock chamber and transfer arm that could be separately vented and pumped down to UHV allowed samples to be introduced to the main chamber without destroying the vacuum.

For more complex surfaces the preparation chamber included a sputtering gun bought from LK Technologies which was used for argon sputtering to remove surface contaminants and an Omicron heater stage which could be used for both direct and resistive heating. The preparation apparatus was successfully demonstrated using the $\text{TiO}_2(110)$ and $\text{Si}(111)7\times 7$ surfaces which were prepared using sputtering and resistive heating and direct flash heating respectively. Such surface preparation, particularly involving movement of the sample around the vacuum system is time consuming and cumbersome. This was a deciding factor when choosing HOPG as a sample as well as the fact that the graphite band structure is well understood yet graphite is still a material of current interest particularly with respect to the isolation of graphene [84].

3.2.3.3 Scanning Tunnelling Microscopy

The Scanning Tunnelling Microscope situated in the surface science system was an Omicron UHV STM 1, with a maximum scanning range of $2.3 \mu\text{m} \times 2.3 \mu\text{m}$. The underlying principle of STM involves an atomically sharp tip (usually

made from tungsten) and a conducting surface brought to within angstroms of each other. At this separation, when a voltage bias is applied across the gap electrons may tunnel either from the tip to the sample or vice versa depending on the direction of the bias. The current across the gap will decay exponentially such that a small change in separation will have a great effect on the magnitude of the current. Movement of the tip (or the sample depending on STM model) can be controlled using piezoelectric transducers which expand or contract when a voltage is applied. Applying a combination of a sawtooth voltage and a voltage ramp to the x and y piezo respectively will cause the tip to scan the surface in the xy plane. In constant current mode the current tunnelling across the gap is kept constant by a feedback loop which compares amplified current readings to a reference value. The resulting difference is used to drive the z-piezo which will expand and contract, moving the tip towards or away from the surface depending on surface protrusions. The z-piezo movements are recorded over the xy scan producing what can be described as a topographic representation of the surface. In constant height mode the tip-sample separation distance is kept constant. This has advantages as scans are faster, however, this can only be used when the surface corrugation is less than 1 nm. In fact, in either constant current or constant height mode this is an over simplistic explanation as the tunnelling current depends not only on the topography of the surface but also on its electronic structure.

3.2.3.4 Ultra High Vacuum Techniques

The surface science system operated at an ultra high vacuum of 4×10^{-10} mbar however when open to the beamline a pressure of only 1×10^{-9} mbar could be reached. Maintaining a good vacuum is particularly important when studying reactive surfaces. A decrease in pressure results in an increase in the mean free path of molecules inside the chamber, as this happens, the chance of molecules colliding with the surface will decrease. The pressures of 1×10^{-9} mbar attainable

when open to the beamline were a contributing factor to the choice of surfaces used.

The vacuum was maintained using a variety of vacuum pumps. Initial evacuation of the system was achieved using two turbo molecular pumps (one on the main chamber and one on the ToF flight tube) both backed by a shared rotary pump with an oil trap attached. The backing line reached a pressure of about 10^{-2} mbar whilst the turbo pump could reach and maintain a chamber pressure of 10^{-8} mbar. The transition between high vacuum and UHV was accomplished using ion pumps. These consist of an anode and a cathode (usually titanium) with an electric and magnetic field applied. Free electrons ionise incoming gas molecules and as positive ions hit the cathode titanium is sputtered forming a film on the anode. Titanium will react with all ionised gas molecules and the stable molecules formed will be captured on the walls of the pump, anode and cathode.

A titanium sublimation pump (TSP) was used in addition to the ion pumps to reach a lower working pressure primarily by remove hydrogen which, due to its small size is not effectively removed from the system by other varieties of pump. Unlike the other pumps on the system the TSP was not used continuously but was used either on a when needed basis or programmed to be used after certain time intervals (e.g. 24 hours). The mechanism uses a titanium filament which when heated produces a vapour of titanium which will react with active gas molecules present in the chamber. The stable products of this reaction are embedded on the walls of the chamber.

Bake out heaters, heating tape and heat shields were used to bake the system (at 150°C) to remove water present inside the chamber after exposure to air e.g. during maintenance.

3.2.4 The Attenuation of Ultrashort Pulses

The photoelectron spectra presented in the following section were found to be highly dependent on laser intensity and as such a brief description of the experimental method used to vary the laser intensity is given here.

As previously discussed (page 12), the large bandwidth of ultrashort pulses makes them particularly susceptible to material dispersion leading to temporal broadening. This means that traditional optical methods to attenuate the laser power such as neutral density filters are unsuitable. Using a trick of polarisation by reflection (Figure 3.13b)) it was possible to control the intensity of the laser on the surface using only a reflective surface and an ultrathin (broadband suitable) half wave plate.

An extra beamline set up was constructed between the exit of the laser table and the entrance to the HHG chamber. The IR fundamental was incident on a reflective surface of a prism at Brewster's angle as shown in Figure 3.13 a). A prism was chosen as it had a large surface area, which was required to cover the whole beam spot at grazing angles and because it could be mounted easily on a rotatable stage. At an incident angle of Brewster's angle all of the light reflected from the prism surface is s-polarised (Figure 3.13 b). An ultrathin half wave plate ($1\text{st } \lambda/2$) was placed before the prism so that the polarisation of the incident laser beam could be adjusted. When the half wave plate was set to transmit mostly s-polarised light, the light reflected from the prism was maximal. If the half wave plate was set to transmit p-polarised light the reflected signal was minimal as there was little or no s-polarised light incident to be reflected. Rotating the half wave plate between the minimum and maximum points allowed the amount of s-polarised light incident and hence the intensity of the reflected light to be adjusted on a continuous scale. A second half wave plate could be used to adjust the polarisation of the beam to that required for the experiment, this was checked using a piece of Polaroid.

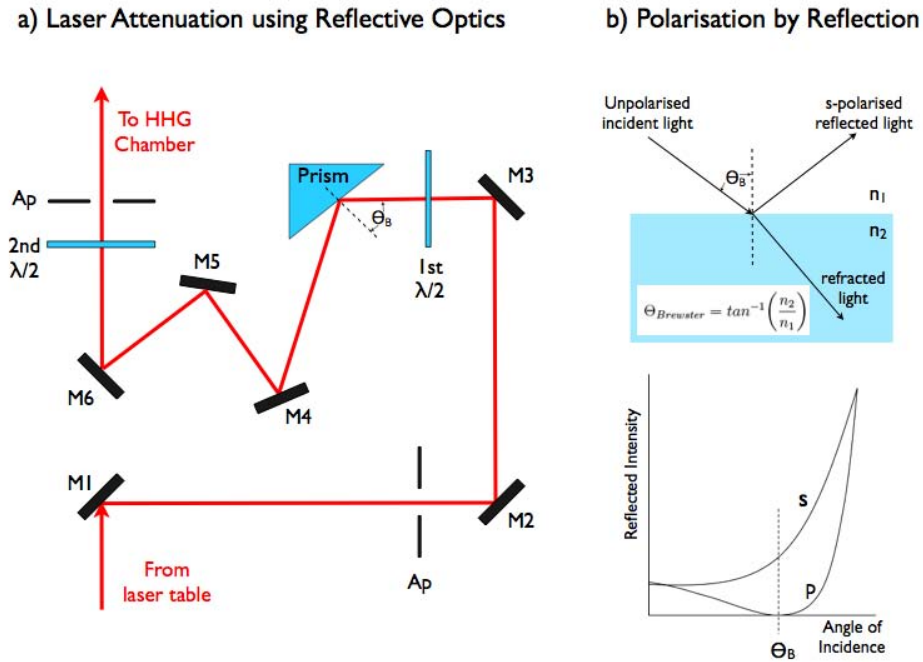


FIGURE 3.13: Attenuation of Ultrashort Pulses using Reflective Optics: a) Schematic Diagram of Attenuation set up placed in-between the output of the laser table and the entrance to the HHG chamber. The first half wave plate (1st $\lambda/2$) controls the laser intensity reflected from the prism (see main text for more details) and the second half wave plate (2nd $\lambda/2$) can then be used to change the polarisation of the light. Adjustable apertures (Ap) and multiple mirrors (M1-M6) were required for accurate beam-pointing along the vacuum beamline. b) (upper) Conditions for Brewster's angle at which all reflected light is s-polarised, (lower) Reflected intensity of s-polarised and p-polarised light as a function of incident angle.

3.3 Photoelectron Spectroscopy Measurements Using 13fs Infra Red Laser Pulses

3.3.1 A Description of the Photoelectron Spectra

The photoelectron spectrum of the HOPG surface produced by photons of 1.55 eV energy was found to consist of three main features. It was immediately apparent that the two features corresponding to highest kinetic energies occurred at significantly higher energies than might be initially expected for a surface with a work function of 4.5 eV illuminated by photons of only 1.55 eV. Figure 3.14 and Figure

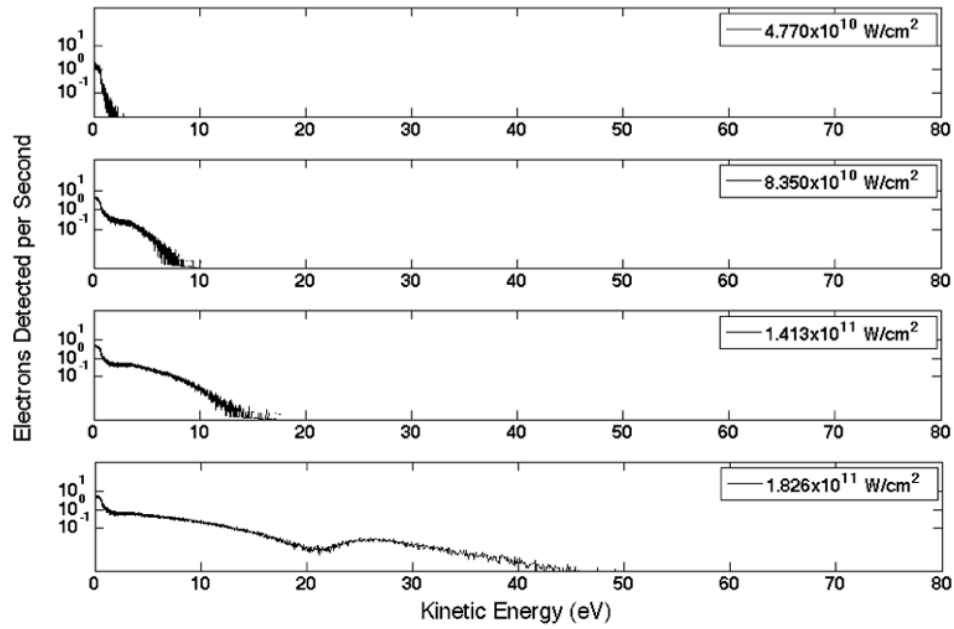


FIGURE 3.14: Photoelectron spectra from the HOPG surface generated by p-polarised infra red laser pulses with a photon energy of 1.55 eV and 13 fs pulse duration. The four spectra shown correspond to different laser intensities

3.15 show the development of the three features in the spectrum with increasing laser intensity for light that is p-polarised and s-polarised respectively. A log scale has been used in the figures so that all three features may be viewed on the same axis although it should be noted that on this scale each feature (i.e. each peak in the spectrum) appears as a broad continua.

Taking first of all the case of p-polarised light: At a laser intensity of 4.77×10^{10} W/cm² (Figure 3.14, upper plot) the first peak in the photoelectron spectrum was observed at a kinetic energy of 0.3 eV. At higher laser intensities (of 6.42×10^{10} W/cm² and above) a second feature appears in the spectrum corresponding to electrons with a peak kinetic energy of 3.5 eV. With a further increase in laser intensity the centre of gravity of this band of photoelectrons is found to shift towards higher energies (of up to 6 eV). The first peak is also seen to shift slightly from $\sim 0.3\text{eV}$ to $\sim 0.4\text{eV}$.

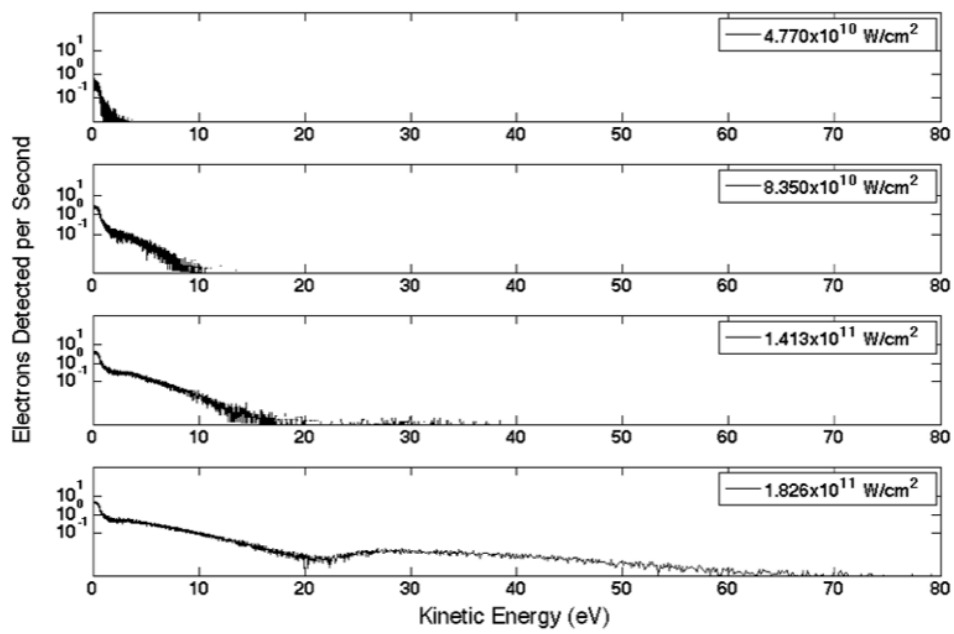


FIGURE 3.15: Photoelectron Spectra taken at the HOPG surface generated by s-polarised infra red laser pulses with a photon energy of 1.55 eV and 13 fs pulse duration. The spectra shown correspond to the same four laser intensities as in Figure 3.14

The third and final feature in the photoelectron spectrum corresponds to photoelectrons with a peak kinetic energy of 26 eV and appears at a threshold intensity of $1.55 \times 10^{11} \text{ W/cm}^2$. It is seen to grow rapidly with increasing laser intensity. At the highest laser intensities the tail of this “fast electron” peak was found to extend to kinetic energies of up to 45 eV. The apex of the “peak” could be sensibly judged with an accuracy of $\pm 0.5 \text{ eV}$. This is greater than the uncertainty introduced by the equipment which is estimated at $\pm 0.3 \text{ eV}$ as shown in Appendix C.

For the case of s-polarised light (where the electric field oscillates only in the plane of the surface) three distinct bands are also seen in the PES. The peaks of each band were found to occur at kinetic energies of 0.3 eV, 3.5 eV, and 28 eV. As described above for the previous polarisation and in Appendix C, the energy measurements for the “fast” electron feature carried an uncertainty of $\pm 0.3 \text{ eV}$ although this was overshadowed by the human error in deciding the peak value

which was estimated at ± 0.5 eV. For this polarisation, at the lowest intensity of 4.77×10^{10} W/cm² the two features at 0.3 eV and 3.5 are already visible. As in the previous polarisation these two features at lower kinetic energies can be seen to shift slightly with increasing laser intensities to kinetic energies of up to 0.4 eV and 5 eV. The “fast electron” peak at 28 eV kinetic energy (a slightly higher peak energy than the p-polarised case) appears at the lower threshold laser intensity of 1.2×10^{11} W/cm² and has a tail extending to even higher kinetic energies of up to ~ 80 eV.

It should be noted that all laser intensities used in these experiments were below the threshold for ion emission/ablation which occurs at 1.3×10^{12} W/cm² for the HOPG surface [105, 106].

3.3.2 Nonlinearity Calculations

Photoelectron spectra were taken at a total of 11 different laser intensities ranging from 4.77×10^{10} W/cm² to 2.10×10^{11} W/cm² (some of which have been displayed in Figure 3.14 and Figure 3.15). This was the maximum possible range using the reflective attenuation method.

At each laser intensity, the area under each peak of the spectrum (the integrated yield) was measured. Since the photoelectron yield Y is proportional to I^N where I is the laser intensity and N the number of photons involved in the process, the nonlinearity of the excitation process (the number of photons involved) was extracted from the data by plotting log of the integrated yield verses log of the laser intensity. This resulted in a straight line with a gradient equal to the nonlinearity of the process as described by the following relationship:

$$\log Y - \log Y_0 = N(\log I - \log I_0) \quad (3.5)$$

where I and I_0 are two values of the laser intensity and Y and Y_0 are the corresponding values of the photoelectron yield (ie. $\log Y - \log Y_0$ and $\log I - \log I_0$ are the change in the y-axis and the change in the x-axis respectively, as required to take the gradient).

The relationship between photoelectron yield and nonlinearity is well known [107] and comes from a simple power law which states that the ionisation rate for an N-photon transition is proportional to the Nth power of the laser photon flux Φ , where Φ is the laser intensity divided by the photon energy [108]. This N-photon ionisation rate is given by:

$$R_N = \sigma_N \Phi^N \quad (3.6)$$

where σ_N is a generalised cross section with units of $\text{cm}^{2N} \text{s}^{N-1}$. The probability of ionisation is therefore given by [108]:

$$P = \int R_N(t) dt \quad (3.7)$$

For a pulse duration, T the following is true

$$P \approx \sigma_N T \Phi^N \quad (3.8)$$

and thus if the photoelectron yield is considered to be proportional to the probability of ionisation, the cross section, pulse duration and photon energy are constant, the relationship in Equation 3.5 can be obtained from Equation 3.8.

The log-log plots are shown in Figure 3.16 for both p and s-polarised light and for each of the three features in the PES. For the case of the lowest energy feature (blue crosses in Figure 3.16) the nonlinearity of the excitation process appears

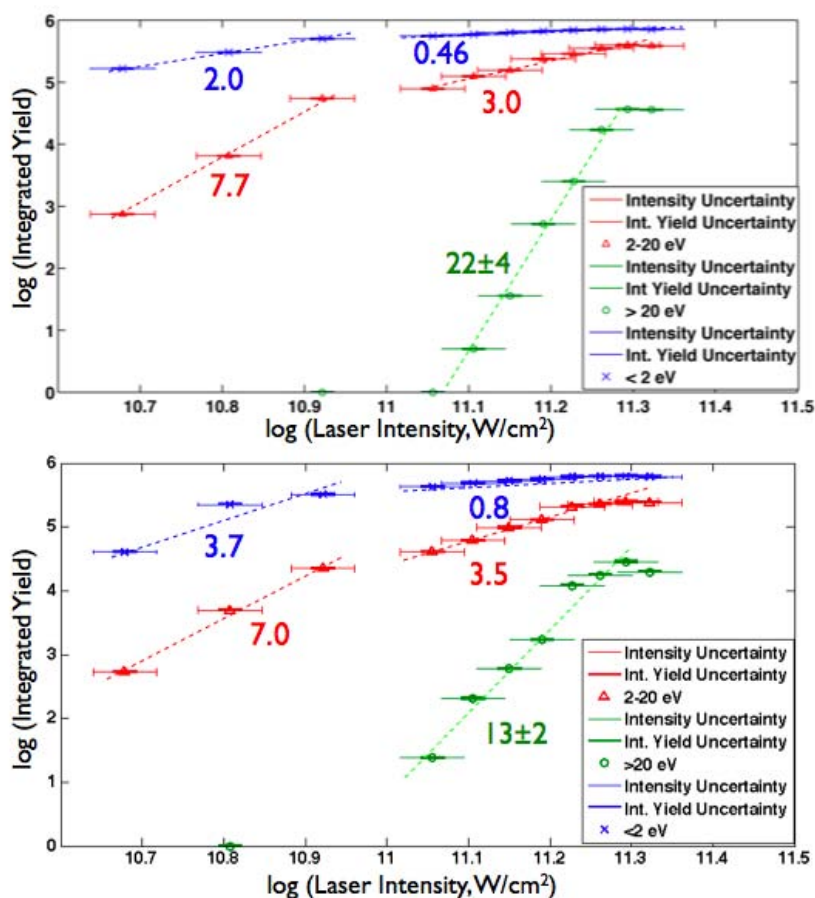


FIGURE 3.16: A plot of the Integrated yield of each peak versus the laser intensity (a) p-polarised light (b) s-polarised light. The integrated yield is shown for three energy ranges of 0-2 eV (blue), 2-20 eV (red) and >20 eV (green) corresponding to the three features observed on the photoelectron spectrum. When plotted on a log/log scale a linear fit of the gradient gives an estimate for the nonlinearity of the process giving rise to each feature. Vertical error bars show the uncertainty of the energy measurement (i.e. the error in choosing the limits over which to integrate) and the accuracy of the MCP (taken from the accuracy of the gain applied). Since these errors are relatively small, the upper and lower limits are only just visible. Error bars on the x axis correspond to the uncertainty of the intensity measurements as discussed in Appendix C.

to be 2nd and 4th order for p- and s-polarised light. Once the laser intensity reached the threshold for the “fast electron peak” (the 26eV/28eV peak) however the nonlinearity of the lowest energy feature is found, for both polarisations, to reduce to a value of less than one. The same is seen for photoelectrons in the mid-energy feature where nonlinearities drop from 7.7 ± 0.09 (6.7 ± 0.07) to 3.0 ± 0.03 (3.5 ± 0.03) for p-polarisation (s-polarisation). For the case of the “fast electrons” nonlinearities calculated suggest a 22-photon process (22 ± 4) for p-polarised light and a 13-photon process (13 ± 2) for s-polarised light. Errors were calculated using residuals from the linear fit. By taking the photoelectron yield as the integrated area under each peak these results give the value for nonlinearity averaged over the whole peak. It was found however, for the case of the “fast electrons” that if smaller integrated sections were taken as slices within each peak and the process repeated for each slice, the nonlinearity measured for each slice increased with photoelectron kinetic energy within the peak.

The implications of these nonlinearity measurements are discussed in the context of the known band structure of graphite on page 78.

3.3.3 Pulse Duration Dependence of Photoelectron Measurements from the HOPG Surface

As shown by Kupersztych et al. [41] and described in more detail previously in the theory section (page 27) photoelectrons generated by multiphoton excitation may be accelerated in the ponderomotive field produced by a plasmon at the surface. In order ascertain whether such a process could be responsible for the high kinetic energies seen from the HOPG surface the effect of pulse duration on the photoelectron spectrum was tested.

Figure 3.17 shows the difference between spectra produced by 10 fs pulses (red) and 30 fs pulses (black) of equal laser intensity. Both s and p-polarisations are

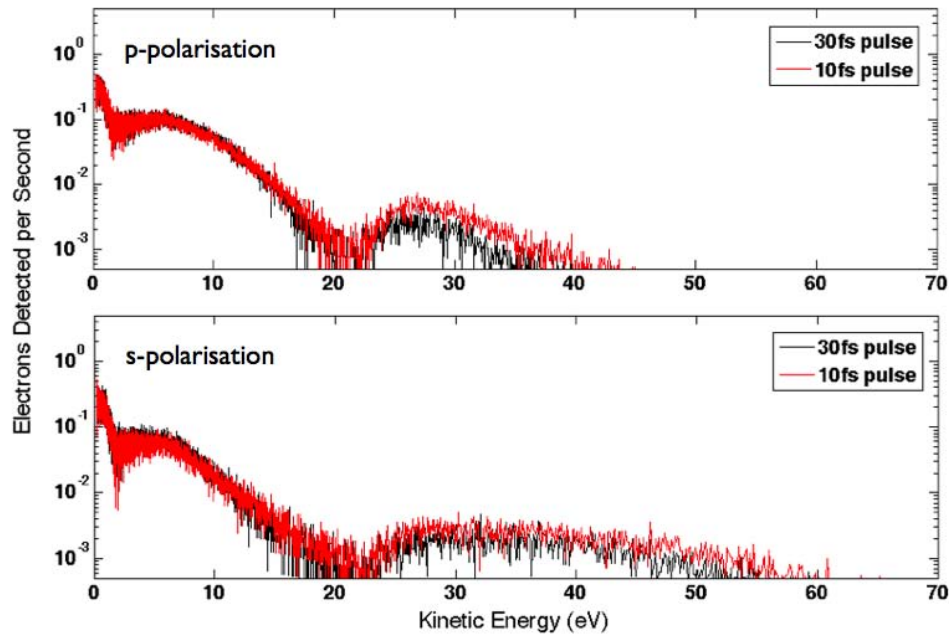


FIGURE 3.17: Photoemission from the HOPG surface taken by pulse durations of 10 fs and 30 fs. The laser intensity remained constant at $1.6 \times 10^{11} \text{ W/cm}^2$ for all measurements shown. The upper panel depicts spectra taken using p-polarised light and the lower panel depicts spectra taken using s-polarised light.

shown. Since the 10 fs pulse corresponds to ~ 4 cycles of the laser and the 30 fs pulse to ~ 11.5 cycles it would be expected that if the electron energies observed were a result of ponderomotive acceleration then the “fast electron” peak in the spectrum corresponding to 30 fs pulses would occur at higher kinetic energies. Kupersztych et al. show just this, that doubling the pulse duration results in a significant shift of a peak to higher photoelectron energies. This is not consistent with the HOPG results where the pulse duration appears to have little effect on the photoelectron spectrum. If anything the shorter 10 fs pulses appear to generate photoelectrons with very slightly higher kinetic energies. This is most probably due to the higher peak power of the shorter pulse as equal energy is compressed into a shorter pulse duration.

Ponderomotive effects can therefore be ruled out as the main cause of the high kinetic energy electron peak. The nonlinearity measurements for HOPG are also in agreement with this assumption because nonlinearity calculations undertaken

in other investigations for electrons excited by ponderomotive acceleration have shown that the number of photons involved in the excitation process are equal to that required to overcome the work function [22]. In our case the nonlinearity values measured are significantly greater.

3.4 Photoelectron Spectroscopy Using XUV Pulse Trains

XUV harmonic pulse trains, as described in the Technical Background section (page 55) were also used to excite the HOPG surface. Figure 3.18 (a) shows the photoelectron spectrum generated by the XUV pulse trains. Figure 3.18 (b) shows the spectral profile of the XUV pulses. As in the IR case this spectrum was found to be made up of three distinct features. The peaks of these three features occurred at kinetic energies of 0.4 eV, 5 eV and 24.5 ± 0.5 eV (uncertainty of measurement as described in the previous section and in Appendix C).

It is immediately obvious that a striking similarity exists between this spectrum and that taken using IR photons (Figures 3.15 and 3.14). It is therefore possible to use this photoelectron spectrum to provide more information on the IR photoelectron spectrum. It is more reasonable in this case that photons with energies of ~ 36 eV can generate photoelectrons with ~ 25 eV energy. This raises the question of whether conduction band state(s) much above the Fermi level, which may be reached by a single XUV photon, may also be accessed in the short pulse/strong field regime by IR photons with energy of only 1.55 eV. This will be discussed further in the subsequent sections as will possible mechanisms for such a transition in relation to the known band structure of graphite. It is however worth noting at this point that a multiphoton transition of non-linearity 22 as measured for the p-polarised IR case would correspond to a total excitation energy of $22 \times 1.55 = 34.1$

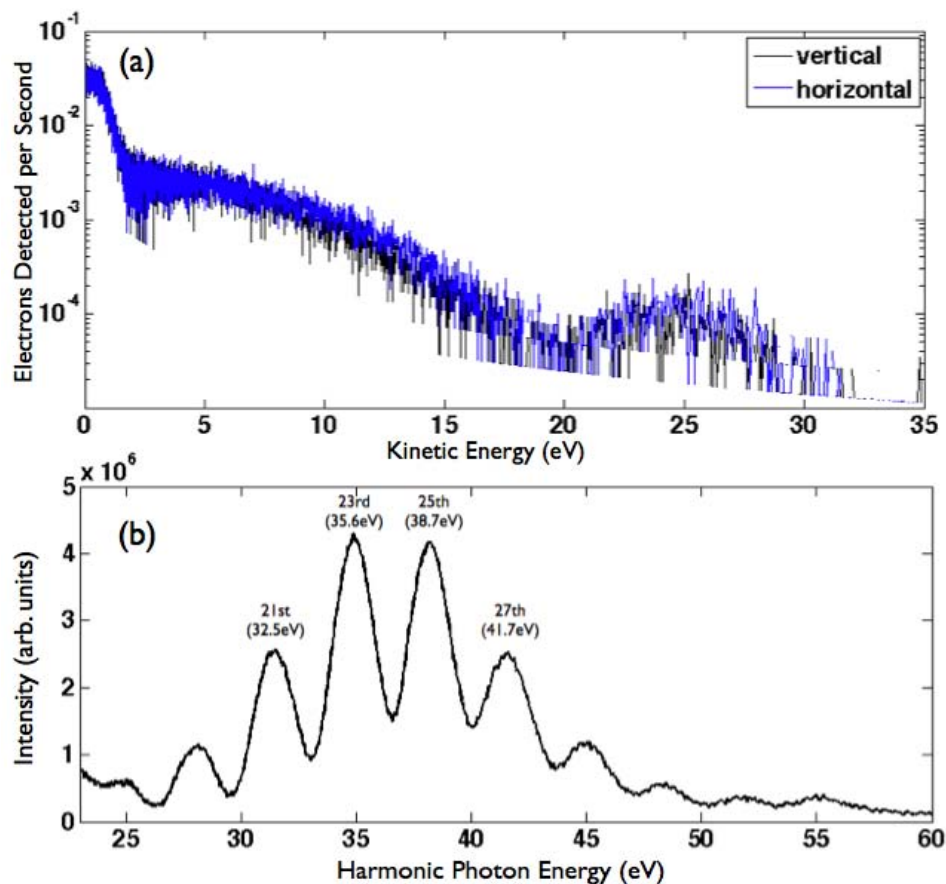


FIGURE 3.18: (a) Photoelectron spectra of the HOPG surface produced by XUV pulse trains generated by HHG using argon gas. "Vertical" corresponds to s-polarised light and "horizontal" corresponds to p-polarised light. (b) XUV harmonic spectrum i.e. photon energies incident on the surface.

which is of similar value to the main harmonic contributions to the XUV photons of 35.6 eV and 38.7 eV.

It might be expected that the XUV photoelectron spectrum might show some signature of the spectral profile of the XUV pulses (Figure 3.18(b)). For experiments in the gas phase where a train of harmonics has been used to excite the medium it is commonplace to observe repeated features in the photoelectron spectrum [109]. These could not be distinguished in the spectrum shown in Figure 3.18(a). Since the range of kinetic energies observed in the photoelectron spectrum is comparable with the spectral range of the envelope of the XUV harmonics it is possible that

such effects would be seen if a greater XUV signal could have been used. Alternatively, since the photoelectron spectrum depends not only on the spectral profile of the XUV pulses but also the density of states of the initial state and that of the final state it is possible that the signature of the harmonics could be smeared out by the initial, occupied state in the valence band of graphite which is extremely broad in energy [90].

3.5 Analysis and Discussion of the Photoelectron Spectra taken at the HOPG Surface

3.5.1 Comparisons with Band Structure

In this section the photoelectron spectra taken are compared with the known band structure in an effort to identify the initial and final states of the three peaks observed in both the XUV and IR case and to attempt an explanation for the striking similarity between the two. The band structure of graphite is well studied both theoretically [86, 89, 91, 110] and experimentally [82, 83, 88, 111]. For analysis of the photoelectron spectra, the work of Willis et al. [112] was particularly useful as one of the few papers where the band structure was calculated for energies of up to 50 eV (relative to the Fermi level).

Figure 3.19 shows the bandstructure of graphite as published by Bianconi et al. [90]. This is based on the calculations of Willis et al. [112]. The scale on the horizontal axis of the band structure plot corresponds to distance along the Brillouin zone (in \AA^{-1}). A direct comparison is made in the figure to the photoelectron spectra taken and highlighted sections mark areas of the band structure which match up to the peaks in the spectrum.

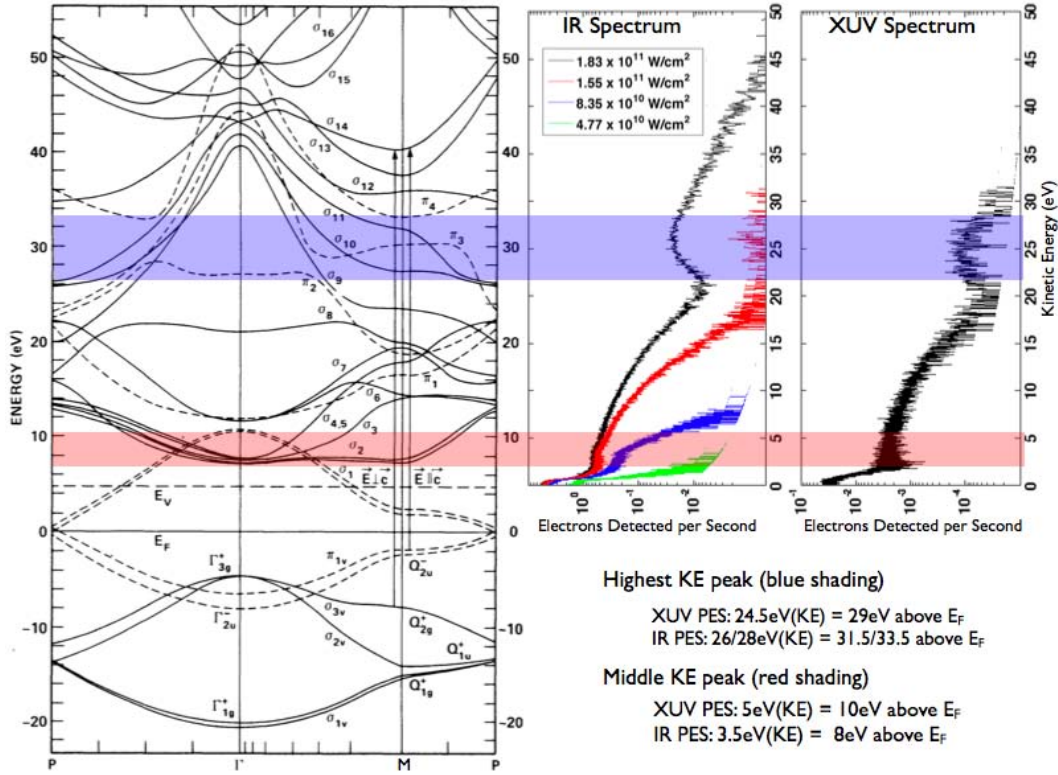


FIGURE 3.19: Comparison of photoelectron spectra and known band structure. The calculated bandstructure shown is taken from [90] the arrows indicate an example of transitions to higher final states than observed in our experiments. The blue shaded area highlights unoccupied states corresponding to the highest kinetic energy peak in the photoelectron spectra. The red shaded area highlights those states corresponding to the mid-kinetic energy peak observed at 3.5 eV in the IR spectrum and 5 eV in the XUV spectrum.

Taking first of all the case for the photoelectron spectrum generated by XUV light: For the highest kinetic energy peak at 24.5 ± 0.5 eV, if the photon energy is taken to be that of the strongest harmonic contribution (the 23rd harmonic of energy ~ 36 eV), the origin of the photoelectron can be calculated as the photon energy minus the kinetic energy of the electron minus the work function of graphite (4.5 eV [29]) i.e. $36\text{eV} - 24.5\text{eV} - 4.5\text{eV} = 7\text{eV}$. There is an occupied state, the π minimum which lies 7 eV below fermi level, at the Γ point to which this could correspond. Although there is no unoccupied state in the conduction band at 29 ± 0.5 eV (24.5 eV + work function) at the Γ point, there is π state at the slightly lower energy of 27 eV, lying 1.5 eV outside of the uncertainty limits. Taking into

account the work function, the π band at M-point on the Brillouin zone is therefore a better fit to the kinetic energies of 24.5 ± 0.5 eV observed in the “fast electron” peak. It should be noted that in older papers this part of the Brillouin zone is referred to as the Q point but in more recent papers it is commonly referred to as the M point [29, 91]. Thus, throughout this thesis the more modern notation will be used. For this case where the photoelectrons originate from the M point it can be assumed that the initial state would be the π band lying ~ 3 eV below the Fermi level at the M point. This point on the Brillouin zone is known to be where the greatest density of states occurs in the valence band [82] and as such would be the most likely site in the valence band from which electrons could be excited. At the lower end of the XUV spectrum, the 21st harmonic has energy of 32 eV. For a transition starting from the M point 3 eV below the Fermi level this would produce electrons of KE 24.5 eV ($32 \text{ eV} - 4.5 \text{ eV} - 3 \text{ eV} = 24.5 \text{ eV}$). It is therefore thought that the photoelectron signal most likely corresponds to a transition from the M point. However, since a potential transition at the Γ point lies just outside of the experimentally observed energies it should not be totally discounted.

In Figure 3.19 the red highlighted section shows the parts of the band structure which could correspond to the middle energy peak at ~ 5 eV. Previous angle resolved photoemission experiments [83] using a synchrotron source have measured a very strong secondary electron signal at 3.5 kinetic energy which is well known to correspond with to the Γ point at 8 eV above the Fermi Level. For a photon energy of 35 eV Law et al. [83] also observed a weaker secondary electron feature at 10 eV above the Fermi level which fits well with the position of the peak in this thesis. The lowest KE feature can be interpreted as the ‘cascade maximum’ which is not a feature of the band structure but is a secondary electron feature due to inelastic scattering of electrons [113].

Moving on to analysis of the infra red photoelectron spectrum, the measurements of nonlinearity can be used to provide a total photon energy for the transitions.

For the “fast electron” peak at 26 ± 0.5 eV (p-polarised light) nonlinearity measurement suggested a 22 photon excitation process. This would correspond to a total energy of 22×1.55 eV = 34.1 eV. Taking into account the work function of graphite, this would correspond to an initial state 3.6 ± 0.5 eV below the Fermi level ($34.1 - 26$ eV(peak) - 4.5(work function) = 3.6 eV). Again this matches well with the pi band at M point where the greatest density of states occurs. For s-polarised light the energies and nonlinearity involved do not match up. Instead, the calculated nonlinearity of 13 would give a total photon energy of just 13×1.55 eV = 20.15 eV which would correspond to an initial state already in the conduction band. Failure of an agreement between the nonlinearity measurements and the photoelectron energies indicates that for s-polarisation unlike p-polarisation a simple multiphoton analysis cannot be applied.

Initially a multiphoton-type approach fits well for the mid energy peak observed at 3.5 eV. The nonlinearity measurements suggest an 8 (7) photon process for p (s) polarised IR light. For a kinetic energy of 3.5 eV a 7 photon process would point to an initial state at ~ 3 eV below the Fermi level (7×1.55 eV = 10.85 eV and 10.85 eV - 3.5 eV - 4.5 eV = 2.85 eV). Again, this matches up well with the M point π band approximately 3 eV below the Fermi Level. The photoelectron energy also matches up very well to a possible final state at the σ band at the M point. Schülke et al. show that for both cases where the electric field acts in the plane and/or out of the plane of the surface this is an allowed transition[114]. Adopting the same approach for an 8-photon process as suggested by the nonlinearity measurements for p-polarised light, the total photon energy, 8×1.55 eV = 12.4 eV gives 12.4 eV - 3.5 eV - 4.5 eV = 4.4 eV which matches up very well with the σ bands that occur at roughly 4.5 eV below the Fermi level at the Γ point. Final states at the bottom of the σ^* band at the Γ point are located 8 eV above the Fermi level, which is again an excellent match with the observed kinetic energy peak at 3.5 eV. Once again these are dipole-allowed transitions [114].

Although this multiphoton picture appears to fit at the lower laser intensities used, the interpretation fails for those intensities above the threshold intensity for the “fast electron” peak. As previously described and shown in Figure 3.16, at this point the gradient of the log-log plot changes suddenly giving a much lower estimate for the nonlinearity. The position of the kinetic energy peak remains constant at 3.5 eV so continues to match up well with the previously mentioned states in the band structure.

Studies at a tungsten surface have shown that for intense IR pulses of a similar intensity to those of this investigation [115] heating of the surface leads to an increased electron temperature. Subsequently, thermal emission can lead to the population of unoccupied states. This could certainly be the cause of the lowest energy photoelectron feature (peak 0.3 eV). This explanation involving thermal electrons is backed up by results from interferometric autocorrelation measurements which will be presented in the next chapter.

It should be noted that the flight times of ions generated at the HOPG surface at laser intensities around and above the ablation threshold were tested. It could be seen from these measurements that even ions with a small mass/charge ratio such as H^- had significantly longer times of flight than the photoelectrons. Since ions were not observed in the measurements described in this chapter, it is not believed that any surface damage, whether sudden or gradual, would lead to the phenomenon observed.

3.5.2 Space Charge

Since space charge effects have previously been cited at the cause of high electrons detected in photoemission experiments [50, 116, 117] it is important to confirm whether or not they could be the cause of the photoelectron features observed at the HOPG surface. An example of a typical shift and distortion of a photoelectron

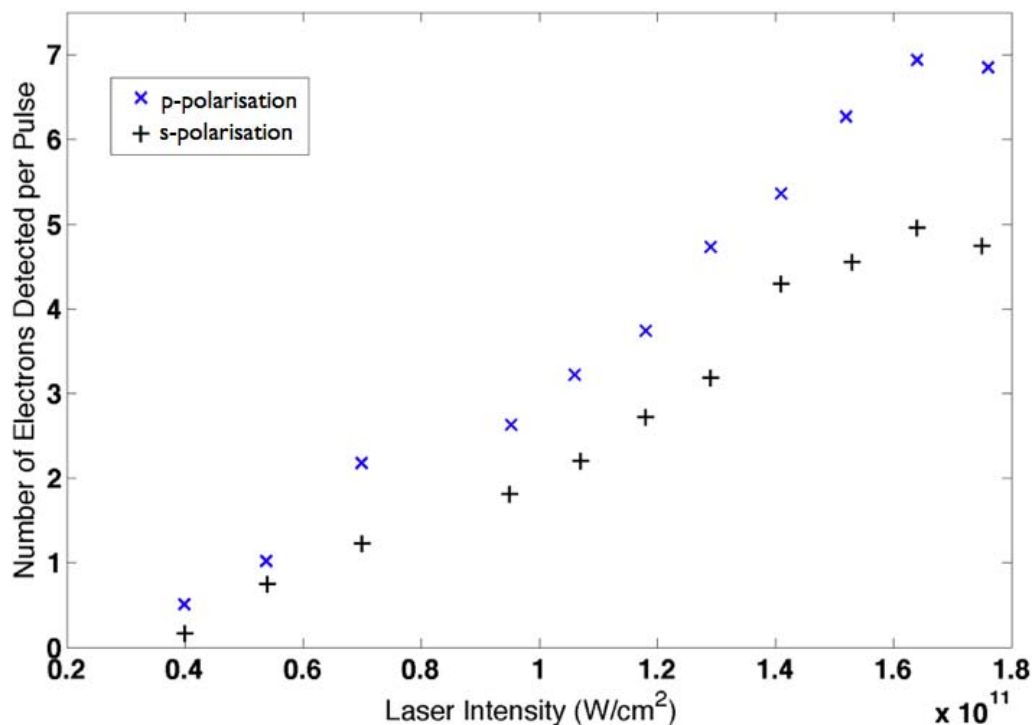


FIGURE 3.20: A plot showing the number of electrons detected by the ToF per pulse with respect to laser intensity. Photoelectrons detected for horizontal polarised light (p-polarisation) are shown in blue, photoelectrons detected for vertically polarised light (s-polarisation) are shown in black

spectrum attributed to space charge effects is that given by Petite et al. [60] as shown in the Chapter 2 on page 30.

It is possible to totally eliminate the possibility of space charge by reducing the intensity of the laser such that only one photoelectron is produced [50] per laser pulse i.e. that there are no other electrons present and therefore no repulsive forces. This is done in many cases for photoelectron studies in metals where the threshold laser intensities for such effects are much lower however it was not suitable for the work presented in this thesis because the fast electron peak which was of most significant interest does not occur at such low intensities.

For the data presented in this chapter, each photoelectron spectrum corresponds to electrons collected over 100,000 laser pulses equating to an average yield per pulse ranging from 0.1 to 7 electrons (Fig. 3.20) with increasing laser intensity. At

the threshold for the 25 eV feature the average yield per pulse of 6 electrons corresponds to a total current density of ~ 0.032 Amp/cm². Barbour et al. [118] showed that the onset of space charge effects occurred at significantly higher current densities of 3.5×10^5 amp/cm². More recently, Riffe et al. [64] reported thermionic electron emission from metal surfaces which they attributed to the presence of strong space charge fields; they measured a current density of 550 amp/cm². It should be noted at this point that the average value of 6 electrons per pulse is an underestimate as it assumes all photoelectrons created are detected however it lies significantly below the threshold current density suggested by Barbour et al. and also below the experimental parameters of Riffe et al.

The development of three separate features seen in the photoelectron data from HOPG shows that the low energy features remain relatively stable with increasing laser intensity, a situation also observed by Belsky et al. [59]. This is not consistent with the space charge effects observed by Petite et al. where the shape of the spectra varies significantly at lower laser intensities depending on laser intensity. As explained by Passlack et al. [116], space charge will lead to a general broadening of the kinetic energies observed which occurs in both directions (i.e. at higher and lower kinetic energies). This is not observed in the HOPG data which, along with the low current density measured leads to the conclusion that space charge effects do not play a significant role in the energies of photoelectrons observed from the HOPG surface.

3.5.3 A Discussion of Different Excitation Mechanisms in Relation to the HOPG Photoelectron Measurements

Suitable states that could give rise to the observed photoelectron features have been identified however the mechanism by which this excitation occurs in the infra red case (where the incident photon energy is just 1.55 eV) is not immediately

obvious. This section discusses the evidence taken from the various photoelectron measurements reported above and draws comparisons with relevant experiments and theory from the literature. The excitation mechanisms reported in the literature are examined separately however it is possible that a mixture of two or more different mechanisms could give rise to the high energy electrons observed from the HOPG surface.

In some of the data taken, particularly for the case of p-polarised light, the non-linearity measurements made match up extremely well with the observed kinetic energies and known band structure of HOPG. This is highly indicative of a multi-photon process. Examining the structure of the photoelectron spectra however the photoelectron features observed could be described as having a smoothed nature. This would be more consistent with a tunnelling excitation process [50] as opposed to a multiphoton process. For a multiphoton excitation process it would be expected that discrete peaks in the photoelectron spectrum would be observed with a separation equal to the incident photon energy [119]. Such features, known as above threshold photoemission (ATP), correspond to the excitation of the same initial state by different multiples of the number of photons.

Theoretical work carried out by Faisal et al. used Floquet-Bloch theory to construct a model of a combined laser-surface system [120] at a standard (non specific) crystal surface. The electron emission spectrum calculated from the field modified band structure is shown in Figure 3.21 for a laser intensity of 3×10^{10} W/cm² (towards the lowest of laser intensities presented in the experimental work of this thesis). This calculated spectrum shows a sequence of individual bands of electrons with energies very similar to the two lower energy features observed in the HOPG experiments. Within these calculated emission bands, they also observed strips of no emission (white bands) with a periodic spacing equal to the incident photon energy. This differs in appearance to ATP which has since been observed experimentally [119] but matches well with the lower two photoelectron features

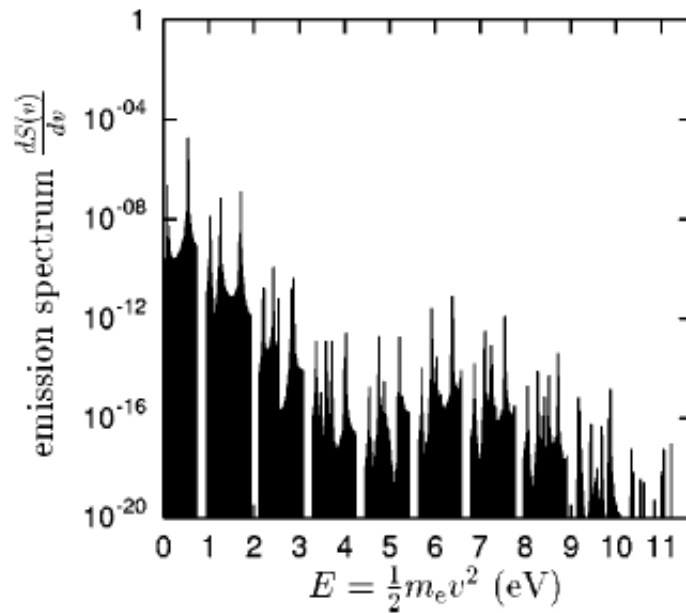


FIGURE 3.21: Above-threshold surface emission calculated by Faisal et al. [120]: A Floquet-Bloch model of the interaction between an intense laser and a crystal surface generates an emission spectrum made up of bands of electron energies with gaps in the emission occurring with a periodicity of the photon energy. The authors find that including the presence of surface electronic band structure results in the generation of greater energy photoelectrons as compared to a standard free-electron model.

observed in the HOPG experiments with the exception of the white gaps. These gaps in the calculated spectrum were found to vanish when the photon energy was less than the width of the initial band from which the electron was excited. This is the case for the HOPG experiments presented in this thesis as the photon energy of 1.55 eV is considerably less than the width of the initial band (photoelectron measurements of the valence band of graphite by Bianconi which show a broad energy range of up to 20 eV [90]). Based on the shape of the features in the photoelectron spectra it is therefore not possible to confirm that the excitation occurs via either a tunnelling or a multiphoton process.

As described previously in the theory chapter (page 15) the Keldysh parameter, γ can be used to distinguish between multiphoton and tunnelling ionisation processes for strong field interactions. Substituting experimental parameters at the threshold

laser intensity for the 26 eV peak into equation 2.11 and using the work function of 4.5eV as the ionisation potential (as is common practice when the Keldysh parameter is calculated for surfaces [119]), the value of γ calculated is 14. Since $\gamma = 1$ marks the boundary between the two processes (values greater than 1 lie in the multiphoton regime and those below 1 lie in the tunnelling regime) [21] this would suggest that the excitation process of interest lies in the multiphoton regime. By substituting $\gamma = 1$ into Equation 2.11 it can be seen that a laser intensity of 3.8×10^{13} W/cm² would be required for a tunnelling process, this is significantly higher than the actual threshold intensity of the fast electron peak at 1.55×10^{11} W/cm². The mismatch between these two laser intensities calculated for tunnelling ionisation can not however be used as definite proof that the excitation process leading to the fast electrons is a multiphoton mechanism until all contributing factors at the surface have been considered:

M. Wegner showed, for the GaAs surface [121] that for semiconductors with $m_e/m_0 \ll 1$ the condition for tunnelling may be reached at the lower laser intensity of 10^{12} W/cm². For the case of graphite $m_e/m_0 = 0.05$ [110]. Using this value for the conduction band effective mass in the Keldysh equation would give a laser intensity of 1.3×10^{13} W/cm² required for a tunnelling process to occur. This value is still greater than that observed experimentally however one effect not yet taken into account is the amplification of the electric field at the surface that could be provided by a surface plasmon [42]. Since the evanescent field of a surface plasmon polariton can lead to a field enhancement of 1-2 orders of magnitude [45] i.e. an increase in the effective laser intensity of up to 4 orders of magnitude ($I = |E^2|$). Substituting these values of the field enhancement into the Keldysh equation shows that the experimental conditions under which these fast electrons are observed lie very much on the border of multiphoton processes vs. tunnelling processes. It is therefore not possible to use the Keldysh parameter to make a conclusive statement as to how the excitation occurs. It should also be mentioned

that in gas phase experiments it has been shown that the two excitation processes are not always mutually exclusive [23].

It should also be noted that the photoelectron spectrum initially appears to show an uncanny resemblance to electron energy loss spectroscopy (EELS) measurements of the HOPG surface. EELS measurements show a peak at $\sim 7\text{eV}$ corresponds to the π plasmon and a peak at $\sim 28\text{ eV}$ corresponds to the $\pi + \sigma$ plasmon [86]. However, once the workfunction of graphite is taken into account as has been described above, the resemblance is no longer strong. Thus it is believed that the electrons observed cannot simply be attributed to a plasmonic effect.

3.5.4 Experimental Evidence for Field Enhancement

At laser intensities such as those used in these experiments that lie below but close to the threshold for ablation, the graphite surface exists in a highly-excited state (excited state carrier concentration of $\sim 10^{20}\text{ cm}^{-3}$). It has recently been shown by Huang et al. [43] that under these conditions the excitation of surface plasmons on the graphite surface is likely. They showed that when the surface is in a highly excited state electrons are excited in abundance and so plasmas are generated at the surface i.e. strong and localised fields are created. This is explained by Weber et al. [42] and on page 22 of the theory chapter where it can be seen that when the condition $\epsilon_2'' \ll -\epsilon_2'$ ($\epsilon_{imaginary} \ll -\epsilon_{real}$) is satisfied amplification of the field occurs. The real part of the dielectric function will be negative for the high excited state carrier concentrations thus the condition will be satisfied. The field enhancement observed at the graphite surface by Huang et al. was found to occur predominantly at intrinsic defects on the surface (or at purposely created nanostructures). As has been discussed in the section above, the generation of such surface plasmon polaritons and subsequent field enhancement at the graphite surface has a significant effect on the analysis of the HOPG data as

it would suggest that tunnelling processes might occur. Grain boundaries (usually at a separation of $\sim 1\mu\text{m}$) formed on the surface by the production of HOPG can act in a similar manner to a grating on the surface. The coupling of light to plasmon polaritons at the HOPG surface can thus be explained by equation 3.9:

$$k_{sp} = k_l + k_{gr} \quad (3.9)$$

where k_{sp} is the wave vector for the surface plasmon and k_l and k_{gr} are those for the laser and grating respectively. They can be expanded to give equation 3.10.

$$k_{sp} = \frac{\omega}{c} \sin \theta + \frac{2\pi}{a} \quad (3.10)$$

where a is the periodicity of the grating and θ is the incident angle of the light. Since the periodicity of defects on the surface is random the coupling efficiency will be low as coupling will only occur when the defects are separated by a distance, a that satisfies equation 3.10.

As described previously in the theory chapter (page 21) p-polarised light may be coupled to surface plasmons polaritons at flat surfaces. It is possible however for localised plasmons occurring at intrinsic defects on the surface to be excited using either s-polarised and p-polarised light. These localised areas of field enhancements are sometimes referred to as hot-spots [54].

A typical characteristic of the photoemission occurring at these hot-spots is that they display a varied polarisation dependence (i.e. different defects at the same surface can couple better to p-polarised light or to s-polarised light [122]). In many cases the photoemission signal from a rough or purposely structured surface is shown to be greatest for s-polarised light [49, 50, 51, 52]. For the HOPG experiments it has been shown that fast electron features occur first at lower laser intensities for s-polarised light than for p-polarised light. Also the photoelectron

spectra produced by s-polarised light extends to higher energy photoelectrons. It is clear from the experiments that the emission of such high energy electrons is more efficient when a larger proportion of the E-field is acting in the plane of the surface. This is highly suggestive that localised plasmons and subsequent field enhancement could be involved.

Nonlinear photoelectron emission is known to occur at these hotspots [51] with strong multiphoton processes [52] and proposed tunnelling excitation [50] being attributed to the localised areas of field enhancement. Hotspots previously generated with similar laser wavelengths occurred on a ~ 1 micron scale [51]. This is significantly smaller than the focussed laser spot which forms an ellipsoid of major axis $1380 \mu\text{m}$ and minor axis $250 \mu\text{m}$ on the surface and given the findings of Huang et al. it is likely that such defects occur within the laser spot.

If such field enhancement is involved in the generation of the high energy electrons observed it is possible that it could be used to explain the polarisation dependence of the photoelectron spectra. It is clear that the fast electron excitation channels are more efficiently accessed by s-polarised light where all of the E-field acts in the plane of the surface than for p-polarised light where components of the E-field lie both in and out of the plane of the surface. It is reasonable to expect then that the overall field at the surface is greater for the case of s-polarised light. Nonlinearity measurements showed that a multiphoton excitation process could be used to explain the observed photoelectron energies for p-polarised light but not for the s-polarised light. A speculative suggestion is that the extra field enhancement in the s-polarised case pushes the system into the tunnelling regime whereby a multi-photon picture fails to fully explain the photoelectrons observed.

3.6 Summary and Discussion

Time of flight photoelectron spectroscopy experimental measurements have shown that few-cycle laser pulses with a photon energy of 1.55 eV can be used to generate photoelectrons with kinetic energies of up to 80 eV at a HOPG surface. The excitation process was found to exhibit a significantly higher order non-linearity (up to 22nd order) as compared to previous reports of high energy photoelectrons generated by similar wavelengths at other surfaces [22].

Comparison of the IR photoelectron spectrum with that generated at the same surface using XUV photons revealed striking similarities suggesting that the non-linear excitation in the IR case could access the same final states as a straightforward one-photon excitation using XUV light. This has demonstrated for the first time that band structure effects can survive into such a non-linear regime.

Experimental evidence has suggested that a multiphoton excitation mechanism can be used to describe the generation of these high energy photoelectrons, particularly for the case of p-polarised light. Possible transitions at the M-point and Γ point have been identified for the measurements made with p-polarised light. These transitions lie within or just outside of the uncertainty of experimental measurements respectively. At the laser intensities used however, and with some evidence of field enhancement at the surface, excitation due to a tunnelling mechanism can not be completely ruled out, especially for the case of s-polarised light for which nonlinearity measurements taken do not match up fully with observed kinetic energies.

The use of few-cycle laser pulses as a source of femtosecond electron pulses [56] is an area of growing interest and importance where clear uses of such electron pulses include time resolved electron diffraction experiments [57]. A recent review of non-linear photoemission by Ferrini et al. describes various mechanisms by

which photoelectrons with high kinetic energies may be created however there are no previous reports in the literature of photoelectrons generated by such a high-order process or of apparent signatures of such excited states in the band structure (it has previously been shown that multiphoton transitions of 2nd-4th order can excite unoccupied states just above the vacuum level at the Cu(001) surface [123]). Ferrini et al. also highlighted the lack of detailed theory currently available to describe such laser-matter interactions.

Time-resolved photoemission experiments at the HOPG surface have been undertaken to provide further understanding of the excitation process leading to these high energy photoelectrons and the timescales involved. These experiments are presented in the next chapter.

Chapter 4

Interferometric Measurements and Optical Bloch Simulations of Photoelectron Emission from the HOPG surface

4.1 Introduction

This chapter concentrates on the application of interferometric techniques to further investigate the photoelectron emission generated at the HOPG surface by few cycle infra red laser pulses as described in the previous chapter. The background theory of interferometric and pump-probe experiments has been described in Chapter 2 along with the theory behind few cycle laser pulses which allow for increased temporal resolution.

The first of two experiments presented in this chapter is the Interferometric Auto-correlation (IAC) of the photoelectron emission from the surface. This is achieved using two equal IR pulses separated in time by a delay τ and the shape of the

resulting interferogram is used to provide information on the nonlinearity of the excitation process as well as the coherence. The experimental method is described and the results presented with some qualitative analysis. Particular attention is paid to the photoelectrons generated with extremely high kinetic energies of >20 eV. Throughout this chapter the experimental set up used is that as previously described in Chapter 3 but with the laser output from laser table directed through one of two interferometers placed after laser table before the entrance to the vacuum beam-line.

The second experiment presented in this chapter is an IR pump-XUV probe measurement at the HOPG surface. In principle such an experiment can be used to make time-resolved measurements at the surface on an attosecond timescale. In reality the challenging experimental conditions and limited beam time available meant that attosecond resolved measurements could not be achieved however the IR-XUV pump-probe method was tested on the HOPG surface where the IR pump was used to excite low lying conduction band states below the vacuum level. The experimental techniques used are described including experimental obstacles that were successfully overcome. The IR pump - XUV probe measurements made at the HOPG surface are presented and discussed.

Finally, the Optical Bloch Equations (OBE's) have been used to construct a simulation of the experimental measurements to aid interpretation of the results. Standard OBE's have been modified and solved numerically to allow the simulation of high order multiphoton transitions thought to lead to photoelectrons observed at the HOPG surface with kinetic energies >20 eV. The OBE's are explained and a brief summary of previous literature given. The numerical method used to solve the equations is discussed along with the effect of various parameters such as damping terms, detuning and pulse area. Particular attention is paid to the adaptation of the equations to include nonlinearity and how this effects measurements. Lastly, the application of the OBE's to the experimental measurements

described above are presented and the fit between the data and simulation are discussed.

4.2 Interferometric Autocorrelation Measurements of the Photoemission Signal Generated by 13fs IR Pulses

4.2.1 Experimental Method: Interferometric Autocorrelation Measurements using 13fs IR Pulses

Interference autocorrelation measurements of the photoelectron emission from the surface were made using a Michelson Interferometer built by Dr. Eva Heesel from UCL (University College London). 13fs infra red pulses from the hollow fibre output (as described in Chapter 3) were split into two pulses of equal intensity using an ultrathin ($612 \pm 5\text{nm}$) 50:50 beamsplitter. A schematic diagram of the interferometer is shown in Figure 4.1 where it can be seen that the two beam paths are created from the beamsplitter to mirror M3 (stationary arm) and the beamsplitter to M4 (variable arm). The relative delay between the two pulses could be changed by altering the position of mirror M4 thereby increasing/decreasing the path length of the variable arm. Both arms were recombined at the beamsplitter such that the spatially overlapped pulses followed a collinear path into the HHG chamber.

Coarse movement of mirror M4 was provided by a motorised linear translation stage (Physik Instrumente) with a maximum range of 100 mm (corresponding to a relative delay between the pulses of 667 ps) and a minimum step size of $1 \mu\text{m}$ (6.67 fs). Fine movement was achieved using a piezoelectric transducer stage (also

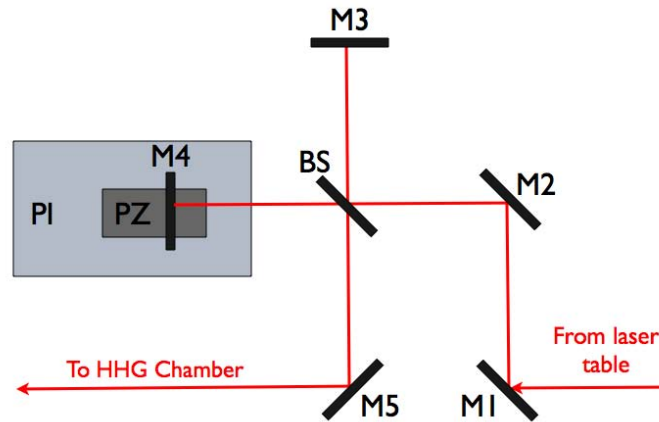


FIGURE 4.1: Schematic diagram of the Interferometer used for autocorrelation measurements of the photoelectron signal. The incident laser pulse from the laser table is split into two identical pulses at the beam splitter (BS). One pulse follows the stationary arm of the interferometer (M3), the other follows the variable arm of the interferometer (M4). The relative delay between the pulses is achieved by altering the path length between the beam splitter and mirror M4 travelled by pulses in the variable arm. The linear translation stage (PI) provides coarse movements and finer steps can be made using a piezoelectric transducer stage (PZ).

from Physik Instrumente) which had a maximum range of motion of $38 \mu\text{m}$ and a minimum step size of 1nm (6.67 attoseconds). LabView programs were used to control the positions of the two stages during experiments.

The absolute position of the stages at which the two pulses were temporally overlapped was found to vary from day to day because the optimisation of the output from the laser table affected the beam pointing. A HeNe (Helium Neon) laser that followed the same path as the laser was used for initial alignment purposes, however it was necessary to determine the exact position of zero delay using the IR pulses before the experiment. This was achieved by performing a linear autocorrelation firstly on a coarse scale by setting the piezo stage at its mid point and scanning the linear stage whilst recording the laser power using a Thorlabs digital optical power meter. The power meter output could be recorded using a Labview program. Once the linear position at which power reading was maximum had been located, the linear stage could be set to this value and then the process repeated on

a finer scale by scanning the piezo stage to determine the most accurate position measurement of the zero delay point.

Once an accurate position for the temporal overlap had been determined the piezo was sent to either the most positive/negative delay of interest. A ToF photoelectron spectrum was taken at the desired delay and then the stage stepped in the required negative/positive direction. Ensuring that steps were always taken in a single direction prevented any error caused by hysteresis of the piezo stage.

The primary purpose of the interference autocorrelation (IAC) measurements of the photoemission signal from the HOPG surface was to provide further understanding of the excitation process leading to the generation of high kinetic energy electrons as described in Chapter 3. As such, the laser intensity used for the IAC experiments was chosen such that each pulse separately was below the threshold intensity required to observe the ‘fast’ (>20 eV) electrons but so that the constructive interference between the two pulses lay above the threshold.

4.2.2 Results: Interferometric Autocorrelation Measurements using 13fs IR Pulses

Photoelectron spectra were taken at various pump-probe delays starting from -15 fs up to +15 fs with step sizes of 0.3 fs from -2 fs to +2 fs and 0.5 fs steps elsewhere. These step sizes were chosen to maximise resolution whilst minimising the actual lab time taken to perform the experiment as laser drift presented a problem allowing approximately 1 hour experimental time before re-alignment was necessary. The photoelectron spectra taken at each delay have been put together in Figure 4.2 and Figure 4.3 to show the photoemission as a function of pump-probe delay.

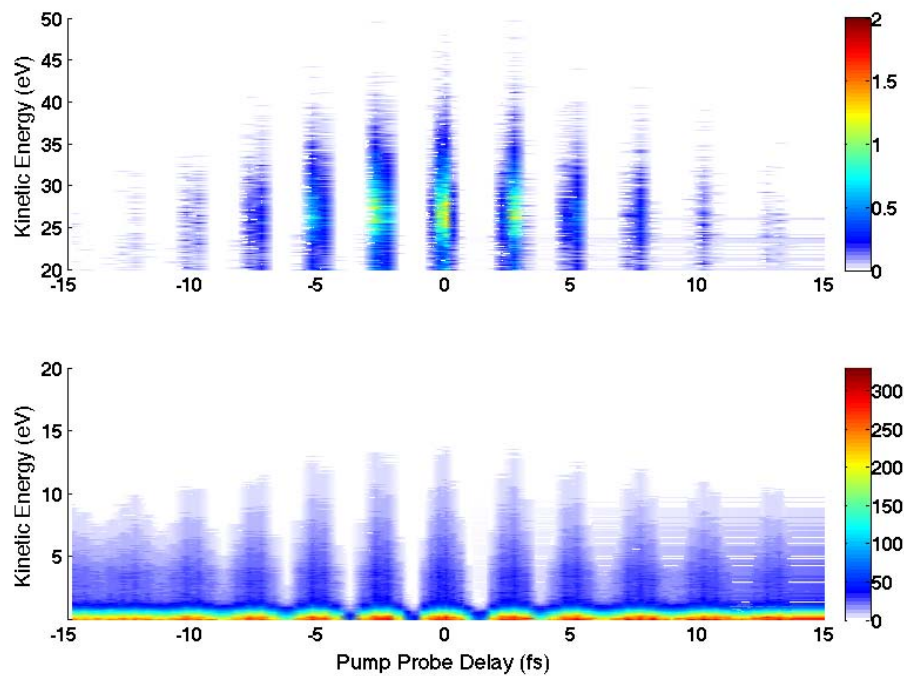


FIGURE 4.2: Photoelectron emission interference autocorrelation for p-polarised Light: A 2D colour plot of the photoelectron emission from the HOPG surface as a function of pump-probe delay of two equal 13 fs p-polarised laser pulses. Photoelectron kinetic energies of (upper panel) 20 eV-50 eV (lower panel) 0 eV-20 eV are shown separately and colour displays the photoelectron yield as given in the colorbar (arb. units) The fringes shown correspond to temporal interference and have a periodicity equal to the laser cycle of 2.67 fs.

Figure 4.2 shows the 2D colour plot of the photoelectron emission interference autocorrelation for p-polarised light. Three separate bands of photoelectron energies can be resolved which correspond to the three features of the photoelectron spectrum as described in Chapter 3 with peak kinetic energies of 0.3 eV, 3.5 eV, and 26-28 eV. The different behaviour of these three bands can be seen as a function of the delay time between the two pulses. The colour scale gives the number of electrons collected and the highest energy electrons observed (>20 eV) are shown on a different scale in the upper plot. Figure 4.3 gives the same information for the case of s-polarised light.

Immediately visible across all kinetic energies are the interference fringes (running vertically along the 2D figure). These correspond to constructive and destructive

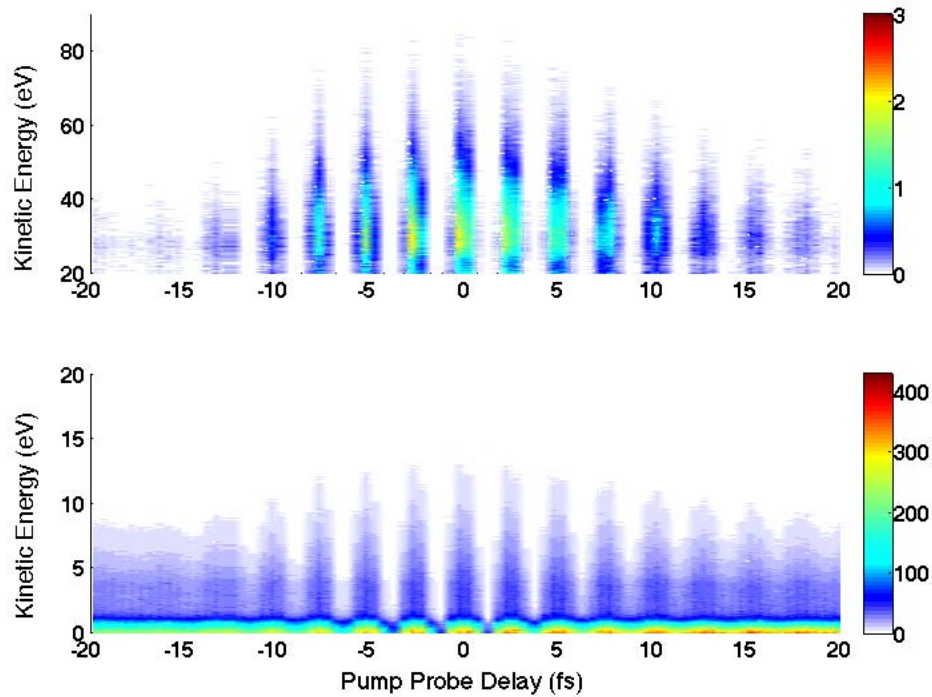


FIGURE 4.3: Photoelectron emission interference autocorrelation for p-polarised Light: A 2D colour plot of the photoelectron emission from the HOPG surface as a function of pump-probe delay of two equal 13 fs p-polarised laser pulses. Photoelectron kinetic energies of (upper panel) 20 eV-90 eV (lower panel) 0 eV-20 eV are shown separately where the x-axis gives the time delay between the pump and probe pulses, the y axis gives the kinetic energies of the photoelectrons measures and colour displays the photoelectron yield as given in the colorbar (arb. units). As in Figure 4.2 the fringes observed correspond to interference of the two pulses in time and have a periodicity equal to the laser cycle of 2.67 fs.

temporal interference between the two pulses and result from the collinear nature of the two pulse outputs from the Michelson interferometer thereby confirming the coherent nature of the excitation process. The periodicity of the fringes was measured as 2.67 fs, the time taken for one complete laser cycle. The shape of these fringes can also be seen in Figure 4.4 and Figure 4.5 where the photoelectron signal has been integrated over kinetic energy ranges of 0-1.2 eV, 1.2-20 eV and 20 eV-45 eV/90 eV for p/s polarised light. This allows the shape of the autocorrelation envelope to be viewed more clearly for each individual band of electrons from the original spectra.

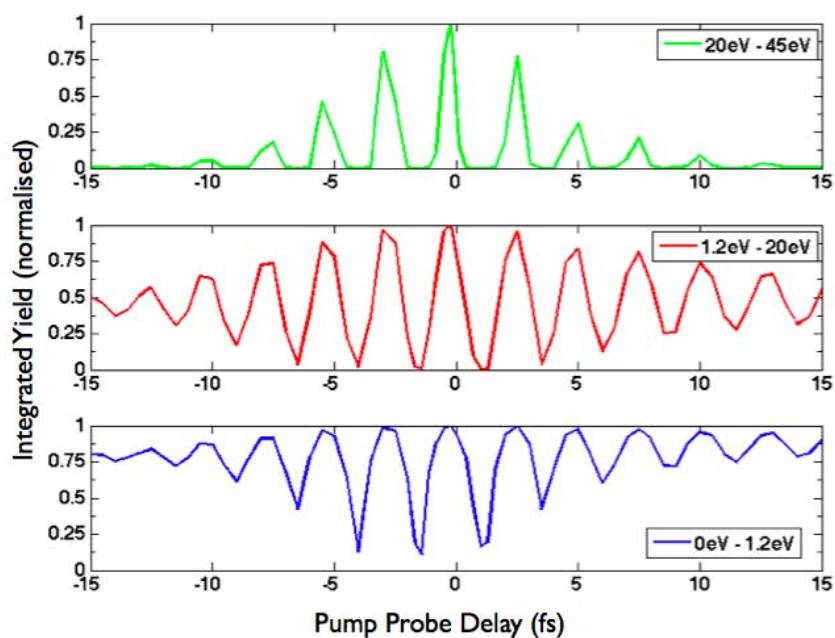


FIGURE 4.4: Interferometric autocorrelation shapes for p-polarised pulses: The autocorrelation signal as shown in Figure 4.2 has been integrated over each of the three photoelectron features and is plotted as a function of pump-probe delay.

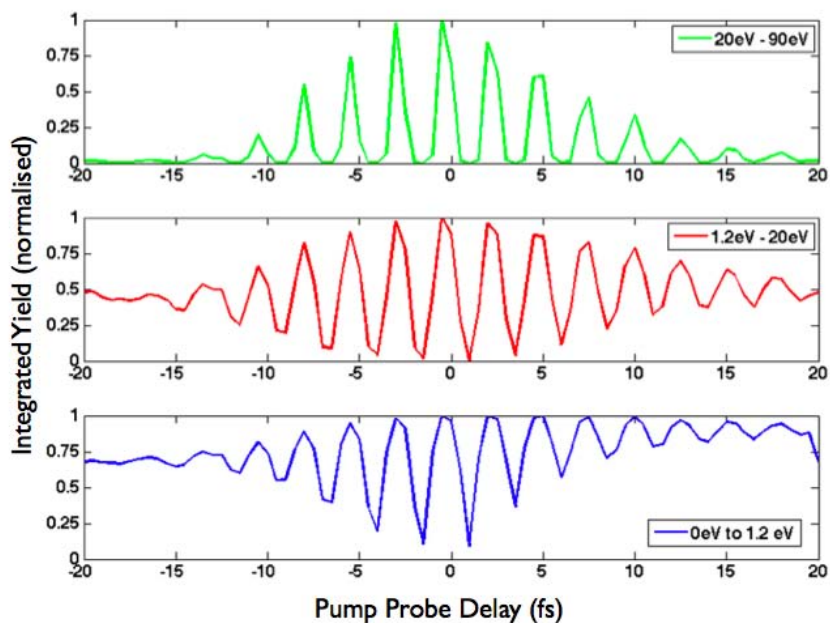


FIGURE 4.5: Interferometric autocorrelation shapes for s-polarised pulses: The autocorrelation signal as shown in Fig. 4.3 has been integrated over each of the three photoelectron features and is plotted as a function of pump-probe delay. Asymmetry in the autocorrelation shape about zero delay is thought to be due to laser drift.

For the electrons with lowest kinetic energy (peak ~ 0.3 eV) the interference fringes show saturation and a lifetime of the process extending far beyond the range of delays used.

The mid-energy photoelectron feature (corresponding to electrons with a peak kinetic energy of ~ 3.5 eV) can also be seen to extend to longer delay times with interference fringes observed across the whole delay range. In this case however the interference fringes can be seen more clearly than for the lower energy photoelectrons. A narrowing of the linewidth of the individual fringes is also observed with increasing photoelectron kinetic energy.

The shape of the autocorrelation traces can be seen more clearly in Figure 4.4 and Figure 4.5 where the total photoelectron signal has been averaged over each electron feature and plotted as a function of pump-probe delay. The mid-energy peak (integrated over kinetic energies from 1.2 eV - 20 eV) appears to show a typical 1st-order envelope shape with the base line at 0.5 on the normalised scale [14]. In contrast, for a 2nd order interferometric autocorrelation the contrast ratio of 8:1 i.e. the base line would start at ~ 0.2 on a normalised scale. With increasing electron kinetic energy, the mid-energy autocorrelation envelope shape becomes more and more nonlinear in behaviour until the envelope appears similar to that for electrons in the highest kinetic energy range of >20 eV. These highest energy photoelectrons, which are of most interest can be seen (Figure 4.2 upper and Figure 4.3 upper) to produce extremely sharp interference fringes with an individual linewidth shorter than one optical cycle. Figure 4.4 and Figure 4.5 show how the electron counts between the fringes is zero at delays corresponding to destructive interference. The FWHM of the autocorrelation envelope is measured as 9.5 fs for p-polarised light and 14 fs for s-polarised light. For a standard autocorrelation measurement the ratio $\Delta\tau = 1.54\Delta t$ is usually used as a rule of thumb to convert from delay time $\Delta\tau$ to time Δt this takes into account the intensity FWHM of the pulse itself. The factor 1.54 corresponds to a *sech*² pulse fit and a Gaussian fit

has a scale factor of 1.414 which will give a slightly higher estimate if converting data from $\Delta\tau$ to Δt . For the case of this experiment, the pulse intensity FWHM measured by FROG trace was 13 fs so an experimental FWHM (in delay time τ) would be expected to be 18.4 (*sech*² fit) or 20.02 (Gaussian fit). This is the case for the mid-energy photoelectrons shown in red in Figure 4.4 and Figure 4.5. For the ‘fast electrons’ however the FWHM of the autocorrelation envelope is found to be significantly less at 9.2 fs for p-polarised light and 14 fs for s-polarised light.

The shape of the autocorrelation trace for the low energy electrons (0 eV - 1.2 eV) shown in Figure 4.4 and Figure 4.5 is also somewhat unexpected with an asymmetry about the baseline, leading to the baseline being located at a value of 0.75 on a normalised scale.

The Optical Bloch Equations (OBE) have been used to model this autocorrelation trace to provide more information on these measurements, concentrating particularly on the case of the high energy electrons. This theoretical treatment is described in the later parts of this chapter.

4.3 IR/XUV Pump Probe Measurements

4.3.1 Experimental Method: IR-XUV Pump Probe Measurements

The final and most complicated measurements made using few-cycle pulses at the HOPG surface were those using a combination of few-cycle IR pulses and XUV pulse trains to perform IR pump/XUV probe experiments. The vacuum beamline used has been described previously (Figure 3.8). In order to generate the pump and probe pulses an annular Michelson interferometer, constructed by Imperial College was placed before the beamline.

The interferometer generated two coherent beam paths with a variable relative temporal delay of up to 250 fs. Custom made mirrors (M1 and M4 Figure 4.6) had 2 mm diameter holes drilled through them at a 45 degree angle. M1 was used to separate the 7 fs IR fundamental pulses into two different paths, an outer beam with a ring shaped spot profile and an inner beam corresponding to the missing hole inside of the ring. The inner beam travelled over a variable path length controlled by the movement of mirrors M6 and M7, positioned on a piezo stage. The inner beam was also the strongest of the two beams by a power ratio of 5:1 chosen so that it was powerful enough to be used to generate an XUV pulse train for the pump beam. The annular (ring shaped) beam formed the IR probe beam. After being recombined by the second ring shape mirror M4 both beams were focused onto an argon gas jet in the HHG chamber to generate XUV pulse trains by an off-axis parabolic mirror (see page 55 for an explanation of the HHG method). After the gas jet both pulses passed through a homebuilt split filter consisting of an inner 200nm aluminium filter mounted on an annular plate. The purpose of this glass ring was to filter out any XUV generated by the outer beam while the Al filter transmitted the XUV pulse trains whilst blocking the inner IR beam. The net result was an IR outer ring-shaped beam and an XUV inner beam. The two were focussed onto the surface by the gold toroidal mirror which focusses to the same point irrespective of wavelength.

A key part of the experimental design was the split filter and separate glass plate of equal thickness. These were not present initially and the annular interferometer operated in a slightly different configuration. A major drawback to the initial set-up, only discovered once experiments started, was that the two IR beams interfered temporally in the gas jet. The resulting interference fringes (in time) resulted in a harmonic yield that varied periodically as a function of pump-probe delay. As the photoelectron signal in turn depended on the intensity of the incident light it was found that any pump-probe photoelectron measurements were dominated by the

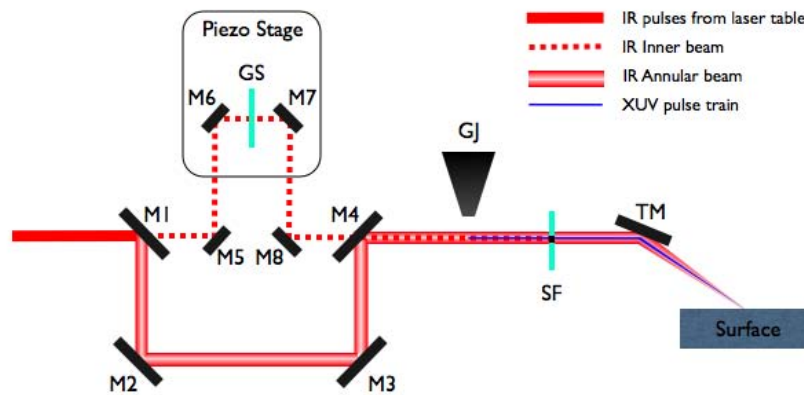


FIGURE 4.6: Schematic diagram of the XUV-IR pump probe experiments: Mirror M1 separated the IR fundamental into an outer ring shaped IR beam and inner IR beam. The inner beam could be delayed with respect to the outer beam using a piezo stage. Both beams were then focussed into the gas jet where XUV pulse trains were generated by HHG. A home-made split filter (SF) had an aluminium filter centre which passed XUV but blocked IR light and an ultrathin glass outer ring which blocked XUV and transmitted IR. A glass slide (GS) ensured both pulses travelled through an equal thickness of glass. The inner XUV pulse and outer IR pulse were focussed to the same spot on the surface by the gold toroidal mirror (TM).

temporal interference fringes. The purpose of the initial glass plate (GS in Figure 4.6) was to delay the inner IR pulse by a substantial amount before the gas jet so that the two pulses no longer interfered in time. The outer IR pulse could then be delayed by an equal amount after the gas jet by the doughnut shaped piece of glass of equal thickness which made up the outer part of the split filter (SF).

In such a complicated beamline set-up laser drift was a large problem, affecting the hollow fibre output, harmonic generation and general alignment. The alignment of the experiment from start to finish (i.e. from the laser cavity to the surface including finding the temporal overlap of pump and probe pulses) was a lengthy process taking an average of 5-8 hours. Re-optimisation after significant beam drift could take from 10 mins to 1 hour. In an attempt to reduce experimental time and therefore maximise the work that could be done within a finite allocated beamtime the collection of data was fully automated. This was done using a

LabView8 program written by Justin Steele-Davies from Reading University. The program could interface with the FastCom card on one PC to collect ToF data whilst also having an interface with the piezo stage controlled by another PC. After each ToF spectrum had been recorded the piezo stage was quickly moved to its new position corresponding to the next pump-probe delay so that the next ToF scan could take place. The ToF results could be viewed throughout the process and parts of the spectrum of interest could be monitored as a function of delay so that bad data sets could be terminated early reducing wasted time. The automated system was successful in reducing the effect of laser drift as much as possible. The beam pointing was still a significant problem though and in the long term, for future experiments at Imperial College a corrective feedback system has been planned. For all IR/XUV experiments, the pulse duration of the Infra red pulse was 7fs. The duration of the XUV pulses could not be measured although the characterisation of the XUV pulses formed the main aim of the team from Oxford University who were involved in the Attosecond collaboration.

4.3.2 Results and Discussion: IR-XUV Pump-Probe Measurements

Initially the intensities of the XUV and IR light were chosen such that the photoelectron signal created by each one individually was roughly equal. Using these parameters the pump-probe scans recorded no changes whatsoever as a function of pump-probe delay time. It is thought that this was simply due to low cross sections.

The XUV signal could be further maximised at the expense of the IR intensity. The photoelectron spectra recorded at these intensities are shown in Figure 4.7. Although the IR pulse itself did not generate significant yield of photoelectrons the pump-probe scan was successful in that a change in yield could be seen around the

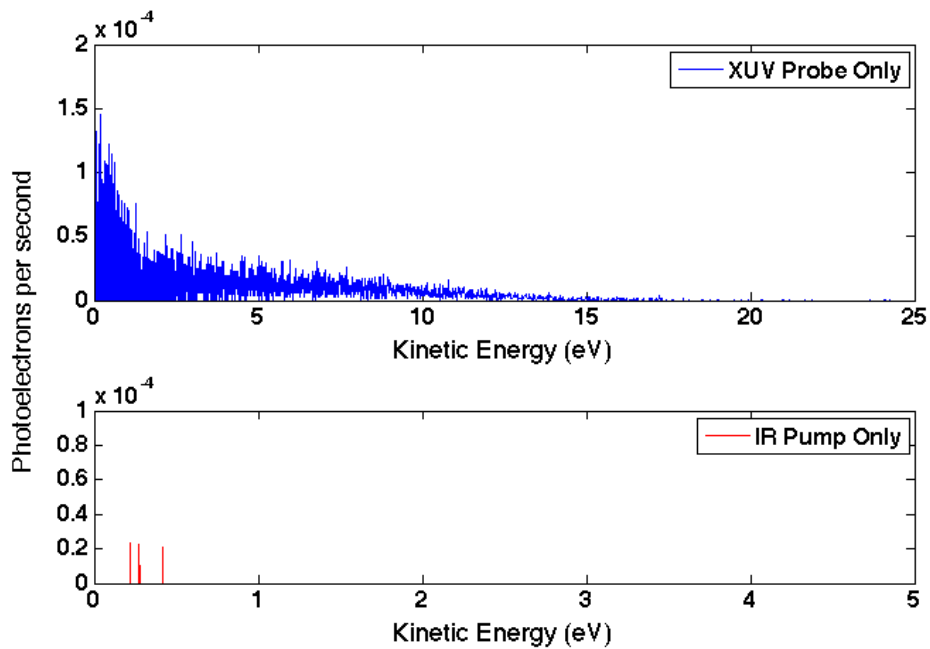


FIGURE 4.7: Photoelectron measurements taken before pump probe experiments to show the individual contribution from the IR pump (lower panel) and XUV probe (upper panel). In this case the XUV signal was maximised resulting in an extremely low yield from the IR pump alone.

zero delay position. It should be noted that using these experimental parameters, dictated by the inherent design of the laser beamline the IR-XUV pump-probe measurements could not be used to probe the strong field effects leading to high energy photoelectrons reported in Chapter 3. It was not possible to measure the IR laser intensity during the experiment however it was substantially below 4.7×10^{10} W/cm².

For the case where the XUV light alone was incident on the HOPG surface (Figure 4.7 upper plot), the photoelectron spectra was the same as that described in more detail in Chapter 3 however due to the short collection times required for the pump probe experiment the feature above kinetic energies of 20 eV could not be resolved. During pump-probe measurements the combined IR and XUV photoelectron spectra taken at different delay values was also very similar and

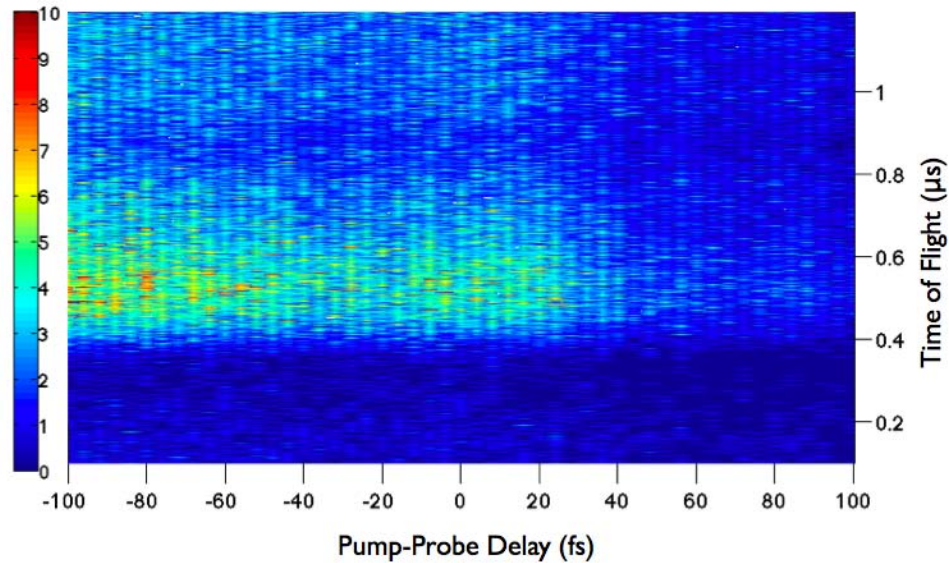


FIGURE 4.8: IR-XUV Pump-Probe Raw Data: Shown on a time of flight scale vs. delay where negative delay values correspond to the XUV pulse arriving first and positive delay values correspond to the IR pulse arriving at the surface first.

could not be distinguished from the XUV only spectrum.

The raw data for the IR-XUV pump-probe measurement is shown in Figure 4.8. It has been displayed on a time of flight scale in μs rather than on the converted kinetic energy scale as the regions of interest can be distinguished more easily. The horizontal band seen in Figure 4.8 from $\sim 0.4 \mu\text{s}$ to $\sim 0.9 \mu\text{s}$ corresponds to photoelectrons with kinetic energies of 2 eV - 20 eV and the band seen at $\sim 1 \mu\text{s}$ corresponds to those photoelectrons with less than 2 eV kinetic energy. There was a significant laser drift throughout the experiment hence the overall laser intensity at negative delays (left hand side) was much higher than that at positive delays. The bright feature seen stretching from delays of -20 fs to +20 fs is the measurement of interest. It can be seen more clearly in Figure 4.9.

Figure 4.9 (a) shows the total photoelectron signal integrated over all photoelectron kinetic energies as a function of pump-probe delay. In Figure 4.9 (b) and (c) the integrated yield has been taken over the two separate features of the PES, from 2 eV - 20 eV and 0 eV - 2 eV respectively. The background slope due to laser drift

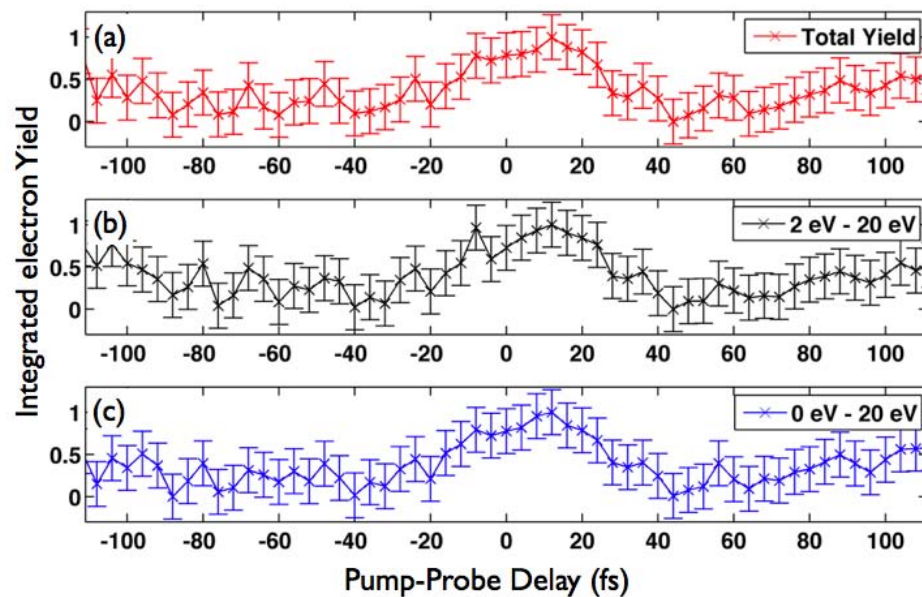


FIGURE 4.9: Photoelectron Yield vs. Pump-Probe Delay: The photoelectron yield shown corresponds to the normalised integration of the signal (a) over all electron kinetic energies (no upper limit), (b) for photoelectrons with energies of 2 eV - 20 eV, (c) for photoelectrons with energies from 0 eV - 2 eV. Error bars show the uncertainty of the points which results from the subtraction of a linear background slope as explained in the text.

during the experiment has been assumed to be linear and a linear fit of the slope has been subtracted from the data. The difference in the number of photoelectrons before and after the scan were consistent with the observed drop in laser intensity over the same interval i.e measured before and after the experiment. Error bars shown in Figure 4.9 show the standard deviation of the difference between the value of the signal and the linear estimate of the background slope attributed to laser drift. The “delay zero” point was determined from the maximum of a IR-IR pump-probe interference trace performed immediately prior to the scan. The ultrathin pieces of glass had to be removed to perform the IR-IR test scan. Taking the accuracy of the measurement of thickness to be $0.5 \mu\text{m}$, this corresponds to a temporal uncertainty of 1.67 femtoseconds.

From the data taken it can be clearly seen that whilst the IR pulse alone does not generate a significant photoelectron signal, its presence as a pump pulse before the

XUV probe signal leads to an increase in photoelectron signal around delay zero. There is little difference between the integrated yield taken from different parts of the photoelectron spectrum (i.e. between Figures 4.9 (a) and (b)) showing that the generation of all electrons is enhanced by the same extent by the presence of the IR pump. Oscillations in the integrated signal are observed however these lie within the range in uncertainty of the measurements.

It is possible for the IR pulse to excite low lying conduction band states located below the vacuum level [32] that could not be probed the IR pulse alone. If the cross section for excitation by the XUV pulse is greater from such a surface state as compared to the initially occupied valence band states then the overall photoelectron yield would increase as observed. Further discussion of the data is made in the following section as a result of comparisons with the Optical Bloch Equations.

4.4 The Optical Bloch Equations

4.4.1 Background

The Optical Bloch Equations (OBE) are commonly used as a tool to model the interaction between a two level system (ground state and excited state) and a laser field as a function of time [26, 28, 31, 81, 124, 125]. In this thesis Optical Bloch Equations have been used to model interferometric measurements at the HOPG surface, concentrating particularly on the IAC measurements using 13 fs IR pulses.

The time dependence of an excited state can, to a simple extent, be described using the Schrödinger equation where excitation and stimulated emission can be taken into account. For a fully accurate description of a system however, the inclusion of relaxation terms (spontaneous emission) are also required. Such spontaneous

emission will result in the population of a statistical distribution of light field states and will therefore leave an atom in a distribution of momentum states [126]. For this reason, rather than the single wavefunction used to describe the system as with the Schrödinger equation, it is necessary to describe the system as a distribution of wavefunctions. To calculate the probability that an atomic system exists in a certain statistical distribution of states a density operator must be used to characterise the statistical mixture of quantum states. The Optical Bloch Equations describe the evolution of the matrix elements of this density operator over time. It should be emphasised that the OBE's describe a simple atomic picture of two levels; the effect of band structure or band width are not taken into account.

Previous examples in the literature have shown that the Optical Bloch Equations may be used to extract extra information from time resolved photoemission experiments. Hertel et al. showed that OBE's could be used to extract the lifetimes of excited states on the Cu(111) surface from experimental 2- colour pump-probe data despite the fact that the surface state lifetimes in question were shorter than the pulse duration used. Some of their data are shown in Figure 4.10 (a) and (b). This method of OBE analysis may only be used if the actual zero delay point is known precisely (i.e. the peak of the temporal profile of the pump pulse) as it relies on the measurement of a shift in the photoemission peak with respect to the temporal profile of the pulse [31]. For resonant transitions ($\omega_{transition} = \omega_{laser}$) the population of the excited state will lag behind the temporal profile of the pulse. Since the photoemission observed experimentally corresponds, in the case of Hertel et al. to the population of the intermediate state $|2\rangle$ the shift observed experimentally can be compared to models constructed using OBE's of a two level system and the lifetime of the state extracted from the model. In Figure 4.10(b) the OBE pump-probe results are shown on a normalised scale where the dotted line is the time profile of the pulse which is followed exactly by the population

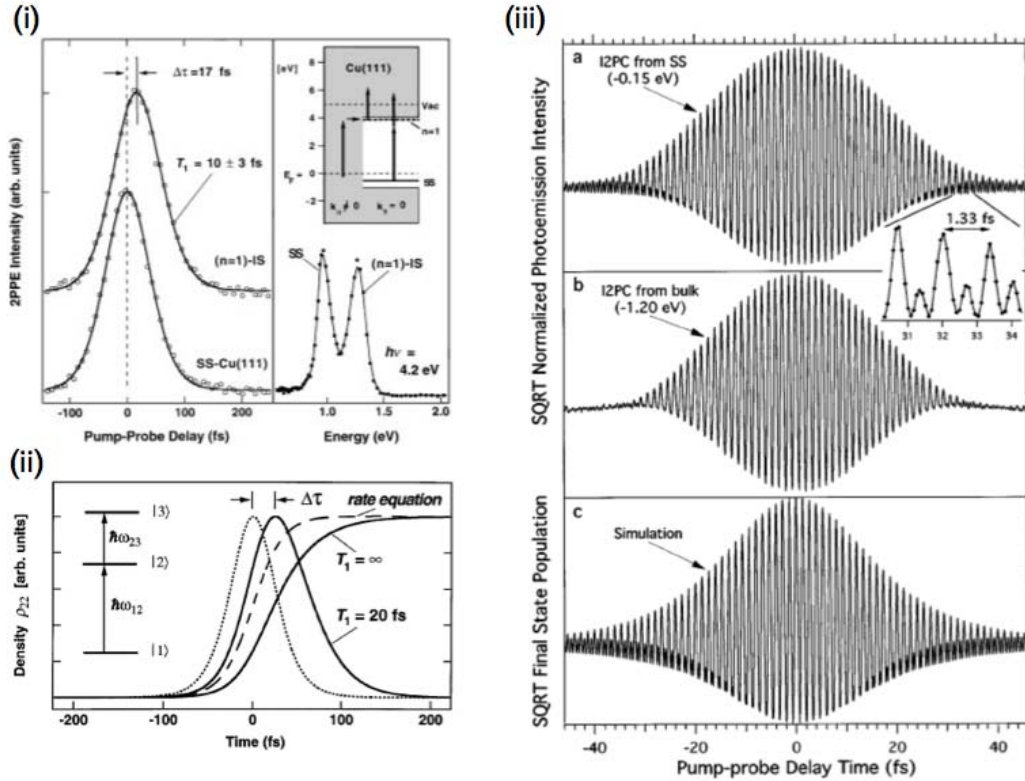


FIGURE 4.10: Examples of OBE simulations from the literature: (i) Experimental data for pump-probe 2PPE measurements of the Cu(111) surface using 4.2 eV pump and 2.1 eV probe. Schematic diagram of the excitation and the 2PPE spectra are shown in the right panel and pump-probe measurements in the left panel (ii) OBE simulations corresponding to (i) where the model ignores the second photon creating a 2 level model of the ground state $|1\rangle$ and intermediate states $|2\rangle$ ((i) and (ii) taken from [31]) More details are given in the main text. (iii) Interferometric autocorrelation measurements of the surface state (upper) and bulk (middle panel) at the Cu(111) surface and an OBE simulation of the IAC from the surface state, taken from [34].

of the excited state for a non-resonant excitation and the solid black curves show the population of the excited state for a resonant excitation with two separate damping conditions. The time integrated pulse envelope is shown by the dashed line and can be compared with the resonant transition for $T = \infty$ to show the inaccuracy incurred using the simple rate equation (Fermi's Golden Rule) to model the situation.

Investigating the same copper surface, Ogawa et al. demonstrated for the first time that interferometric photoemission experiments from a surface could be modelled

successfully using the Optical Bloch Equations. The experimental data and a simulation corresponding to the IAC measurements from the surface state (SS) are shown in Figure 4.10 (c) (top figure and bottom figure respectively). Oscillations observed experimentally at long delays with a periodicity corresponding to the second harmonic were also observed in the OBE model and their origin attributed to the nonlinear polarisation oscillations which can give rise to second harmonic generation at surfaces.

More recently Georges et al. have presented a 4 level (a three photon transition) model of interferometric autocorrelation photoemission measurements where comparisons are made between resonant and non-resonant excitations at a gold surface [127]. They improved upon previous OBE models ([28, 31, 81, 124, 125]) by including multiphoton transition matrix elements between the 4 levels to fully describe the non-resonant continuum-continuum transitions. Whilst the output of this approach compares more favourably to experimental data for non-resonant transitions it is significantly more complex mathematically and as such is beyond the scope of this thesis. It should however be noted that the IAC measurements at the HOPG surface presented in this thesis are much more consistent in shape to the resonant transition models used as a comparison by Georges et al. and so are more likely to correspond to resonant transitions in which case the model described below is accurate.

4.4.2 Standard Optical Bloch Equations for a Two Level System

Starting with a time dependent wavefunction $\Psi(r, t)$ and the Hamiltonian $\hat{\mathcal{H}}$ the Optical Bloch Equations can be derived to give a general explanation of the laser-atom interaction[128]. It is assumed that the incident laser light is monochromatic with a frequency of ω .

The wavefunction describes an atom which can exist either in the ground state ψ_1 or the excited state ψ_2 .

$$\Psi(r, t) = C_1(t)\Psi_1(r, t) + C_2(t)\Psi_2(r, t) \quad (4.1)$$

The total Hamiltonian $\hat{\mathcal{H}}$ is given by:

$$\hat{\mathcal{H}} = \hat{\mathcal{H}}_E + \hat{\mathcal{H}}_I \quad (4.2)$$

The inclusion of the interaction Hamiltonian $\hat{\mathcal{H}}_I$ in addition to the standard atomic Hamiltonian $\hat{\mathcal{H}}_E$ (as used in the time-dependent Schrödinger Equation) allows the interaction of the electric and magnetic fields of the laser radiation with the atom to be described in position and time. Since the most important contribution to $\hat{\mathcal{H}}_I$ comes from the electric dipole moment ($-e\mathbf{D}$) in the electric field ($E_0 \cos \omega t$) the interaction Hamiltonian can be given by:

$$\hat{\mathcal{H}}_I = eD.E_0 \cos \omega t \quad (4.3)$$

By applying the total Hamiltonian (4.2) to the time-dependent wavefunction (4.1) it can be shown [128] that the equations for the coefficients C_1 and C_2 can be given by:

$$\frac{d^2 C_1}{dt^2} = -i\mathcal{V} \cos \omega t \exp(-i\omega_0 t) C_2 \quad (4.4)$$

$$\frac{d^2 C_2}{dt^2} = -i\mathcal{V}^* \cos \omega t \exp(i\omega_0 t) C_1 \quad (4.5)$$

Where \mathcal{V} includes the matrix element X_{12} and the electric field E_0 . The matrix element X_{12} includes the transition dipole moment.

$$\mathcal{V} = \frac{eE_0X_{12}}{\hbar} \quad (4.6)$$

To continue with derivations of the laser-atom interaction it is convenient to define a density matrix $\rho(t)$

$$\rho(t) = \begin{pmatrix} \rho_{ii} & \rho_{ij} \\ \rho_{ji} & \rho_{jj} \end{pmatrix} \quad (4.7)$$

Where the individual elements of the matrix are given by:

$$\begin{aligned} \rho_{11} &= |C_1|^2 \\ \rho_{22} &= |C_2|^2 \\ \rho_{12} &= C_1C_2^* \\ \rho_{21} &= C_2C_1^* \end{aligned} \quad (4.8)$$

The diagonal terms in the density matrix are known as the population terms and are related to the average population of the ground or excited state where Equation 4.9 is always true.

$$\rho_{11} + \rho_{22} = 1 \quad (4.9)$$

The off-diagonal terms are complex and satisfy the relationship

$$\rho_{12} = \rho_{21}^* \quad (4.10)$$

Differentiating the off-diagonal terms in (4.8) shows that the equations of motion for the density matrix can be taken simply by using the equations of motion for the coefficients:

$$\frac{d\rho_{12}}{dt} = C_1 \left(\frac{dC_2^*}{dt} \right) + C_2^* \left(\frac{dC_1}{dt} \right) \quad (4.11)$$

Substituting (4.4) and (4.5) into (4.8) gives:

$$\frac{d\rho_{22}}{dt} = -\frac{d\rho_{11}}{dt} = -i \cos \omega t (\mathcal{V}^* \exp(i\omega_0 t) \rho_{12} - \mathcal{V} \exp(-i\omega_0 t) \rho_{21}) \quad (4.12)$$

$$\frac{d\rho_{12}}{dt} = \left(\frac{d\rho_{21}}{dt} \right)^* = i\mathcal{V} \cos \omega t \exp(-i\omega_0 t) (\rho_{11} - \rho_{22}) \quad (4.13)$$

Finally the rotating wave approximation can be made. Assuming that ω (laser frequency) is close in magnitude to ω_0 (transition frequency), it is assumed that terms oscillating at a frequency of $(\omega_0 + \omega)$ have a negligible effect compared to those terms oscillating at $(\omega_0 - \omega)$. By removing these rapidly oscillating terms from (4.12) and (4.13) gives [128]:

$$\frac{d\rho_{22}}{dt} = -\frac{d\rho_{11}}{dt} = -\frac{1}{2}i\mathcal{V}\tilde{\rho}_{12} + \frac{1}{2}i\mathcal{V}\tilde{\rho}_{21} \quad (4.14)$$

$$\frac{d\tilde{\rho}_{12}}{dt} = \left(\frac{d\tilde{\rho}_{21}}{dt} \right)^* = \frac{1}{2}i\mathcal{V}\rho_{11} - \frac{1}{2}i\mathcal{V}\rho_{22} + i(\omega_{12} - \omega_l)\tilde{\rho}_{12} \quad (4.15)$$

Equation 4.14 and Equation 4.15 are the basic Optical Bloch Equations. In this case the substitution $\tilde{\rho}_{12} = \rho_{12} \exp[-i(\omega_{12} - \omega_l)t]$ has been made and the Rabi frequency, \mathcal{V} is given as before. The electric field, $E(t)$ depends on the simulation used i.e. single pulse, pump-probe and also on the pulse shape assumed. The electric field used in these investigations for a single Gaussian pulse was $E(t) = E_0 \exp(-t/t_G)^2$ where $t_G = \frac{t_p}{\sqrt{2 \ln 2}}$, t_p is the FWHM of the pulse. The terms ω_l and

ω_{12} are the laser frequency and the transition frequency respectively (previously defined as ω and ω_0 in the derivation).

4.4.3 A Numerical Solution to the Optical Bloch Equations

For a simple two level system as in (4.14) and (4.15) it is possible to solve the equations using the substitution of trial solutions however a numerical method was chosen instead so that changes such as the inclusion of damping terms or nonlinearity could be made more easily. The four interdependent Optical Bloch Equations can be written in a matrix form as shown in Equation 4.16.

$$\begin{pmatrix} 0 & 0 & i\frac{1}{2}\mathcal{V} & -i\frac{1}{2}\mathcal{V} \\ 0 & 0 & -i\frac{1}{2}\mathcal{V} & i\frac{1}{2}\mathcal{V} \\ i\frac{1}{2}\mathcal{V} & -i\frac{1}{2}\mathcal{V} & i(\omega_0 - \omega) & 0 \\ -i\frac{1}{2}\mathcal{V} & i\frac{1}{2}\mathcal{V} & 0 & -i(\omega_0 - \omega) \end{pmatrix} \begin{pmatrix} \rho_{11} \\ \rho_{22} \\ \tilde{\rho}_{12} \\ \tilde{\rho}_{21} \end{pmatrix} = \begin{pmatrix} \frac{d\rho_{11}}{dt} \\ \frac{d\rho_{22}}{dt} \\ \frac{d\tilde{\rho}_{12}}{dt} \\ \frac{d\tilde{\rho}_{21}}{dt} \end{pmatrix} \quad (4.16)$$

Equation (4.16) can then be rearranged to give (Equation 4.17) with the condition that Δt is a very small change in time.

$$\begin{pmatrix} \Delta\rho_{11} \\ \Delta\rho_{22} \\ \Delta\tilde{\rho}_{12} \\ \Delta\tilde{\rho}_{21} \end{pmatrix} = \Delta t \begin{pmatrix} 0 & 0 & i\frac{1}{2}\mathcal{V} & -i\frac{1}{2}\mathcal{V} \\ 0 & 0 & -i\frac{1}{2}\mathcal{V} & i\frac{1}{2}\mathcal{V} \\ i\frac{1}{2}\mathcal{V} & -i\frac{1}{2}\mathcal{V} & i(\omega_0 - \omega) & 0 \\ -i\frac{1}{2}\mathcal{V} & i\frac{1}{2}\mathcal{V} & 0 & -i(\omega_0 - \omega) \end{pmatrix} \begin{pmatrix} 1 \\ 0 \\ 0 \\ 0 \end{pmatrix} \quad (4.17)$$

A matlab program was written whereby initial conditions could be entered for the population and coherence terms. For a system in its ground state these are $\rho_{11} = 1$, $\rho_{22} = \tilde{\rho}_{12} = \tilde{\rho}_{21} = 0$. The program then calculated the change in

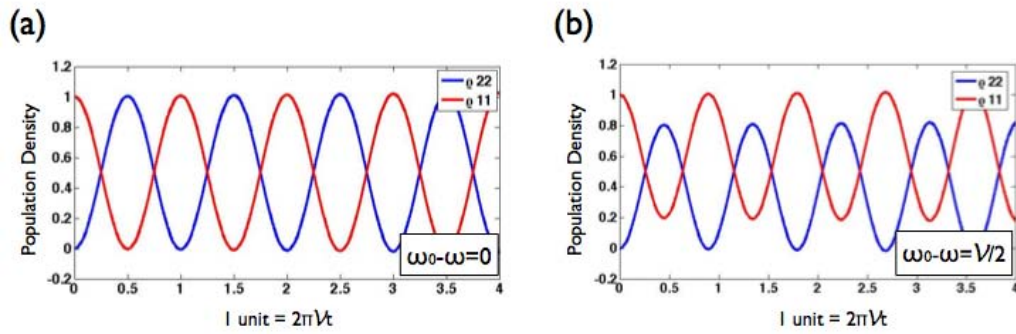


FIGURE 4.11: Rabi oscillations of population density of a two level system: Time is given (x-axis) in units of $2\pi\mathcal{V}$ where \mathcal{V} is the Rabi frequency. Initial conditions are $\rho_{11} = 1, \rho_{22} = 0$ i.e. the lower state is fully populated, upper state is empty.

population density of the upper and lower states, $\Delta\rho_{22}$ and $\Delta\rho_{11}$ and change in coherence terms, $\Delta\rho_{12}$ and $\Delta\rho_{21}$ which resulted in response to the laser interaction over the small time step. The output values of $\Delta\rho_{11}$, $\Delta\rho_{22}$, $\Delta\rho_{12}$ and $\Delta\rho_{21}$ were then added to the initial conditions before the next iteration. The program was looped over time such that the process repeated itself outputting the calculated values of ρ at each time step over a given range in t . These calculated values could then be plotted as a function of time. Since $\mathcal{V} = \frac{eE(t)X_{12}}{\hbar}$ and $E(t)$ is defined for a Gaussian pulse as before the time dependence from the matrix comes from this term.

By plotting the population terms ρ_{11} and ρ_{22} (Figure 4.11) as a function of time, the time dependence of the population of the two states can be seen where one unit on the x-axis corresponds to $2\pi\mathcal{V}t$. In the case of 4.11(a) there is no detuning and the population can be seen to oscillate sinusoidally between the ground state and excited state with a period of $2\pi\mathcal{V}t$. \mathcal{V} is the Rabi frequency as has previously been defined and the oscillations are known as Rabi Oscillations. In Figure 4.11(b) the same plot has been made for a system with detuning factor $(\omega_0 - \omega)$ of $\frac{\mathcal{V}}{2}$ resulting in oscillations with a shorter period and a lower maximum population of the excited state.

4.4.4 The Pulse Area

The pulse area, Θ can be used to describe the state in which a system is left after interaction with a laser pulse[12]. It is therefore an important parameter which must be taken into account when modelling such laser-atom interactions. If a pulse is at resonance with a system, It is defined in equation 4.18 where μ_{12} is the dipole moment.

$$\Theta = \left| \frac{\mu_{12}}{\hbar} \int_{-\infty}^{+\infty} E(t) dt \right| \quad (4.18)$$

Figure 4.12 has been calculated using the before mentioned matlab program. It shows the response of a two level system to three pulses of different pulse areas where in this case pulse area has been controlled by altering the FWHM of the pulse (the temporal profile of the three pulses is shown in the top row). Since the program is unit-less, an arbitrary value of E_0 and μ_{12} have been chosen and the time axis is measured in number of cycles (for 800 nm, one cycle would correspond to 2.67 fs). It can be seen from Figure 4.12 that when $\Theta = \pi$, known as a “ π pulse”, the laser pulse results in a total inversion of the population. The population terms for the ground state and excited state are shown in red and blue respectively. For the middle pulse shown in Fig. 4.12 where the pulse duration is 4 cycles, the ratio of Θ/π is almost 2. From the plot of the population terms it can be seen that such a “ 2π ” pulse results in the population completing a full cycle, firstly a total inversion and then back again to the initial values i.e. one “Rabi Flopping” oscillation. The third plot shows an example of a longer pulse duration of 6 cycles. In this case, since the pulse area is under 3π the population terms oscillate twice, finishing just below the initial values. Had the pulse area been equal to 3π the population terms would have returned to the original values. The same trend follows for higher multiples of π and 2π with the total number of population oscillations increasing with Θ .

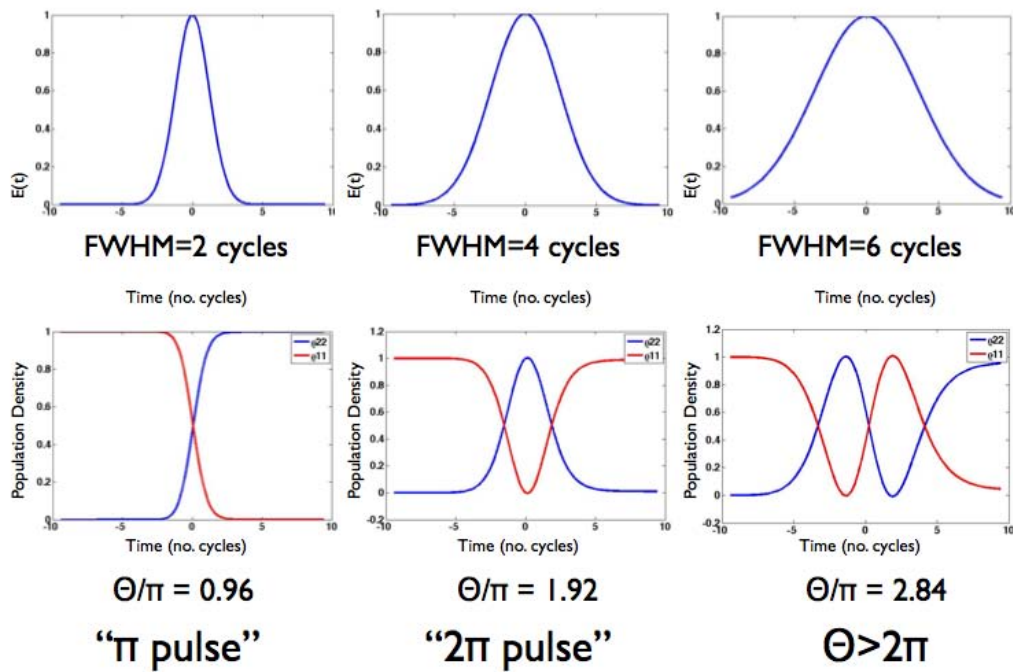


FIGURE 4.12: Time dependence of population for three different pulse areas. There are no damping terms included

In terms of the Matlab simulation the pulse area plays an important role since it can be used to match the program inputs to the experimental conditions. Measurements of the laser intensity and pulse duration can be used along with estimates of the dipole moment to calculate the pulse area. This pulse area can then be checked to make sure that the simulation input values represent the experimental conditions. It is important that a π pulse or less is used so that the lifetime of the excited state of interest can be measured i.e. that the population change is caused by spontaneous rather than stimulated emission. In order for the effects of spontaneous emission to be taken into account and incorporated into the Matlab program it is necessary to include damping terms into the Optical Bloch Equations [126].

4.4.5 Damping Terms

Damping terms have been added to the Optical Bloch Equations following the method used in references [12, 26, 28, 31, 34]. In this case the equations for a simple two level system are given by Equation 4.19 and Equation 4.20.

$$\frac{d\rho_{22}}{dt} = -\frac{d\rho_{11}}{dt} = -\frac{1}{2}i\mathcal{V}\tilde{\rho}_{12} + \frac{1}{2}i\mathcal{V}\tilde{\rho}_{21} - \frac{\rho_{22}}{T_1} \quad (4.19)$$

$$\frac{d\tilde{\rho}_{12}}{dt} = \left(\frac{d\tilde{\rho}_{21}}{dt}\right)^* = \frac{1}{2}i\mathcal{V}\rho_{11} - \frac{1}{2}i\mathcal{V}\rho_{22} + i(\omega_{12} - \omega_l - \frac{1}{T_2})\tilde{\rho}_{12} \quad (4.20)$$

T_1 is the energy (i.e. population) damping term which corresponds to the lifetime of the excited state. T_2 is known as the total dephasing time and is given by the following:

$$\frac{1}{T_2} = \frac{1}{2T_1} + \frac{1}{T_2^*} \quad (4.21)$$

Where T_2^* is the "true dephasing" term [31] and accounts for the decay in coherence of the system without any population decay [129] which occurs as a result of elastic scattering. Whilst the elastic collisions by definition only affect the off-diagonal density matrix elements by relaxing off diagonal matrix elements [130] and not the state populations, spontaneous emission and ionisation affect both the population of states and also the coherence.

The value of T_2 or T_2^* could not be taken directly from any of the PES data from the HOPG surface (In 2PPE experiments it is possible to measure T_2 from the intrinsic linewidth measurements, Γ as $\Gamma = 2/T_2$). As suggested by Hertel et al. for resonant and coherent transitions the assumption $T_2 = 2T_1$ was made [31] where T_1 was the free parameter to be varied. Initially sensible estimates based on previous lifetime measurements of similar states [29, 32, 94] of few to tens of femtoseconds were used for the lifetime of the excited state, T_1 .

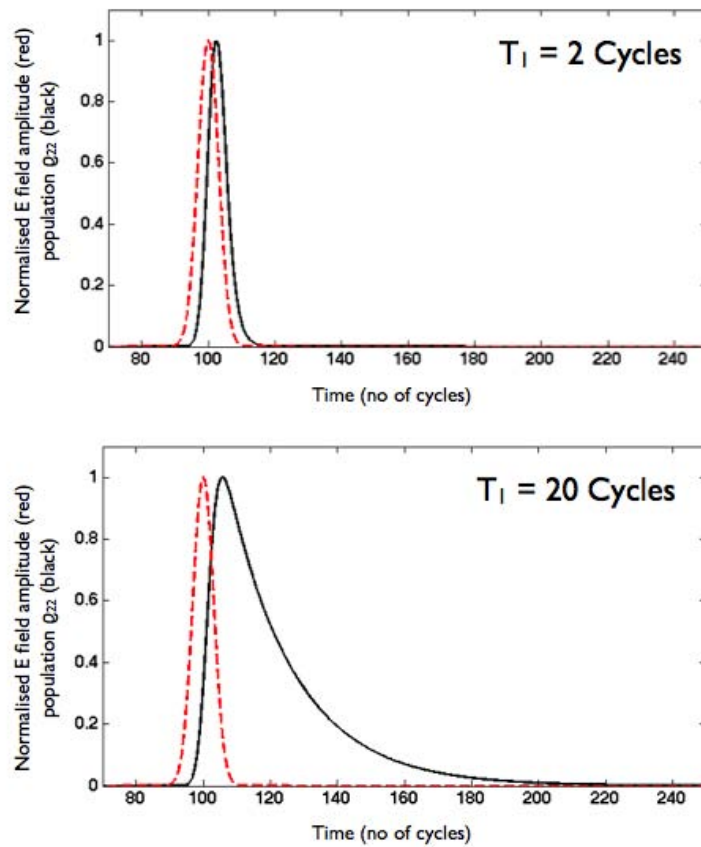


FIGURE 4.13: One Pulse OBE Simulation: The population of the excited state ρ_{22} as a result of one pulse is simulated for two different excited state lifetimes T_1 . The pulse area, $\Theta = 0.02$, and a pulse of 5 cycles (13 fs pulse for 800 nm) was used. The black line shows the normalised population term and the red dashed line shows the normalised E-field temporal profile for comparison. The x-axis is given in units corresponding to complete cycles with the arbitrary value of 100 given to the peak of the E-field. For $T_1 = 2$ the risetime (temporal difference between the E-field peak and population peak) is 2.4 cycles and for $T_1 = 20$ this increases to 5.7 cycles.

Fig. 4.13 shows the population of the upper state of a two-level system in response to one laser pulse as a function of time. The affect of the parameter T_1 can be seen by comparison between the two plots of $T_1 = 2$ and $T_1 = 20$. Figure 4.14 shows a model of the same population term as a function of pump-probe delay between two equal pulses in an IAC experiment. To model the Interferometric Autocorrelation measurements i.e. the excited state population as a function of pump-probe delay, the matlab program was modified to calculate the population terms as in Figure 4.13 but this time as a function of the combined E-feld of the

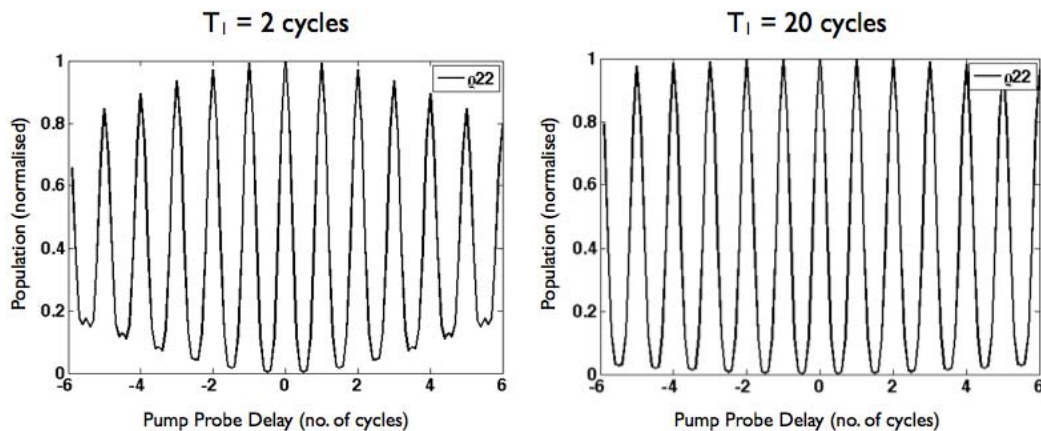


FIGURE 4.14: Lifetime Dependence of Interferometric Autocorrelation Model: The same parameters were used as in Figure 4.13 however for an Interferometric Autocorrelation experiment. In this case the x-axis corresponds to the time delay between the two pulses and is given in units of number of cycles.

two pulses. The program was then put inside an external loop to iterate over the pump-probe delay τ and the total population term (integrated over time t) at each delay was plotted as in Figure 4.14.

4.4.6 A Two-Level OBE Model of a Multi-Level System

In order to model the IAC measurements at the HOPG surface it was necessary to incorporate the high orders of non-linearity measured into the Optical Bloch Equations. This was achieved by describing the multi-level transitions involved in a multiphoton process as a two level system. The method was based on that first proposed by Diels [12, 131]. The multi-level system was described as having a total number of levels = $n+1$, where the lowest level is $|0\rangle$ and the highest $|n\rangle$ i.e. n is the nonlinearity (number of photons) of the excitation process. The rates of changes in populations of the initial (ρ_{00}) and final (ρ_{nn}) states could then be calculated in the same manner as before for the standard 2-level OBE model, this time however using the modified differential equations Equation 4.22 and Equation

4.23. The off-diagonal matrix elements (ρ_{0n}) once again described the coherence of the system.

$$\dot{\rho}_{0n} = i(\Delta_{0n}) + i\kappa_n \tilde{\varepsilon}^n (\rho_{nn} - \rho_{00}) - \frac{\rho_{nn}}{T_2} \quad (4.22)$$

$$\dot{\rho}_{nn} - \dot{\rho}_{00} = 2\kappa_n [\tilde{\varepsilon}^{n*} \tilde{\rho}_{0n} + \tilde{\varepsilon}^n \tilde{\rho}_{0n}^*] - \frac{\rho_{nn}}{T_1} \quad (4.23)$$

The term $\kappa_n \tilde{\varepsilon}^n$ in Equation 4.22 is the generalised Rabi frequency (given as \mathcal{V} in previous equations) for the multiphoton transition and is proportional to the electric field raised to the n th power. The scale factor κ_n is proportional to the product of all intermediate dipole moments of the multilevel transition [12, 131]. For the case of this work it was assumed that the dipole moments were all equal as with the simpler model a sensible estimate was made and checked using the pulse area. The electric field was again described by $\varepsilon(t) = \varepsilon_0 \exp(-t/t_G)^2$ for a single pulse and by $\tilde{\varepsilon}(t) = \varepsilon(t) + \varepsilon(t - \tau)e^{-i\omega\tau}$ for interferometric measurements. Δ_{0n} is the detuning of the final state.

Damping terms can be included as previously described (page 120) and are shown in Equation 4.22 and Equation 4.23 where T_1 is the finite relaxation time of the excited final state and T_2 the total dephasing rate (incorporating T_2^* is the ‘pure dephasing’ time which describes the decay in coherence of the system by elastic scattering processes [128]).

The coupled differential equations could be solved numerically as before, using the Matlab program. Depending on the description of the E-field used the population or coherence terms could be calculated either as a function of time for a single pulse, or in order to model the IAC measurements, as a function of pump-probe delay between two pulses.

Figure 4.15 shows the population of the n th state in response to a single pulse as a function of time (in number of cycles) for three different nonlinearities. A

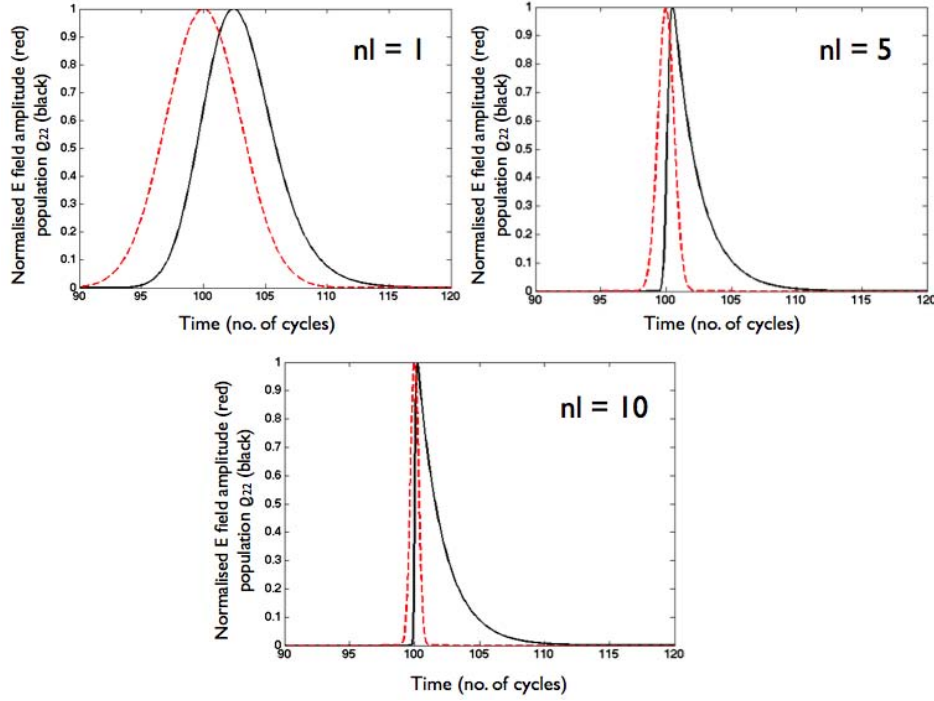


FIGURE 4.15: One Pulse Simulation Examining the Effect of Nonlinearity on Population of the Excited Final State: The plots show the population of the n th state as a function of time for three different multiphoton transitions, a one photon, five photon and 10 photon excitation respectively. The pulse duration modelled has a FWHM of 5 cycles and the lifetime of the excited state T_1 was set as 2 cycles. The red dotted line shows the envelope of the effective E-field in each case (i.e. $\tilde{\epsilon}^n$) which has been centred at an arbitrary value in time of 100 cycles.

resonant transition has been assumed (no detuning factor) and a lifetime of the excited state, $T_1 = 2$ cycles used. The short lifetime was chosen simply to make the axis more convenient. Measurements from the plots show that the time taken for the population to reach its maximum, the “risetime” decreases with increasing nonlinearity from 2.4 cycles for $n=1$ to 0.5 cycles for $n=5$ and 0.2 cycles for $n=10$.

$\tilde{\epsilon}^n$ is also plotted in the figures, shown by the red dashed lines. For the nonlinear picture the pulse area can still be described by the integral over time of the transition rate (the generalised Rabi frequency) Since the Rabi frequency is given by $\kappa_n \tilde{\epsilon}^n$, the equation for pulse area becomes $\Theta_n = \left| \int_{-\infty}^{+\infty} \kappa_n \tilde{\epsilon}^n dt \right|$ [12].

The effect of nonlinearity, n on the autocorrelation shape can clearly be seen in

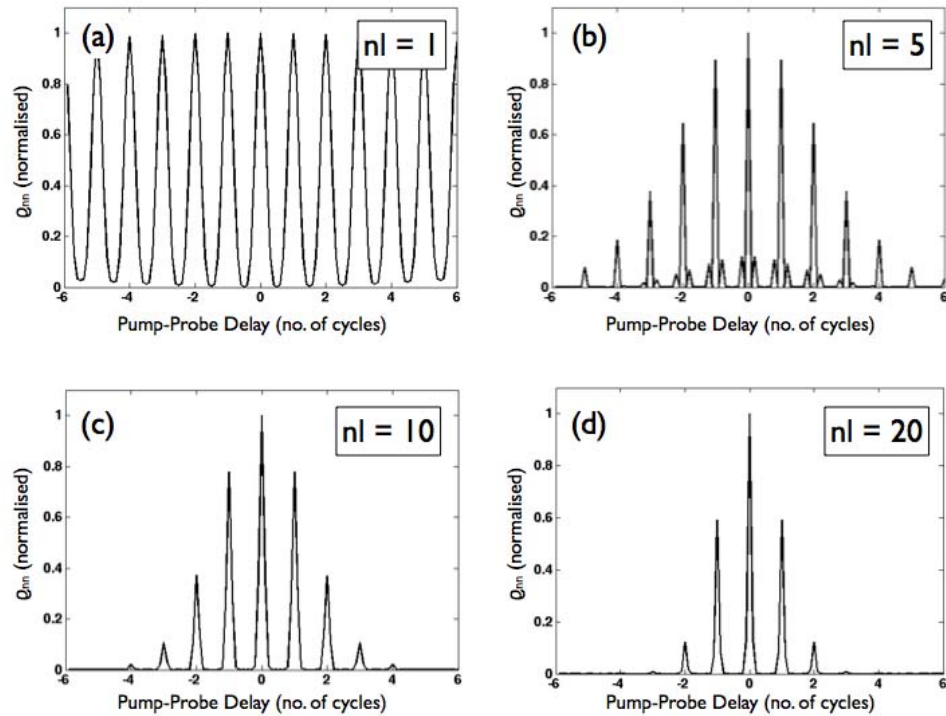


FIGURE 4.16: Interferometric Autocorrelation Simulation: Nonlinearity dependence. Equation 4.22 and Equation 4.23 have been solved for two identical laser pulses (FWHM 5 cycles) and the resulting population of the n th state is shown as a function of pump-probe delay for four different nonlinearities. The lifetime of the n th state was $T_1 = 20$ cycles and the detuning = 0

Figure 4.16. With increasing nonlinearity the FWHM of the envelope of the IAC decreases as do the width of the constructive fringes themselves. The number of actual fringes visible also decreases. For the 1st order process, sub peaks are visible at the extreme tails of the IAC (these are more clearly seen in Figure 4.14 for the case of $T_1 = 2$ cycles). These were also reported by Ogawa et al. and are shown in Figure 4.10 (c). They can be attributed to nonlinear polarisation terms as in the case of second harmonic generation at a surface. The sub-peaks also appear at $nl=2$ but then evolve with increasing nonlinearity to the sub peaks shown in Figure 4.16 (b) for $nl = 5$. For higher nonlinear orders of $nl = 7$ and above, the sub peaks are no longer visible as shown in Figure 4.16 (c) for $nl = 10$ and (d) for $nl = 20$. A simple comparison with the experimental data e.g. Figure 4.4 shows that whilst the highest KE photoelectrons have an IAC fingerprint similar to that

of the high order nl simulations Figure 4.16 (b)-(d), the lower KE features behave more as one would expect of a single photon transition such as those shown in Figure 4.14.

The detuning factor of the upper level [12] is defined as $\Delta_n = \omega_{0n} - n\omega_l$. For all the examples shown in this section detuning has been set to zero i.e. the multiphoton transition has been assumed to be resonant.

Different values of the detuning parameter have been tested and it has been found that for the most part the value of the detuning parameter does not effect the rise-time of the population term (the rise-time can observed using a one-pulse model) and so also has no effect on the IAC 2-pulse model. The overall population yield however does decrease as the detuning is increased. The exception to this was at low nonlinearities when a significantly large detuning factor was chosen such as $100\times$ Rabi frequency. At such values the population was found to follow the temporal profile of the pulse as observed by Hertel et al. for non-resonant transitions. If the program were improved to include a full description of multiphoton transition matrix elements as demonstrated by Georges et al. for a 4-level system [127] then detuning effects could be investigated in more detail however for such high-order processes the calculations required are considerably beyond the scope of this thesis. In the simulations made by Georges et al. the IAC shape looks different for non-resonant transitions as compared to resonant transitions. For the non-resonant case, oscillations are observed at long delays outside of the main envelope of the IAC that are not seen in their resonant model and which are not seen experimentally in the HOPG data for the ‘fast electrons’ (oscillations are observed at longer delays for the lower KE electrons of ~ 1 eV).

4.5 Comparison between Experimental Data and Simulations

4.5.1 Modelling the Interferometric Autocorrelation of High Kinetic Energy Photoelectrons Generated at the HOPG Surface using 13 fs Infra Red Pulses

As has been discussed in Chapter 3, high kinetic energy (peak at ~ 26 eV) photoelectrons produced at the HOPG surface by p-polarised 13fs IR laser pulses are believed to have been excited by a high-order multiphoton mechanism. Interferometric autocorrelation measurements of the photoemission have been reported in this chapter and since no competing excitation processes or saturation effects are believed to be present it is possible to simulate these time-dependent measurements using the Optical Bloch Equations.

Using Equation 4.22 and Equation 4.23 the IAC taken from the ‘fast’ electron signal (peak 26 eV) have been modelled. The number of photons involved in the excitation mechanism (i.e. the nonlinearity, n) have been extracted from intensity dependence measurements using the method previously described in Chapter 3. Previously, the average value of nonlinearity for each feature in the photoelectron spectrum was measured by plotting the integrated yield over the whole feature against the laser intensity. In fact it can be shown that if smaller sections are taken from within one feature of the photoelectron spectra, the nonlinearity will vary across the feature, increasing with increasing kinetic energy of the photoelectrons.

Fig. 4.17 shows the photoelectron spectra taken at three different laser intensities. Two extreme sections of the ‘fast electron’ feature are highlighted with kinetic energy ranges of 20-25 eV and 40-45 eV. The nonlinearity measurements for each section are shown below and yield a value of $n = 17$ and $n = 23$ respectively (The

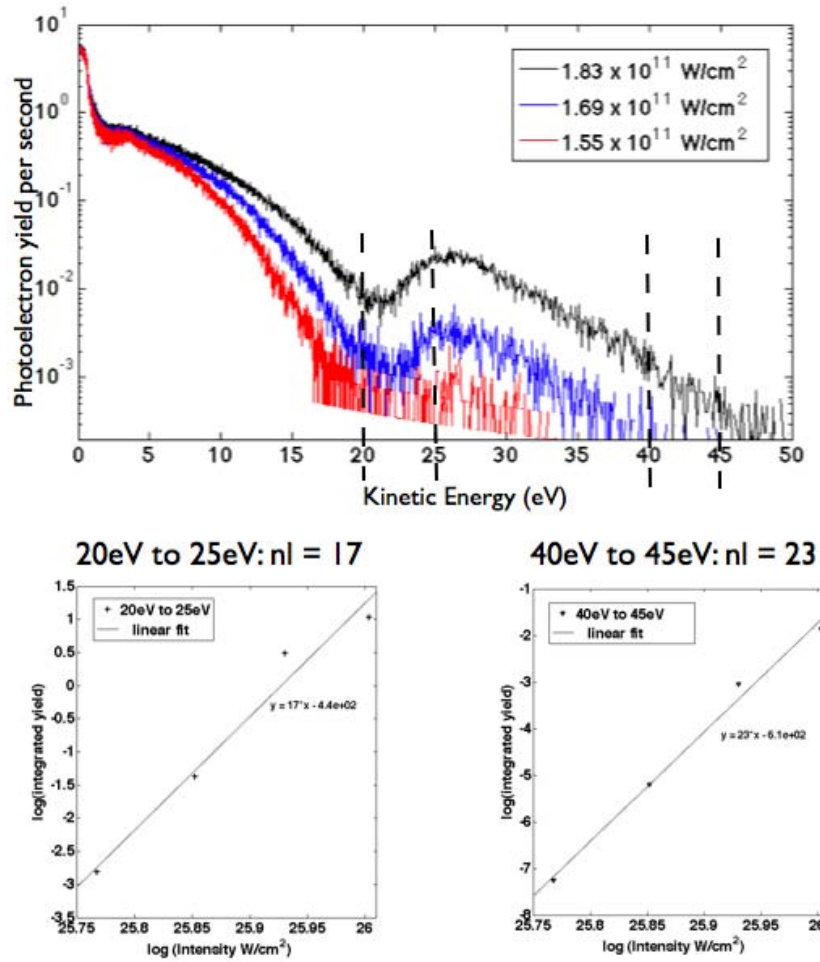


FIGURE 4.17: Extraction of Nonlinearity from Experimental Data: Two sections have been chosen from the high kinetic energy peak in the photoelectron spectrum with kinetic energy ranges of 20-25 eV and 40-45 eV. The log of the integrated electron yield over each section was plotted against the log of the laser intensity to measure the order of nonlinearity. These values were measured as $n=17$ and $n=23$ respectively.

averaged value of nonlinearity previously calculated over the entire fast electron peak was 22). Based on the residuals of the linear fit an error of 20% is calculated for the order of nonlinearity.

These values of $n=17$ and $n=23$ were fed into Equation 4.22 and Equation 4.23 resulting in the plots shown in Figure 4.18 (a). To compare the results from the simulation with experimental data, integrated electron yields from the data are presented over the same chosen KE ranges of 20-25 eV and 40-45 eV showing the corresponding ‘slice’ of the experimental autocorrelation Figure 4.18 (b). A spline

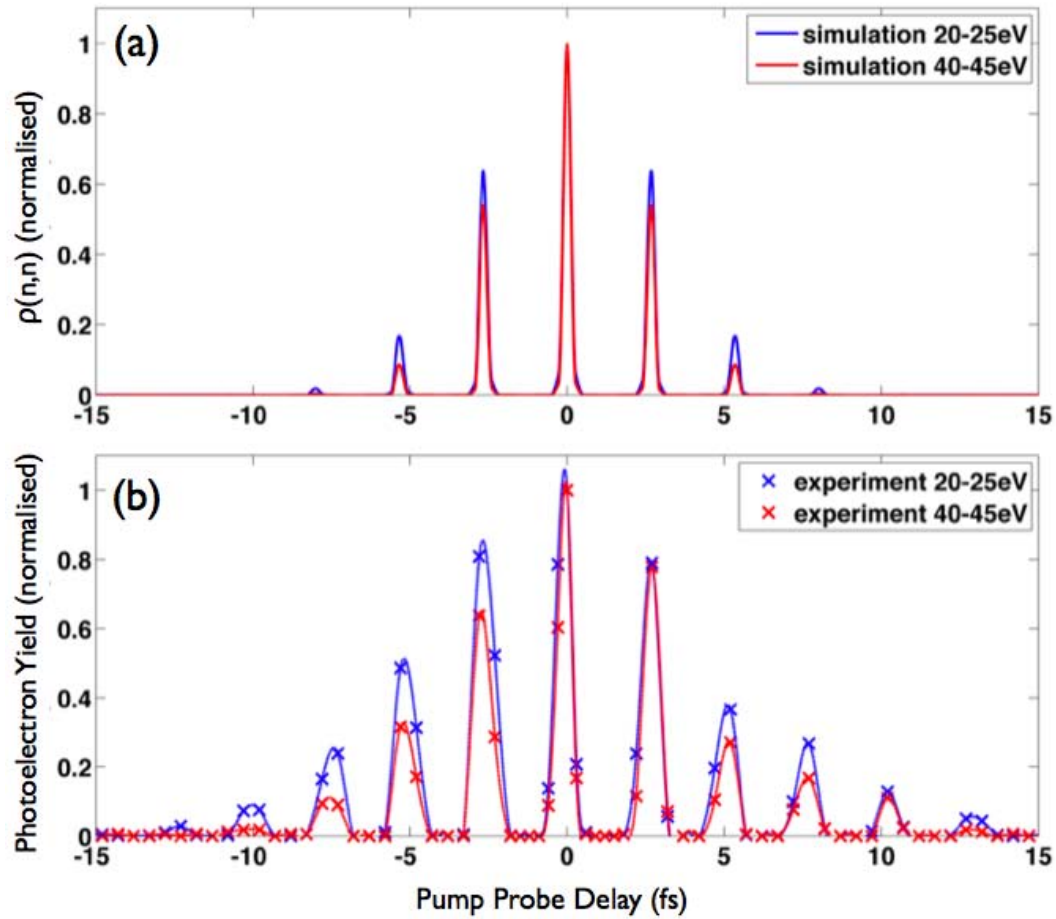


FIGURE 4.18: A Comparison Between Interferometric Autocorrelation Measurements and Corresponding Simulations made using the Optical Bloch Equations: (a) Simulations of the IAC for photoelectrons of energies 20-25 eV (blue) and 40-45 eV (red) where the nonlinearity value used in the model has been extracted from experimental data as shown in Figure 4.17. (b) Experimental measurements: the photoelectron yield integrated over the same energy ranges as in (a), plotted as a function of pump-probe delay

fit of the experimental data has been added to the plot to aid comparison between the two.

From Figure 4.18 it can be seen that the differences between the two experimental autocorrelation traces are reproduced well by the two simulations, where only the value of nonlinearity has been changed. It is clear that the shape of the autocorrelation trace is dependent on the number of photons involved in the excitation. For both the experimental data and the simulation the FWHM of the IAC envelope is seen to decrease for higher photoelectron kinetic energies (i.e. a higher nonlinear

order). The interference fringes themselves can also be seen to become narrower with increasing nonlinearity.

The autocorrelation trace taken from the experimental data has a slightly asymmetrical shape. This is thought to be due to laser instabilities and the subsequent temporal broadening of the pulse throughout the experiment. The simulated interference fringes also appear narrower than their experimental counterparts. This can be due in part to the limited resolution of the delay times as the central fringe, where smaller steps in delay time were taken appears much sharper. Unfortunately improvements in the resolution that could have been made by using smaller step sizes would have been at the expense of a longer experimental time and therefore more laser drift.

The FWHM of the IAC envelope is also smaller in the simulation than for the experimental data. Since the model assumes a multiphoton excitation process, any such differences could indicate the presence of other excitation mechanisms (i.e. tunnel ionisation). The broadening of the experimental data however should not be affected by the transport of the excited electrons through the material since at the energies observed, the mean free path of an electron is only a few angstroms and so the electrons recorded must originate from the top layer of graphite. Dispersion of the ultrashort pulses due to the airpath and optical components were fully accounted for in the FROG measurements so the greater FWHM of the envelope in the experimental case is unlikely to be due to an under-estimate of the pulse duration.

For the purpose of the simulations shown in Figure 4.18 the value of the scale factor, κ was chosen so that $\Theta = \int \kappa_n \tilde{\epsilon}^n dt \ll \pi$. For such values of Θ there will be no population saturation or Rabi flopping. The initial estimates for the damping parameters were chosen, based on previous measurements of excited states in graphite [29, 32, 94], as $T_1 = 20fs$ for the lifetime of the excited state and the

relationship $T_2 = 2T_1$ [31] as before. Other values of T_1 were also tested ranging from sub-cycle timescales up to 52 fs (20 cycles). In fact it was found that at these high orders of nonlinearity the shape of the IAC became only very weakly if not at all sensitive to the decay terms. This observation can be explained by the fact that for highly nonlinear orders the probability of exciting the electron to the n^{th} state vanishes extremely rapidly once the two pulses are not directly overlapped in time. The shape of the autocorrelation will therefore depend much more strongly on this probability of excitation than on the relaxation properties of the excited state.

4.5.2 An OBE Simulation of IR Pump-XUV Probe Experiment at the HOPG Surface

The OBE's have also been used to provide further understanding of the IR-XUV pump-probe experiments made at the HOPG surface (page 107). The experimental data revealed that the generation of photoelectrons across the entire energy range of the photoelectron spectrum was enhanced around the zero delay point where the two pulses overlapped in time.

Since there is no photoelectron signal produced by the IR pulse alone, any excited state populated by the IR pulse must lie below the vacuum level. Xu et al. [32] studied the lifetime of such conduction band states in graphite. They reported that the lifetime of the conduction band state followed a linear inverse relationship with the energy of the state. Figure 4.19 shows their data where the x-axis gives the energy above the Fermi level and the y-axis shows the lifetime in femtoseconds.

Estimates for the lifetimes of states that could be excited by the IR pump pulse were taken from Figure 4.19 and were used as the free parameter T_1 in the Matlab program to solve the OBE's for a single pulse. It was assumed that the probe (XUV) pulse excited the electron simply from the conduction band state of interest

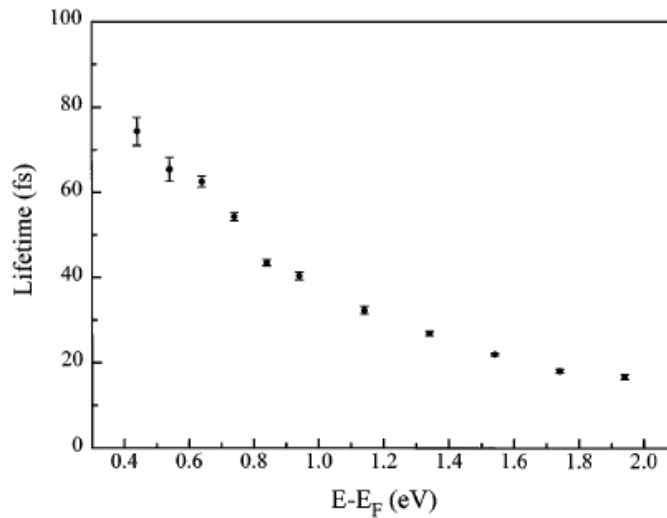


FIGURE 4.19: Lifetime of Conduction Band States in HOPG vs. Energy above the Fermi Level taken from [32].

to the detector (as in the work by Hertel et al. [31]) so the simulation of the population term resulting from the pump pulse alone represents the photoelectrons observed. As in the previous simulations presented in this chapter the conditions $\Theta \ll \pi$ and $T_2 = 2T_1$ were used.

Assuming that the initial state for electrons is the π band 2-3 eV below the Fermi level where the density of states is known to be greatest [82] it is most likely that a 2-photon or 3-photon process would be responsible for the excitation since a single photon transition would not give the electron sufficient energy with which to overcome the Fermi level. Also, if the work of Xu et al. [32] is correct then a higher final energy is more likely to lead to the relatively short FWHM of ~ 30 fs observed experimentally (taken as a rough value from the experimental points in Figure 4.20). For a 3-photon excitation the total photon energy is $3 \times 1.55 = 4.65$, if the initial state was 3 eV below the Fermi level this gives $E - E_F = 1.65$ which corresponds to a state with a 20 fs lifetime [32]. Figure 4.20 shows the experimental data points along with three separate examples of the OBE simulation using input parameters of 20 fs for the lifetime of the excited state, and the nonlinearity equal

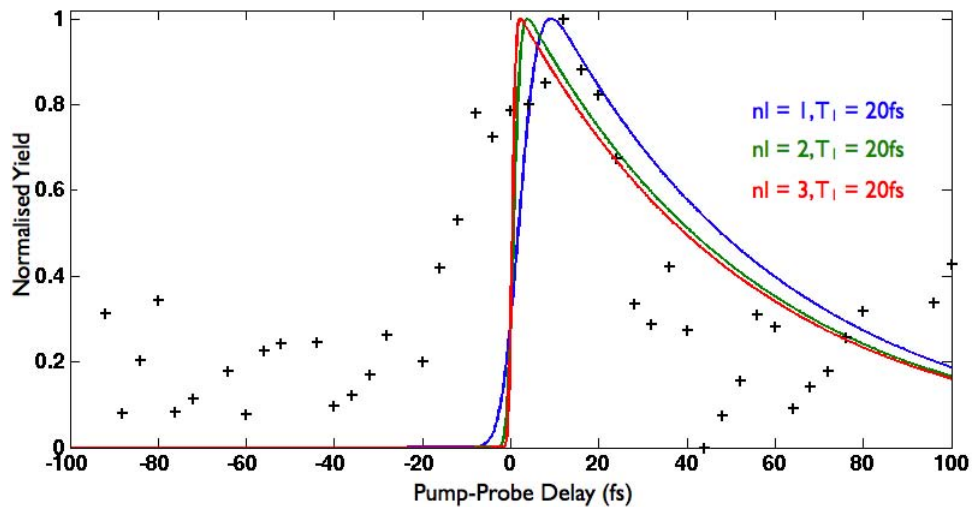


FIGURE 4.20: Comparison Between Experimental Data for IR pump-XUV probe Measurements and Simulations Made Using the Optical Bloch Equations: Experimental data is shown as black crosses and the simulation by coloured lines. The lifetime of the excited surface state was estimated as 20fs and the number of photons required to excite it varied between 1 (blue), 2 (green) and 3 (red).

to 1, 2 and 3.

It can be seen from Figure 4.20 that the simulations do not show a great correlation with the shape of the experimental data however the peak yield of the experimental data lies within the range of peak positions predicted by the three simulations and the FWHM predicted using the OBE's is also comparable to that measured experimentally. The short rise-time of <5 fs predicted by the OBE simulations however is not observed in the experimental data which shows a more symmetrical shape. If the laser drift background was not strictly linear as assumed it is possible that the removal of the background could result in such a distortion of the rising slope of the pump-probe trace. Unfortunately as the intensity of the laser was not recorded during experiments this cannot be confirmed.

By varying the input parameters of the simulation it could be seen that the rise time increased with increasing lifetime T_1 of the excited state but decreased with increasing nonlinearity. The FWHM of the population peak, i.e. the tail of the

peak, was found to increase with T_1 and also with increasing nonlinearity. Whilst the longer rise-time shown for the first order excitation (blue line in Figure 4.20) is more representative of that observed experimentally Xu et al. predict longer lifetimes (up to 80 fs) for conduction band states just above the Fermi level. It is clear from the experimental data that the surface state excited could not have such a long lifetime. It is therefore possible to predict that a 2-photon or 3-photon process excites the state.

4.6 Summary and Discussion

4.6.1 Summary: Interferometric Autocorrelation Measurements of the Photoelectron Emission Generated at the HOPG surface by 13 fs IR pulses

Interferometric Autocorrelation measurements of the photoemission signal generated from the HOPG surface by two equal 13 fs IR pulses have been presented. The shape of the autocorrelation has been shown to vary significantly across different kinetic energies taken from the photoelectron spectrum. For p-polarised light the Optical Bloch Equations have successfully been used to model the autocorrelation fingerprint. Using OBE's modified for multiphoton transitions and taking estimates of the nonlinearity from intensity dependence measurements (Chapter 3) the simulation was found to match well with the experimental data and changes in the envelope shape and fringe linewidth of the IAC that occurred with increasing electron kinetic energy were reproduced by the simulation. The good fit between the experiment and the simulation proves that for the case of p-polarised light, a multiphoton mechanism can be used adequately to explain the fast electrons observed.

For the case of s-polarised light the multiphoton mechanism did not match up (i.e. kinetic energies observed did not match the nonlinearities measured) and so it is thought that competing excitation processes are present, whether these competing processes are thermal or tunnelling in nature they can not be accounted for using this OBE model.

The OBE simulation itself showed that a relatively simple two level system could be used to describe a resonant multiphoton transition, even at extremely high nonlinearities. At such high nonlinearities it was found that the shape of the interferometric autocorrelation relied almost exclusively on the number of photons involved in the excitation process with very little effect from the lifetime of the excited state or detuning of the system.

4.6.2 Summary: IR Pump-XUV Probe of the HOPG Surface

An IR-XUV pump-probe experiment has shown that 7 fs IR pulses of low intensities $< 1 \times 10^{10}$ W/cm² incident on the HOPG surface can be used to excite low-lying conduction band states i.e. below the vacuum level. The lifetime of the excited state has been probed using XUV pulse trains. The Optical Bloch Equations have been used to simulate the population of the excited surface state as a function of time.

Qualitatively the experimental data shows some resemblance to the electron yield predicted by the OBE's however the sharp rise-time expected in the yield is not reproduced in the data. It is possible that background removal from the data could contribute to such differences. If the results could be repeated it would be beneficial to record the laser intensity at each photoelectron measurement throughout the experiment so that any background drift could be corrected for more accurately. A feedback system using electronically controlled mirror mounts to correct

for the drift is also planned. Of course, it is also possible that the symmetrical shape could be due to an excitation process that cannot be accounted for by the OBE Model.

As the first experiment for the XUV-IR beamline, several experimental difficulties had to be overcome to obtain data, the most notable being interference between the pump and probe pulses in the HHG gas jet. Despite improvements made however there is still plenty of scope for improvement for future work. Most importantly for successful IR-XUV experiments the issue of low signal intensity must be improved upon. One way in which this could be improved significantly with minimal effort would be to install a bigger toroidal mirror as this accounted for a 90% loss of IR intensity. The improvement in IR pump signal could also mean that a greater proportion of the initial IR pulse could be used for harmonic generation thereby increasing both pump and probe. Unfortunately such changes were not possible during the beam-time scheduled for these experiments. Whilst the collaboration between the two institutions has now come to an end the XUV-IR experiments have given valuable experience to both sides regarding attosecond measurements at surfaces. Imperial College are now drawing on the experience to create their own surface science chamber to be used with the beamline reported in this chapter and at NPRL in Birmingham there is now a new laser capable of producing pulses of a few cycle duration (once a hollow fibre apparatus has been installed), which could ultimately be used to provide attosecond pulses using a pre-existing HHG beam line.

Chapter 5

Velocity Map Imaging at the HOPG Surface

5.1 Introduction

Velocity Map Imaging (VMI) is a technique primarily used in gas phase chemistry to study the energy released when molecular bonds are broken as a result of laser excitation. The method is an extension of the standard time-of-flight technique with the key difference being the ability to measure the component of initial velocity perpendicular to the central axis of the detector. The principle is summarised in Figure 5.1 where it can be seen that the displacement, x measured using an imaging MCP (Multichannel Plate) detector is given by the product of the velocity component and the time of flight. A key technique in modern VMI measurements is the ability to sample the velocity distributions of ionised particles in such a way that all ions/electrons generated with the same initial velocity vector will be imaged at the same point on an imaging MCP detector.

In this chapter a new design of a velocity mapping instrument is tested whereby the imaging technique has been applied for the first time to the authors best

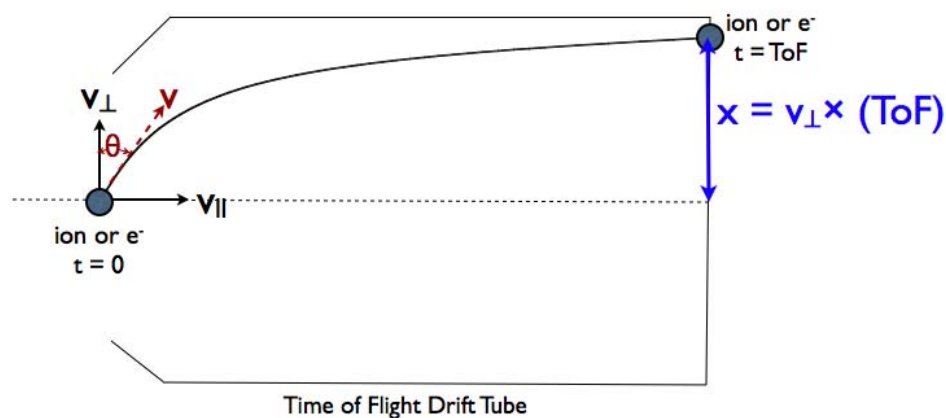


FIGURE 5.1: A Schematic Diagram to Show the Principle of Velocity Map Imaging: An MCP detector records the position, x of an electron or ion which is determined by the product of the component of velocity perpendicular to the drift tube axis and the time of flight (labelled ToF).

knowledge, to study ions and electrons generated by laser/surface interactions. Angularly resolved photoelectron emission measurements from the HOPG surface are presented and comparisons made where possible to the earlier work from Chapter 3 and Chapter 4.

5.2 Background

5.2.1 Ion Imaging and Velocity Map Imaging

Ion imaging apparatus was first demonstrated by Chandler and Houston in 1987 [132] who investigated the photodissociation of methyl iodide CH_3I using a crossed beam set-up, showing that it was possible to measure directly the angular distribution of the ions created. Ions were accelerated by an extractor consisting of a pair of grids and imaged using a microchannel plate (MCP) and phosphor screen (Fig. 5.2). A CCD camera could then be used to record this two-dimensional projection of the three-dimensional velocity distribution of the “ion cloud” [132]. The main

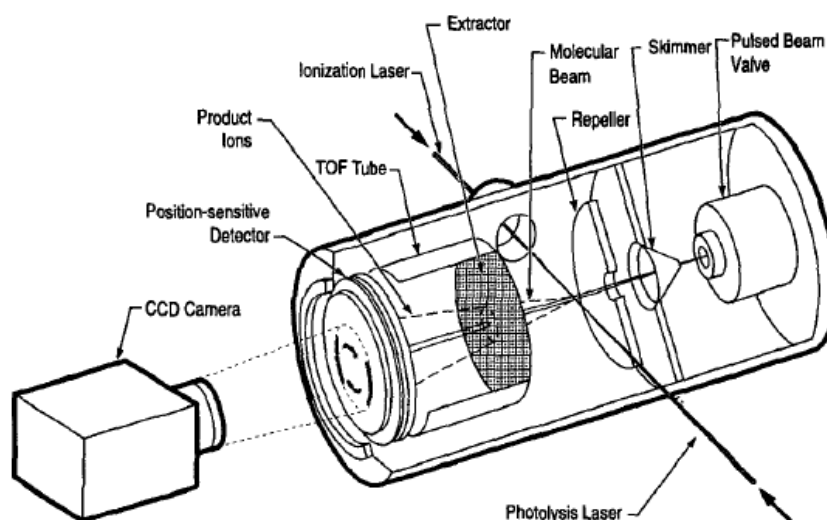


FIGURE 5.2: Schematic diagram of ion imaging apparatus used by Chandler and Houston (1987) to study the photo-dissociation of methyl iodide. Figure taken from [133].

drawback of this type of apparatus is that the image recorded is a convolution of both the angular distribution and the spatial distribution of the ions i.e. the angular resolution is limited by the range in initial positions from which the ions are created.

Eppink and Parker (1997) solved the issue of resolution by replacing the extractor grid with electrostatic lenses [134]. This technique, known as “velocity map imaging” (VMI) allows for all particles produced with the same initial velocity vector to be mapped onto one single point on the detector irrespective of their initial positions in the interaction.

5.2.2 Image Analysis Methods

In the traditional case of gas phase experiments such as photodissociation or photoionisation an excitation event will lead to the production of two fragments which, in the centre of mass frame, will fly in opposite directions with equal momentum.

Over time, if the event is repeated many times, the fragments will form a spherical distribution in velocity space. This distribution is known as a Newton sphere.

In VMI experiments it is common to explain results using the term Total Kinetic Energy Release (TKER), defined as the total excess energy left over after subtracting the internal energy of the products created. In photoionisation experiments the photoelectron will get all the TKER as its mass is so much smaller than that of the resulting ion however for dissociation of a symmetrical molecule such as O_2 the TKER would be shared equally between the two oxygen atoms. Since ionisation or dissociation products with a lighter mass will therefore have more velocity their newton sphere will have a larger radius as compared to a product with a greater mass. The recorded image seen on an MCP detector is a two dimensional projection of this three dimensional distribution so the objects with higher kinetic energy will be observed nearer the outer edges of an MCP detector. The polarisation of the laser used to initiate the process of interest will also have an effect on the resulting image since molecules will align themselves along the polarisation axis leading to an an-isotropic pattern.

One way to deconstruct the Newton sphere is using an Abel transformation which extracts the information from the 2D image that has been crushed from the original 3D projection [135]. It works by taking a function of x and converting it into polar co-ordinates using Fourier transform convolution theorem [133]. Collecting data from the entire Newton sphere creates a large amount of data and therefore gives a higher signal to noise ratio and better resolution than other methods. A standard inverse Abel transformation can only be used however if the image is azimuthally symmetric (i.e. has a cylindrical symmetry about an axis that is parallel to the face of the detector).

5.2.3 The Slicing Technique

Another method of image analysis is known as “slicing” and can be used when the Abel transformation is not valid. When an event occurs and a Newton sphere is created, a delayed electric field pulse or constant low acceleration voltage can allow the sphere to expand before being projected onto an MCP [136]. A detector can then be gated to select only a narrow slice of the ion packet that is of interest [137] (In gas experiments the central part of the Newton sphere is usually selected). [138, 139]. There are some disadvantages to the slicing method; increasing the time delay causes peaks to broaden. As intended this allows slices to be made more easily up to a point however too much broadening can lead to overlap of close features eg. different isotopes. Even when there is only one isotope present then too much broadening can still be a disadvantage since it can lead to distortion effects that occur when the ion cloud gets to be the same size as ion optics [139].

5.3 The Velocity Map Imaging Experimental Set-Up

5.3.1 The Laser System: Spitfire Regenerative Amplifier

An overview of the laser system used in these experiments, based around a Spectra Physics Spitfire Regenerative Amplifier is shown in Figure 5.3. The purpose of the Spitfire laser cavity is to amplify the 80 femtosecond, 300 mW pulses generated by the Spectra Physics Tsunami, a mode locked Ti:Sapphire oscillator. The pulses produced by the Spitfire can have energies of up to 1 W and a minimum pulse duration of 100 fs.

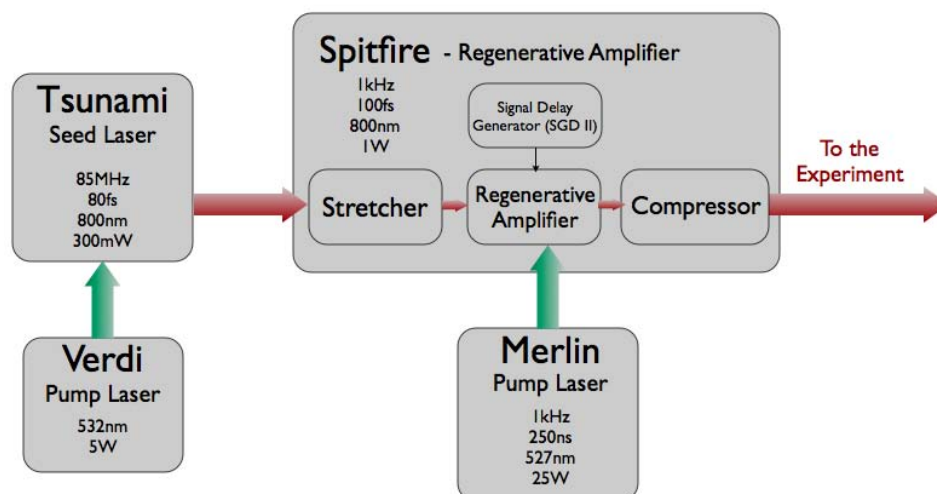


FIGURE 5.3: A Schematic Overview of the Spitfire Laser System

The amplification process is chirped pulse amplification (CPA) as described previously Chapter 3 (page 48). In the case of the Spitfire, the seed pulses from the Tsunami are stretched by a grating/mirror combination and then propagate the cavity. A synchronisation and delay generator (SDGII) is used to select which pulses propagate. After being selected the pulses will follow multiple passes through the Ti:Sapphire amplifier pumped by 25 W, 527 nm pulses from the Q-switched Nd:YLF Merlin laser. Before leaving the Spitfire cavity the amplified pulses are re-compressed by a second grating/mirror combination.

5.3.2 The Experimental Beamline

The experimental beamline is shown in Figure 5.4 is that used for pump-probe experiments at the surface. Pulses from the laser table are directed through a Mach-Zehnder interferometer as shown. They are split by the beamsplitter and then one pulse is delayed with respect to the other by increasing and decreasing the path length it follows using a retro-reflector mounted on a motorised stage that could be controlled by a LabView program. For single pulse experiments the same layout was used but with only one arm of the interferometer being used. It

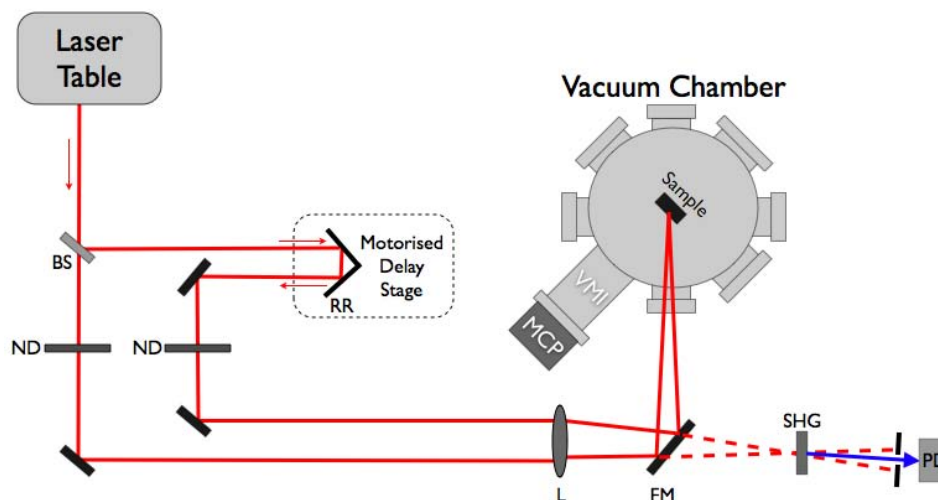


FIGURE 5.4: Schematic Diagram of the Beamline Set-Up for Pump-Probe Experiments at the Surface: A Mach-Zehnder Interferometer splits the output pulse from the laser table into two using beam splitter BS so that one pulse may be delayed with respect to the other by movement of the retro-reflector, RR mounted on a motorised stage. Light from both arms of the interferometer are focused by lens, L and re-combined at the focus on the surface in a non-collinear arrangement. Neutral density filters (ND) are used for energy attenuation of the pulses and a flipper mirror, FM can be flipped down to give a different beam path so that the pulse duration can be measured by SHG intensity autocorrelation.

was also possible (not shown in Fig. 5.4) to direct laser light through the ports lying at 90° angles to the axis of the VMI. Such alignment was not used in surface experiments but was used for initial testing in the gas phase. A thin convex lens is used to focus the two light paths onto the surface where they are re-combined (unlike the experiments of Chapter 3 and Chapter 4 the ~ 130 fs pulses do not have such a large bandwidth so dispersion effects are less of an issue). Laser attenuation is achieved using neutral density filters. A flipper mirror allows the beam paths to be changed so that the focus lies on the surface of an SHG crystal forming an SHG intensity autocorrelator that can be used to measure the pulse duration. The process has been described in more detail in the theory section on page 41, where Figure 2.17 shows an example of a measurement taken of the 130 fs pulses described in this section.

phase case and therefore the detector does not need to be designed to accommodate such a large acceptance range.

The sample can be grounded or a potential applied if desired giving an increased flexibility for the type of experiment that can be carried out. The entrance aperture acts to select the ions/electrons that may enter the detector. The geometry of the aperture diameter and its separation from the sample allows only electrons/ions from the surface to enter the detector. A potential can also be applied to the entrance aperture to attract particles however care should be taken with electrons as a large potential will affect the resolution of measurements.

Lens 1 and lens 2 are used to guide the charged particles through the detector and to reduce any astigmatism of the entrance optics. Such astigmatism takes the form of a curvature of the image plane which means that only part of the velocity distribution is imaged at the flat plane of the detector. Lens 1 and 2 can thus be used to reduce this curvature to the image plane generated by the entrance aperture since they are concentric with the aperture lens. Along with the other components to which the other potentials are applied, the lenses can be used to determine the mode of operation of the detector.

Imaging of the collected particles is achieved by a Micro-Channel Plate (MCP) which lies on a floating linear potential. Part of this, the base potential is present constantly throughout operation and the other part, the gate voltage is applied as required and is used to control the temporal window over which the MCP can “see” the electrons/ions i.e. for slicing measurements. A phosphor screen converts the multiplied electron counts into photons which are then observed using a CCD camera.

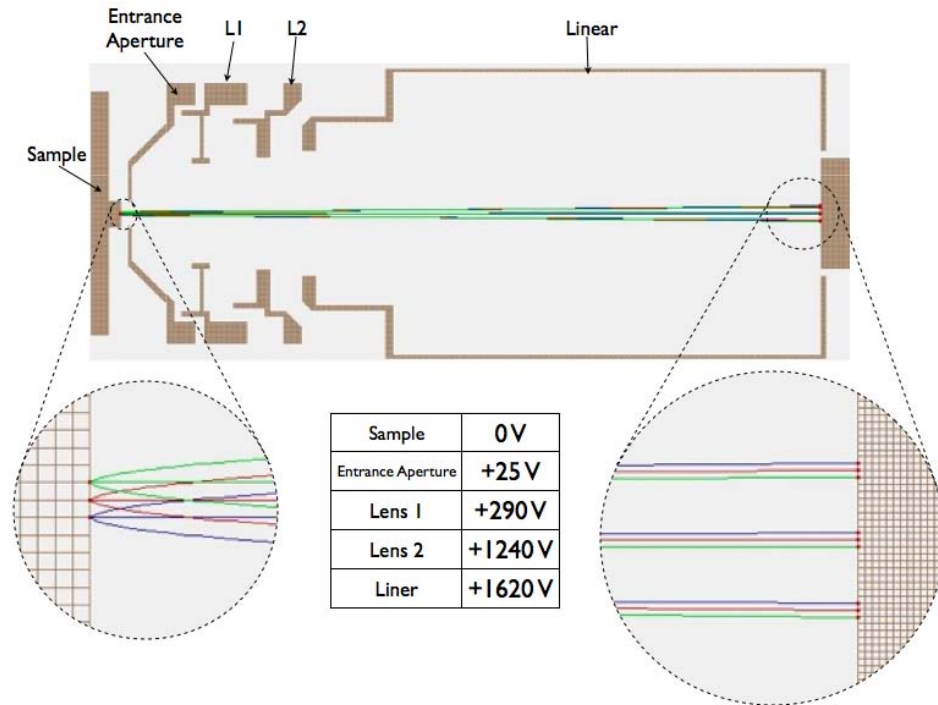


FIGURE 5.6: Velocity Resolution Mode: Simulation of 1 eV photoelectrons emitted from the HOPG surface when imaged in velocity map imaging mode (VMI). One grid unit (visible as squares in the zoomed view) is set as $250 \mu\text{m}$ so that the distribution of initial points corresponds to the diameter of the spot size of the laser on the surface.

5.3.3.1 SIMION Simulations of the Paths taken by Electrons in The VMI Detector due to Different Electrostatic Potentials Applied

A unique feature of this VMI detector, made possible by the chosen configuration of electrostatic lenses is that it can be operated in two different modes. By altering the potentials applied to the lenses it is possible to alternate between velocity resolution and spatial resolution. These two modes are shown in Figures 5.6 and 5.7.

For velocity map imaging, the voltages applied to the electrostatic lenses are chosen carefully to ensure that all ions/electrons which have the same velocity vector when leaving the surface will be projected onto the same point on the MCP irrespective of their initial position on the surface. A SIMION simulation of this mode is shown in Figure 5.6 where photoelectrons have been modelled for three different

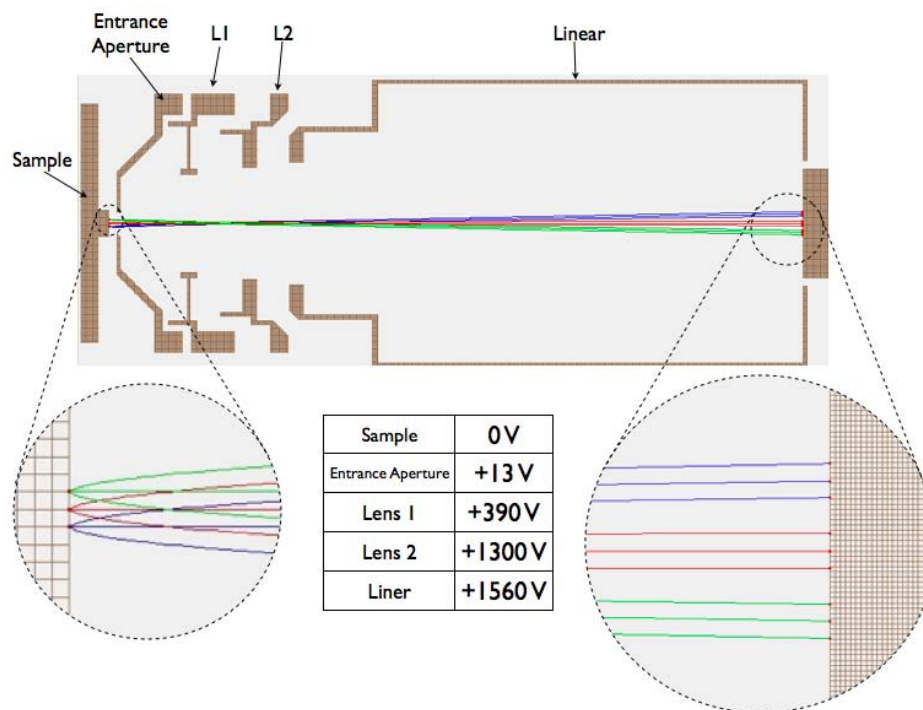


FIGURE 5.7: Spatial Resolution Mode: Simulation of 1 eV photoelectrons emitted from the HOPG surface when working in the “microscope mode”

starting positions within 0.5 mm of each other on the sample and for three different emission angles of -15 , 0 and $+15$ degrees at each starting point. It can be seen that the end position on the MCP is determined by the velocity vector and not by the starting position on the surface. In “Microscope Mode” as shown in Fig. 5.7 the opposite is true and the position on the MCP is a linear magnification of that on the surface.

5.3.3.2 Time Gating of the VMI Detector

As discussed on page 140, it is not possible to implement an Abel transform for surface experiments [135] it is therefore necessary to select the part of the photoelectron/ion spectrum of interest by its time of flight i.e. to use a slicing technique. It is well known that the time resolution of a VMI experiment is limited by the lifetime of the phosphorus screen to typical values of about 60 ns [141]. In the case of this detector, initial tests have shown the best resolution

to be 90 ns. A simulation was constructed using typical VMI-mode potentials to examine groups of photoelectron with different kinetic energies. Taking the 3 features of the PES measurements from HOPG reported in Chapter 3 which had respective kinetic energies of 1 eV, 6 eV and 30 eV it was predicted that their time of flight would be equal to 23.6 ns, 22.6 ns and 20.6 ns. This lies significantly below the resolution of the detector. Ions on the other hand were separated on a μs timescales so could be easily resolved.

5.4 VMI Measurements at the HOPG Surface

5.4.1 Intensity Autocorrelation Measurements in Velocity Mapping and Microscope Imaging Modes

Using the experimental beamline shown in Fig. 5.4 the photoelectrons generated at the HOPG surface using 130 fs 800 nm pulses were measured. Figure 5.8 (a) and (b) shows the raw data taken from the MCP at a set pump-probe delay using a laser intensity of $5.5 \times 10^{11} \text{W/cm}^2$ for velocity mapping and microscope mode respectively.

SIMION simulations have been made to analyse the velocity mapping data which is of main interest. The distance in pixels measured on the MCP detector has been converted into angle in degrees where 0° , the emission normal from the surface has been defined as the point of maximum signal on the MCP.

According to the principle of operation of the the VMI, particles with no transverse component of momentum will be recorded at the centre of the MCP screen. This can be seen in figure 5.6. Thus, the central area spot can be taken to correspond to the emission of electrons normal to the surface. Unfortunately, it is not possible to use the microscope mode measurements to calibrate the VMI measurements

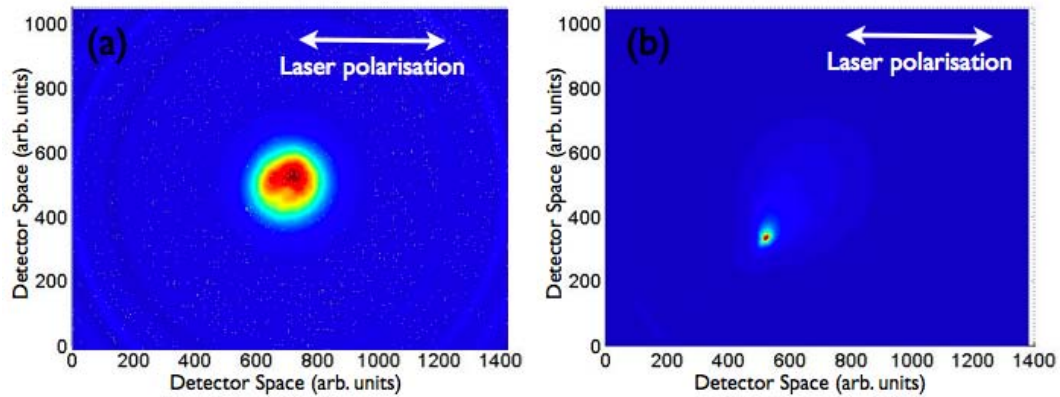


FIGURE 5.8: . Comparison of Photoemission Signal from the HOPG Surface using two Different sets of Potentials: (a) Raw data for velocity resolved mode (b) Raw data for spatial resolution mode. The laser was incident at a 45 degree angle to the surface as shown in figures 5.5 and 5.4.

since the microscope mode measurements give positional information only and the VMI measurements give velocity information only. However, the fact that the maximum electron signal in the VMI measurements is a peak in roughly the centre of the screen is highly indicative of a maximum at normal emission angles. In the corresponding simulation shown in figure 5.6 it can be seen that no matter where on the surface the electrons originate from, those emitted normal to the surface will appear central on the MCP screen. Note that this is despite the fact that the laser spot was not in the centre of the “view” of the detector, as shown in the microscope mode image of figure 5.8(b). It is worth noting that, according to the simulations, if the maximum angle of emission was for example 5 degrees in a particular direction with relation to the graphite lattice then this would lead in a shift of the image on the MCP in a particular direction, however if the preferred angle of emission were symmetrical i.e. 5 degrees in every direction, this would lead to a cone of photoelectron emission that would appear as a doughnut shape on the MCP. For the purpose of analysing these experiments a central maximum in electron emission has been assumed to correspond to electrons emitted normal to the surface. Clearly for a more accurate analysis it would be desirable to calibrate the signal using a sample with known emission properties however during the time

available this was not possible.

In Figure 5.9 slices have been taken across the horizontal and vertical axis of the MCP through the point of maximum signal and the distance along the detector from the maximum converted into angle. These slices or cross-sections (not to be confused with the “slicing” technique in time) have been plotted as a function of pump-probe delay. Figure 5.9 (a) shows a 3D plot of the slices taken across the horizontal axis, this is shown again from above in (d). Plot (b) shows the total integrated signal as a function of delay and (c) shows the same information as (a) and (d) but for slices made across the vertical axis. From this data it can be seen that the overwhelming majority of photoelectrons emitted from the HOPG surface leave the surface over a range of emission angles spanning a total 40 degrees. If the assumption is correct that the maximum signal corresponds to those photoelectrons emitted normal to the surface then this would correspond to photoelectrons emitted at angles of 20 degrees to the normal or less in either direction. Electrons emitted normal to the surface will correspond to those excited at the Γ point [142]. This would agree well with the Γ point transitions described in Chapter 3 to describe the photoelectron features presented in that chapter. Transitions from the M point may also be present and would fall within an emission angle of 20° [142]. At the higher laser intensities generated when the two pulses overlap in time, the angle at which electrons are emitted is seen to increase to values of up to 40° from the supposed normal emission angle. This broadening is likely to be caused by thermal effects or secondary electrons.

For interest, Figure 5.9 (c) and (d) can be compared to the same measurements using microscope mode. The x-axis has been converted to distance in mm on the surface and appears to be wider than the actual value of $108\mu\text{m}$ (horizontal) and $66\mu\text{m}$ taken from spot size measurements projected onto a 45° incident angle. This asymmetric spot shape reveals itself in Figures 5.10 (a) and (b) where the FWHM in (a) is wider.

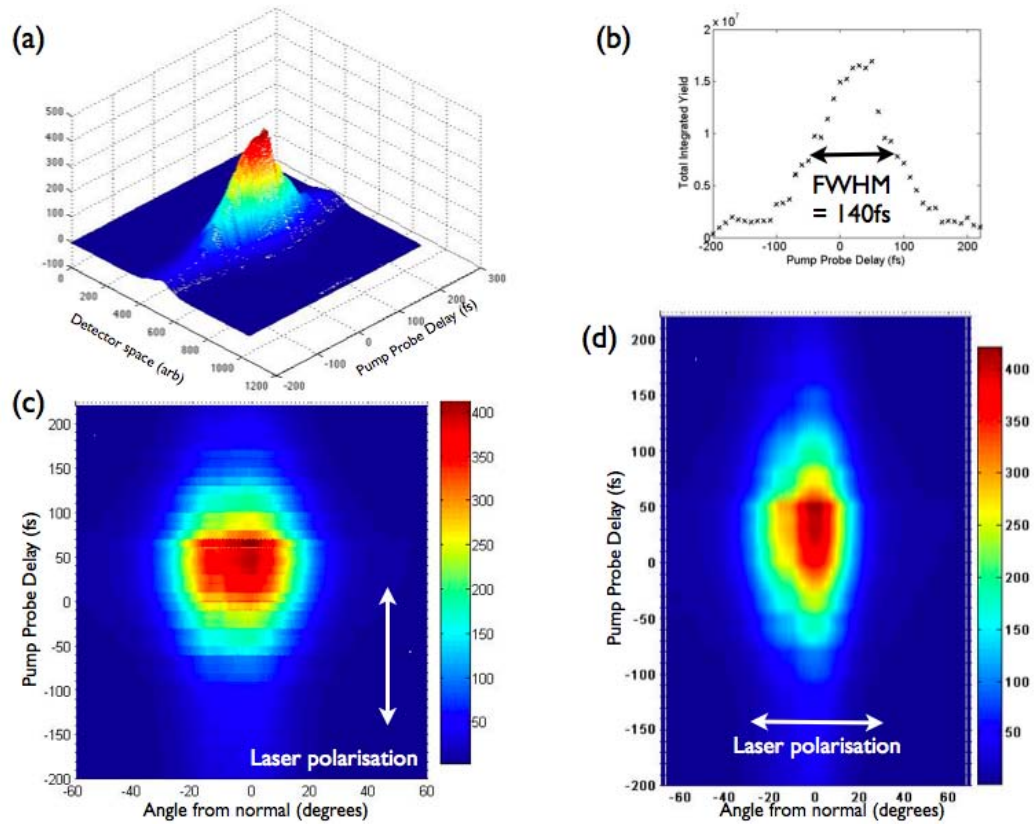


FIGURE 5.9: Intensity Autocorrelation of Photoelectrons from the HOPG Surface Using a Velocity Map Imaging Detector: (a) 3D plot showing slices taken from the maximum along the horizontal experimental axis (b) Total integrated yield vs. delay (c) Slices taken through the maximum signal point along the vertical experimental axis of the MCP as a function of pump-probe delay (d) as in part (c) but with slices taken along the horizontal axis

5.4.2 Intensity Dependence Measurements

Since it is not possible to separate the kinetic energies of different energy photoelectrons using the current VMI set-up, separate intensity dependence measurements were made to provide more information. Extracting the nonlinearities from Figure 5.11 (using the same method as that for the PES signal in Chapter 3) it can be seen that there are two different regimes, the first up to laser intensities of $\sim 5 \times 10^{11}$ W/cm² and the second from there on upwards. In the first regime the nonlinearity is estimated as 1.8 ± 0.19 for s-polarisation and 1.5 ± 0.25 for p-polarisation and in the second regime to nonlinearities of 0.58 ± 0.01 for s-polarisation and

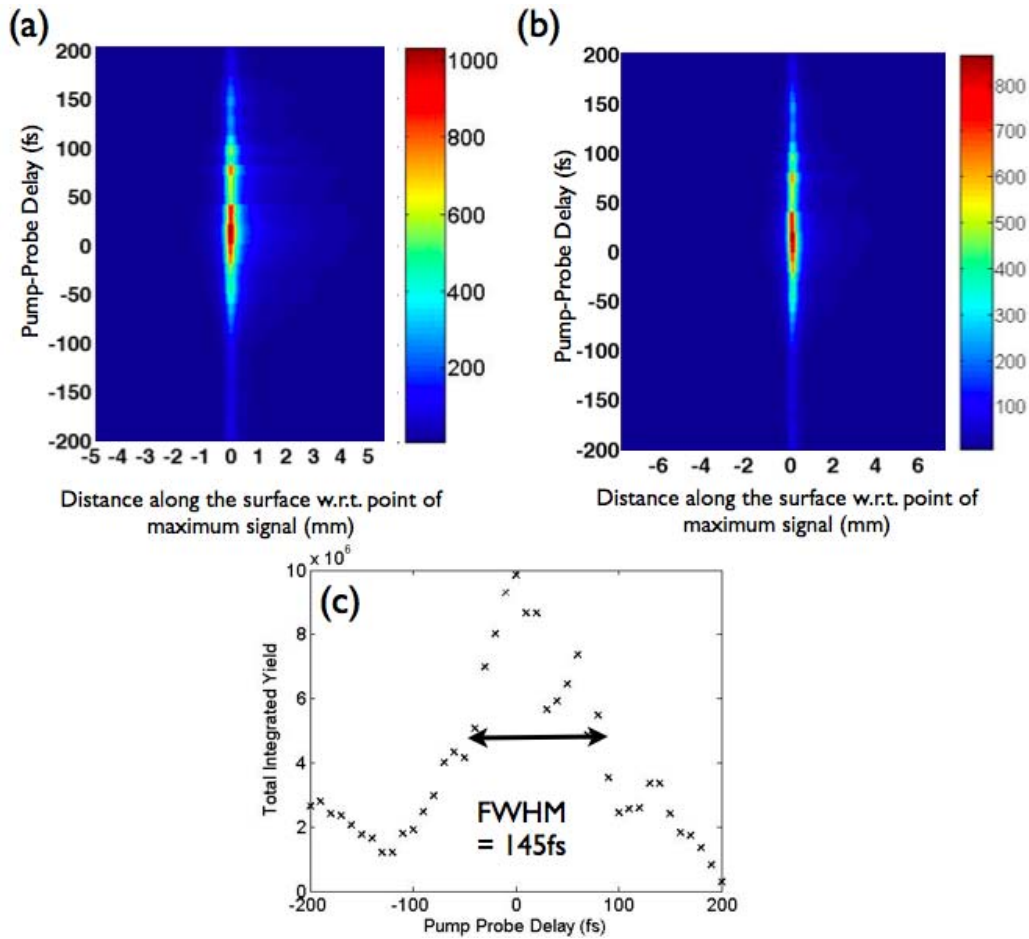


FIGURE 5.10: Intensity Autocorrelation of Photoelectrons from the HOPG Surface Using a VMI Detector in Microscope Mode: (a) slices taken along the horizontal axis vs. pump-probe delay (b) slices taken along the vertical axis vs. pump-probe delay (c) total integrated signal vs. delay.

0.54 ± 0.01 for p-polarisation. The nonlinearities measured for the “slow” photoelectron peak in chapter 3 for p-polarised light were 2 and 0.46 over two regimes (In Chapter 3, s-polarised light gave higher estimates of 3.7 and 0.8 respectively). Such values are similar to these VMI extracted nonlinearities, particularly for the p-polarised case, but lie outside of the experimental uncertainty of these VMI measurements. The observed similarity between the two experiments may suggest that the dominant photoelectron signal recorded using the VMI detector in either mode comes from energies with approximately 1 eV and below. One observation that should be highlighted is that although the intensity dependence behaviour appears to mirror quite well that previously seen in Chapter 3, the laser intensity

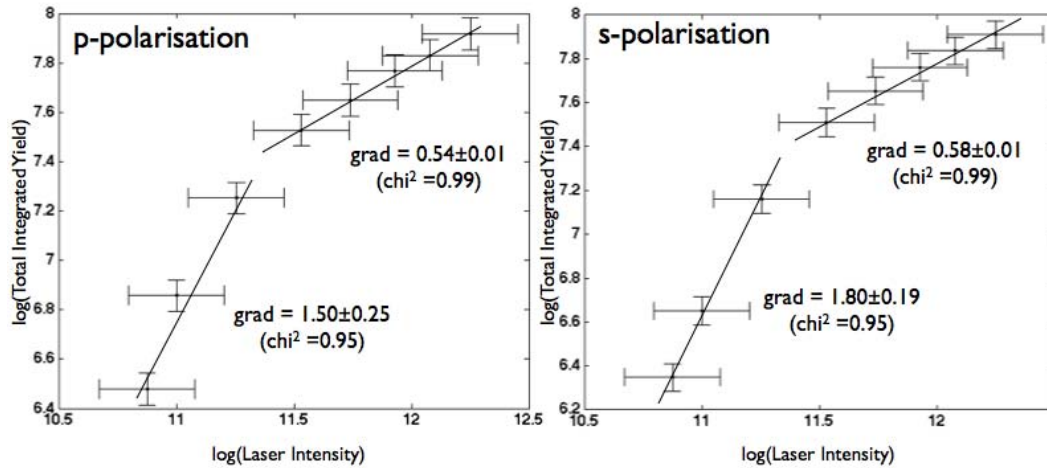


FIGURE 5.11: Nonlinearity measurements-Laser Intensity Dependence of the VMI Photoemission Signal generated at the HOPG Surface by 130fs IR pulses: The integrated yield was measured as the signal integrated over the area of the MCP and the nonlinearity (the gradient) was extracted as explained on page 71. Errors were also estimated using the methods previously described in Chapter 3 and Appendix C with the exception of the uncertainty of the total yield which was taken from the accuracy of the voltages applied to the MCP.

at which the nonlinearity changes is much higher in the VMI experiments. It is possible that this is because the laser intensity has been over estimated in the VMI experiments which is probable as alignment onto the surface at a 45° angle is difficult and it is quite likely that the laser could be clipped slightly before it reaches the surface. This would not have been accounted for during the spot size measurements.

5.5 Summary and Discussion

Initial testing of a novel velocity map imaging detector designed to work at solid surfaces has been presented. These initial tests have demonstrated that the angle at which electrons are emitted from the surface can be recorded using the imaging technique. It was not possible to calibrate the angles of electron emission from the surface however, the fact that the VMI image is central suggests that its peak corresponds to those electrons with normal emission angles. A central peak

of electron emission could correspond to those electrons emitted normal to the surface i.e. primarily from the Γ point. For the HOPG surface the majority of photoelectrons were measured leaving the surface at a range of angles believed to correspond to angles of 20° and below. Intensity autocorrelation measurements revealed a broadening at high laser intensities. It has also been shown that the detector can be configured to act in a “microscope mode” whereby the spatial distribution of the electrons are imaged rather than their velocity (component perpendicular to the time of flight axis). This was found to be useful in pump-probe experiments, allowing the spatial overlap of the two pulses to be checked.

It was revealed that the time resolution of the detector was limited by the response time of the phosphor screen used to image the MCP counts. This meant that it was not possible in the current configuration to measure the angular distribution for photoelectrons with different kinetic energies separately. Intensity dependence measurements matched those taken for low-energy photoelectrons presented in Chapter 3 suggesting that these kinetic energies (~ 1 eV) dominated the angular dependence measurements. It would be possible for the detector to be sent back to the manufacturer to adjust the floating potentials so that the detector would be more sensitive to electrons however this would be at the expense of ion measurements as smaller electrostatic potentials would not be sufficient to control their paths to achieve velocity map imaging.

Chapter 6

Conclusion

The work presented in this thesis has described measurements of photoelectron emission generated at the HOPG surface by ultrashort laser pulses. The thesis project was carried out as part of a collaborative research effort with an overall aim to generate, measure and demonstrate attosecond duration light pulses for the first time in the UK. The specific aim of this thesis project was to work towards attosecond measurements at surfaces, a goal which, prior to the start of the collaboration had never been achieved. Whilst experimental problems with the beamline prevented measurements with such fine time resolution it was possible to use both few-cycle infra red pulses and XUV pulse trains to study photoemission from the HOPG surface. Most interestingly it was found that in the strong field regime, at laser intensities below the damage threshold of the surface it was possible to generate photoelectrons with kinetic energies of up to 80 eV using incident infra red photons with only 1.55 eV energy.

Conclusions drawn from each chapter individually are presented below:

6.1 Chapter 3 Conclusion: Photoelectron Spectroscopy of the HOPG Surface

In Chapter 3 it has been shown that photoelectrons with kinetic energies of up to 80 eV can be generated by infrared 13 fs pulses with an initial photon energy of just 1.5 eV. Intensity dependence measurements were used to estimate the non-linearity of the excitation process which is found to be extremely high (with values of up to the 22nd order).

Comparison between the photoelectron spectra generated by the IR pulses and that taken using XUV pulse trains revealed a striking resemblance. It is suggested that the same final states which are excited by a single XUV photon can also be excited by the non-linear IR excitation. This demonstrates that band structure effects can survive into the strong-field non-linear regime.

A polarisation dependence of the results is also observed. Whilst the peak values of PES features occur at roughly the same kinetic energies for both polarisations, for s-polarised light it can be seen that the tail of ‘fast’ electrons extends to much higher kinetic energies (80 eV as compared to 45 eV for p-polarised light). The threshold laser intensities at which the electrons are observed is also lower for s-polarised light. For p-polarised light the kinetic energies of electrons measured match up with nonlinearity estimates. Initial and final states on the graphite band structure at the M-point and Γ -point of the graphite lattice have been identified which would lead to photoelectrons with kinetic energies either within or lying just outside of the uncertainty range of the experimental values measured. The phenomenon can therefore be explained by high-order multi-photon excitation. For s-polarisation this is not the case so it is speculatively suggested that either tunnel ionisation or thermal effects may also play a part in the excitation process. Literature searches have revealed that surface plasmons and field enhancement

can occur at the HOPG surface which is not widely reported. Taking into account sensible estimates for field enhancement suggest that experimental parameters lie in the multiphoton regime but close to the Keldysh limit for tunnelling. This supports the mechanism suggested for p-polarised light and the ambiguity surrounding s-polarised light. The apparent preference for s-polarised light might suggest the presence of localised surface plasmons. It would be interesting to extend this work by performing similar experiments on a purposely structured surface i.e. a grating so that plasmon effects and therefore field enhancement could be manipulated.

6.2 Chapter 4 Conclusion: Interferometric Measurements and Optical Bloch Simulations of Photoelectron Emission from the HOPG Surface

In Chapter 4 time-resolved measurements of the photoemission signal from the HOPG surface were presented.

Interferometric autocorrelation of the photoemission signal generated by 13 fs infra red pulses showed that the excitation process is coherent and that the fast electrons are generated at the surface. The autocorrelation trace showed signatures of the nonlinearities involved as both the trace envelope and the width of individual fringes were observed to decrease with increasing photoelectron kinetic energies. This autocorrelation shape was successfully modelled using the Optical Bloch Equations where it was shown that the standard OBE's could be modified to describe a resonant multiphoton transition. At the high non-linearities involved in the excitation it was shown that the number of photons was the dominant factor

for the shape of the autocorrelation trace. Little effect was seen from the lifetime of the excited state or the detuning of the system.

IR pump-XUV probe measurements were also made at the HOPG surface. It was shown that a conduction band state lying below the vacuum level could be excited by the IR pulse and probed using XUV pulse trains. Unfortunately low signal levels and problems with laser drift meant that the data retrieved was not of high enough quality to perform a proper quantitative analysis however a qualitative discussion of the data and comparisons between the data and simulations suggest a 3-photon excitation of a conduction band state below the vacuum level. The challenging experimental method has been described in detail along with technical difficulties that were overcome such as interference in the gas jet resulting in modulation of the signal intensity. No attosecond measurements were achieved at the surface, due principally to the inability to isolate single attosecond pulses but also due to low signal levels. Potential improvements that could be made to the beamline to improve data collection include a feedback loop to correct for beam drift and a replacement of key optics to improve poor transmission efficiency along the beam line.

6.3 Chapter 5 Conclusion: Velocity Map Imaging of the HOPG Surface

Outside of the collaborative research that forms the core of this thesis, Velocity Map Imaging has been demonstrated for the first time from a solid surface. It has been shown both experimentally and by simulations that by the careful application of electrostatic potentials it is possible to image the photoelectron emission from a surface such that any electrons leaving the surface with identical velocity vectors will be imaged at a single point on an imaging detector plate.

Initial tests on the HOPG surface suggest that photoelectrons leave the surface at angles of up to 40 degrees from the normal. These initial tests also revealed that the VMI technique suffers from poor time resolution due to the time response of the MCP and the phosphorous screen. This lack of resolution prevented the separate imaging of photoelectrons with different kinetic energies however by comparison to data taken in Chapter 3 it seems likely that the main contribution to the photoelectron signal came from photoelectrons with low kinetic energies of around 1 eV.

6.4 Continuation of Work and Future Plans

The work presented in this thesis has concentrated on the interaction of few-cycle laser pulses and attosecond pulse trains at surfaces. Unfortunately measurements on an attosecond timescale were not achieved at the surface however significant experimental difficulties were overcome and others have been identified. During the course of these experiments being carried out the first (and so far the only) demonstration of attosecond measurements in condensed matter has been published by Cavalieri et al. [10], from the well established attosecond group headed by Prof. Ferenc Krausz. The slow overall progress in the research area highlights the technical difficulties involved in such experiments.

Whilst the collaborative research period has now ended many lessons have been learned by both sides which can now be taken forward independently. The laboratory in NPRL, Birmingham have now purchased a new laser which outputs 30 fs IR pulses and it is planned that hollow fibre compression techniques will be used to achieve few-cycle pulses. The pulses could be used along an existing HHG beamline to generate attosecond pulses for surface experiments. The fast count ToF used for the work in Chapter 3 and 4 and the VMI detector used in Chapter 5 can be used on the same system, one to provide directional information and one

to provide time resolved information although they cannot be operated simultaneously. It is planned that the new system can be used to further investigate the role that surface plasmons play in electron acceleration. Using a purpose built grating to couple plasmon polaritons to a surface it will be possible to control the interaction and to investigate the photoelectrons emitted both with high time resolution and also angular resolution.

The group at Imperial College are also planning to continue working on attosecond measurements at surfaces and have designed and built a new surface science chamber of their own, drawing on experience gained working with the Birmingham Surface Science Chamber; the complexity of the chamber used in this thesis was above that required for simple surface experiments yet sample transfer and vacuum management consumed valuable experimental time. As a result of the collaborative research efforts both groups are now in a position to study surface dynamics on few-cycle timescales.

Appendix A

Derivation of the Dispersion

Parameter, β and the Polarisation

Conditions of a Surface Plasmon

Polariton at a Metal/Dielectric

Interface

Surface plasmon polaritons at a metal/dielectric interface such as that shown in Fig 2.8 (a) can be described mathematically (derivation followed from [46]) starting from Maxwell's equations (A.1)-(A.4):

$$\nabla \cdot \mathbf{D} = \rho_{ext} \quad (\text{A.1})$$

$$\nabla \cdot \mathbf{B} = 0 \quad (\text{A.2})$$

$$\nabla \times \mathbf{E} = -\frac{\partial \mathbf{B}}{\partial t} \quad (\text{A.3})$$

$$\nabla \times \mathbf{H} = \mathbf{J}_{\text{ext}} + \frac{\partial \mathbf{D}}{\partial t} \quad (\text{A.4})$$

and the wave equation (A.5):

$$\frac{\partial^2 \mathbf{E}}{\partial z^2} + (k_0^2 \epsilon - \beta^2) \mathbf{E} = 0 \quad (\text{A.5})$$

Where \mathbf{E} is the electric field, \mathbf{H} is the magnetic field, \mathbf{D} is the dielectric displacement and \mathbf{B} is the magnetic flux density. β is propagation constant, the component of the wavevector acting in the direction of propagation.

If $\frac{\partial}{\partial t} = -i\omega$ is assumed then (A.3) and (A.4) can be solved to give equations for electric and magnetic field components in the x, y and z directions:

$$\frac{\partial E_z}{\partial y} - \frac{\partial E_y}{\partial z} = i\omega\mu_0 H_x \quad (\text{A.6})$$

$$\frac{\partial E_x}{\partial z} - \frac{\partial E_z}{\partial x} = i\omega\mu_0 H_y \quad (\text{A.7})$$

$$\frac{\partial E_y}{\partial x} - \frac{\partial E_x}{\partial y} = i\omega\mu_0 H_z \quad (\text{A.8})$$

$$\frac{\partial H_z}{\partial y} - \frac{\partial H_y}{\partial z} = -i\omega\epsilon_0 \epsilon E_x \quad (\text{A.9})$$

$$\frac{\partial H_x}{\partial z} - \frac{\partial H_z}{\partial x} = -i\omega\epsilon_0 \epsilon E_y \quad (\text{A.10})$$

$$\frac{\partial H_y}{\partial x} - \frac{\partial H_x}{\partial y} = -i\omega\epsilon_0 \epsilon E_z \quad (\text{A.11})$$

This can be simplified for the case that propagation is in the x-direction and the fields are homogeneous in the y-direction ($(\frac{\partial}{\partial x} = i\beta)$ and $(\frac{\partial}{\partial y} = 0)$) to give:

$$\frac{\partial E_y}{\partial z} = -i\omega\mu_0 H_x \quad (\text{A.12})$$

$$\frac{\partial E_x}{\partial z} - i\beta E_z = -i\omega\mu_0 H_y \quad (\text{A.13})$$

$$i\beta E_y = -i\omega\mu_0 H_z \quad (\text{A.14})$$

$$\frac{\partial H_y}{\partial z} = i\omega\epsilon_0\epsilon E_x \quad (\text{A.15})$$

$$\frac{\partial H_x}{\partial z} - i\beta H_z = -i\omega\epsilon_0\epsilon E_y \quad (\text{A.16})$$

$$i\beta H_y = -i\omega\epsilon_0\epsilon E_z \quad (\text{A.17})$$

For TM modes (p-polarisation) only the components E_x , E_z and H_y are not equal to zero so that the situation can be described by two governing equations (A.18) and (A.19) and the wave equation(A.20):

$$E_x = -i\frac{1}{\omega\epsilon_0\epsilon} \frac{\partial H_y}{\partial z} \quad (\text{A.18})$$

$$E_z = -\frac{\beta}{\omega\epsilon_0\epsilon} H_y \quad (\text{A.19})$$

$$\frac{\partial^2 H_y}{\partial z^2} + (k_0^2\epsilon - \beta^2)H_y = 0 \quad (\text{A.20})$$

These can be solved for the separate cases of above and below the interface where $z > 0$ corresponds to the dielectric insulating material with a real positive dielectric constant of ϵ_2 and $z < 0$ to the metal with a dielectric constant of $\epsilon_1(\omega)$ where $\Re[\epsilon_1(\omega)] < 0$. A_1 and A_2 are coefficients.

At $z > 0$:

$$H_y(z) = A_2 e^{i\beta x} e^{-k_2 z} \quad (\text{A.21})$$

$$E_x(z) = iA_2 \frac{1}{\omega\epsilon_0\epsilon_2} k_2 e^{i\beta x} e^{-k_2 z} \quad (\text{A.22})$$

$$E_z(z) = -A_2 \frac{\beta}{\omega\epsilon_0\epsilon_2} e^{i\beta x} e^{-k_2 z} \quad (\text{A.23})$$

And for $z < 0$:

$$H_y(z) = A_1 e^{i\beta x} e^{k_1 z} \quad (\text{A.24})$$

$$E_x(z) = -iA_1 \frac{1}{\omega \epsilon_0 \epsilon_1} k_1 e^{i\beta x} e^{k_1 z} \quad (\text{A.25})$$

$$E_z(z) = -A_1 \frac{\beta}{\omega \epsilon_0 \epsilon_1} e^{i\beta x} e^{k_1 z} \quad (\text{A.26})$$

k_1 and k_2 are the components of the wave vector perpendicular to the interface for the metal and dielectric respectively. $1/k_i$ is the decay length of the evanescent field into either medium (i.e. $i = 1,2$).

From (A.21)-(A.23) and satisfying continuity of H_y and $\epsilon_i E_z$ at the interface it is required that $A_1 = A_2$ and that:

$$\frac{k_2}{k_1} = -\frac{\epsilon_2}{\epsilon_1} \quad (\text{A.27})$$

Confinement of the wave at the surface requires that $\Re[\epsilon_1] < 0$ and $\epsilon_2 > 0$. Also, since A.21 and A.24 have to satisfy A.20 then:

$$k_1^2 = \beta^2 - k_0^2 \epsilon_1 \quad (\text{A.28})$$

$$k_2^2 = \beta^2 - k_0^2 \epsilon_2 \quad (\text{A.29})$$

which, when combined gives the dispersion relation:

$$\beta = k_0 \left(\frac{\epsilon_1 \epsilon_2}{\epsilon_1 + \epsilon_2} \right)^{1/2} = k_{SP} \quad (\text{A.30})$$

where $k_0 = \frac{\omega}{c}$.

The same derivation can be applied for the TE case; the governing equations and wave equation are given by:

$$H_x = i \frac{1}{\omega \mu_0} \frac{\partial E_y}{\partial z} \quad (\text{A.31})$$

$$H_z = -\frac{\beta}{\omega \mu_0} E_y \quad (\text{A.32})$$

$$\frac{\partial^2 E_y}{\partial z^2} + (k_0^2 \epsilon - \beta^2) E_y = 0 \quad (\text{A.33})$$

so that the field components are given by:

$$E_y(z) = A_2 e^{i\beta x} e^{-k_2 z} \quad (\text{A.34})$$

$$H_x(z) = -i A_2 \frac{1}{\omega \mu_0} k_2 e^{i\beta x} e^{-k_2 z} \quad (\text{A.35})$$

$$H_z(z) = -A_2 \frac{\beta}{\omega \mu_0} e^{i\beta x} e^{-k_2 z} \quad (\text{A.36})$$

$z > 0$ and

$$E_y(z) = A_1 e^{i\beta x} e^{k_1 z} \quad (\text{A.37})$$

$$H_x(z) = i A_1 \frac{1}{\omega \mu_0} k_1 e^{i\beta x} e^{k_1 z} \quad (\text{A.38})$$

$$H_z(z) = -A_1 \frac{\beta}{\omega \mu_0} e^{i\beta x} e^{k_1 z} \quad (\text{A.39})$$

for $z < 0$

In this case, continuity of E_y and H_x give the condition:

$$A_1(k_1 + k_2 = 0) \quad (\text{A.40})$$

This condition is only true if $A_1 = A_2 = 0$ since confinement to the surface means that $\Re[k_1] > 0$ and $\Re[k_2] > 0$. Surface plasmon polariton modes do therefore not exist for TE modes so can be excited only for the TM case (by p-polarised light).

Appendix B

Second Harmonic Generation (SHG)

In a non-linear optical medium (Such as a BBO crystal) the polarisation P^{NL} induced by an electric field E is given by:

$$P^{NL} = 2\epsilon_0 d E^2 \quad (\text{B.1})$$

where d is the nonlinear optical coefficient.

If the electric field is defined as:

$$E_\omega(z, t) = \frac{1}{2} E(z, \omega) \{ \exp[i(\omega t - k_\omega z)] + \exp[i(k_\omega z - \omega t)] \} \quad (\text{B.2})$$

where

$$k_\omega = \frac{n_\omega \omega}{c} \quad (\text{B.3})$$

then the polarisation induced by the field as it travels through the medium can be given by:

$$P_{\omega}^{NL}(z, t) = \frac{\epsilon_0 d}{2} E(z, \omega) \{ \exp[i(2\omega t - 2k_{\omega} z)] + \exp[i(2k_{\omega} z - 2\omega t)] \} \quad (\text{B.4})$$

The oscillation of this polarisation wave at a frequency of 2ω will then generate an electromagnetic wave also oscillating at 2ω , given as:

$$E_{2\omega}(z, t) = \frac{1}{2} E(z, 2\omega) \{ \exp[i(2\omega t - k_{2\omega} z)] + \exp[i(k_{2\omega} z - 2\omega t)] \} \quad (\text{B.5})$$

where

$$k_{2\omega} = \frac{n_{2\omega} \omega}{c} \quad (\text{B.6})$$

The process of second harmonic generation will occur at any point along the length of the crystal however for the most efficient yield of the second harmonic at the exit of the crystal can be obtained if the individual SHG contributions are added together constructively such that they grow cumulatively with increasing distance travelled. In order for this to occur the phase velocity of the polarisation wave must be equal to the phase velocity of the second harmonic generated:

$$\frac{2\omega}{2k_{\omega}} = \frac{2\omega}{k_{2\omega}} \quad (\text{B.7})$$

i.e. $k_{2\omega} = 2k_{\omega}$. Using equations (B.4) and (B.7) this can be expressed simply as:

$$n_{2\omega} = n_{\omega} \quad (\text{B.8})$$

This is known as the “phase matching condition” and for a birefringent crystal can be achieved either by the orientation of the crystal or by its temperature.

Appendix C

Estimating the Uncertainty of Experimental Measurements

C.1 Kinetic Energy of Electrons using Time of Flight Mass Spectrometry

The Kinetic Energy, E_K of an electron when it leaves the surface can be described by the following equation:

$$E_K = \frac{m_e}{2} \left(\frac{L}{t} \right)^2 - E_{acc} \quad (\text{C.1})$$

where m_e is the mass of the electron, L is the distance travelled by the electron, t is the time taken for the electron to travel from the surface to the detector and E_{acc} is the kinetic energy gained by the electron before it enters the ToF.

This acceleration energy is generated by the potentials difference applied between the lens of the ToF and the sample. The mean potential applied to the lens was +5.86 V and the mean potential applied to the sample was -1.81V. Both of these

could be measured with an accuracy of ± 0.01 V. This gives an average acceleration energy of 7.66 ± 0.02 eV.

With respect to the ToF spectrometer, it can be seen from the left hand side of Equation C.1 that uncertainty can come from the measurements of L and t . The drift tube was 1 m long and the lens/sample separation was 4mm. The separation distance was measured with a micrometer screw gauge however the flight path within the ToF could be measured with an accuracy of 1mm. The measurement of flight path, L is therefore given by 1.004 ± 0.001 m. In measuring t , the most significant error came from the preamplifier of the MCP. This was specially chosen for its fast reaction and had an uncertainty of ± 1.5 nanoseconds. The electrons observed with the shortest time of flight (i.e. those with the highest energy) had a peak value of 0.25μ s, corresponding to a percentage error of 0.6%.

Thus, the error on the tof measurement (left hand) can be given by:

$$\left(\frac{\delta E_K}{|E_K|}\right)^2 = \left(2\frac{\delta L}{|L|}\right)^2 + \left(2\frac{\delta t}{|t|}\right)^2 \quad (\text{C.2})$$

$$\frac{\delta E_K}{|E_K|} = \sqrt{4\left(\left(\frac{\delta L}{|L|}\right)^2 + \left(\frac{\delta t}{|t|}\right)^2\right)} \quad (\text{C.3})$$

Substituting in the values of the previous paragraphs gives a value of 0.012 for $\frac{\delta E_K}{|E_K|}$ i.e a percentage error of 1.2% which is the most significant uncertainty of the kinetic energy measurements.

This works out as a very small error in the measurement of “slow” electrons, for example the experimental error as calculated above is only ± 0.0036 eV for the 0.3 “slow peak” in the photoelectron spectrum taken with p-polarised IR light. This should be expected due to the fine temporal resolution of the ToF detector.

For the measurements of key interest, the “fast” electrons, the estimates detailed above give measurements for the peak values of 26.0 ± 0.3 eV and 28.0 ± 0.3 eV

for p- and s-polarisations respectively. However, since it is not believed that the “peak” of each electron feature could be measured more accurately than to the nearest 0.5 eV, the errors on the kinetic energy measurements have been quoted throughout the thesis as ± 0.5 eV. Where errors have not been quoted it should be assumed that an error of ± 0.5 eV applies.

C.2 Laser Intensity Measurements

The intensity, I in W/cm^2 of a laser pulse is given by:

$$I = \frac{E}{A \times t_p} \quad (\text{C.4})$$

where E is the energy measured in J, A is the area of the spot size (in cm^2) and t_p is the pulse duration (in seconds).

Since all components of Equation C.4 introduce some uncertainty, the standard error calculation for the laser intensity measurements can be given by:

$$\left(\frac{\delta I}{|I|}\right)^2 = \left(\frac{\delta E}{|E|}\right)^2 + \left(\frac{\delta A}{|A|}\right)^2 + \left(\frac{\delta t_p}{|t_p|}\right)^2 \quad (\text{C.5})$$

Over the range of laser intensities used, the mean of the energy measurements $|E|$ is $45 \mu\text{J}$ with an error, taken from the power meter, of ± 1 J (these energy measurements have been directly taken from the power readings in mW which has the same value as the energy in μJ since the repetition rate is 1KHz).

The spot size diameter, d , was measured as $325.1 \pm 0.1 \mu\text{m}$. The pulse duration was measured by FROG to be 13 fs with an accuracy of ± 0.5 fs. Substituting these numbers into Equation C.5 gave a value of 0.04 (4%) for $\frac{\delta I}{|I|}$. This uncertainty

estimate was used in plot 3.16 to generate error bars to show the uncertainty of the intensity measurements.

References

- [1] R. E. Carley, E. Heesel, and H. H. Fielding. Femtosecond lasers in gas phase chemistry. *Chem. Soc. Rev.*, 34:949–969, 2005.
- [2] September 2009. URL <http://nobelprize.org>.
- [3] Pierre Agostini and Louis F. DiMauro. The physics of attosecond light pulses. *Reports on Progress in Physics*, 67:813–855, 2004.
- [4] P. B. Corkum. Plasma perspective on strong field multiphoton ionization. *Physical Review Letters*, 71(13):1994–1997, 1993.
- [5] F. Krausz and M. Ivanov. Attosecond physics. *Rev. Mod. Phys.*, 81:163–234, 2009.
- [6] T. Brabec and F. Krausz. Intense few-cycle laser fields. *Reviews of Modern Physics*, 72(2):545, 2000.
- [7] P. B. Corkum and F. Krausz. Attosecond science. *Nature Physics*, 3:381–387, 2007.
- [8] M. Drescher, M. Hentschel, R. Kienberger, M. Uiberacker, V. Yakovlev, A. Scrinzi, Th. Westerwalbesloh, U. Kleineberg, U. Heinzmann, and F. Krausz. Time-resolved atomic inner-shell spectroscopy. *Nature*, 419: 803–807, 2002.
- [9] E. Goulielmakis and. Direct measurement of light waves. *Science*, 305: 1267–1269, 2004.

-
- [10] A. L. Cavalieri, N. Muller, Th. Uphues, V. S. Yakovlev, A. Baltuska, B. Horvath, B. Schmidt, L. Blumel, R. Holzwarth, S. Hendel, M. Drescher, U. Kleineberg, P. M. Echenique, R. Kienberger, F. Krausz, and U. Heinzmann. Attosecond spectroscopy in condensed matter. *Nature*, 449(06229): 1029–1032, 2007.
- [11] C.-H. Zhang and U. Thumm. Attosecond photoelectron spectroscopy of metal surfaces. *Phys. Rev. Lett.*, 102(123601), 2009.
- [12] J-C. Diels and W. Rudolph. *Ultrashort Laser Pulse Phenomena*. Academic Press, 1995.
- [13] F. Träger, editor. *Springer Handbook of Lasers and Optics*. Springer, 2007.
- [14] C. Ruilliere. *Femtosecond Laser Pulses: Principles and Experiments*. Springer Science, 2003.
- [15] R. Paschotta. *Encyclopedia of Laser Physics and Technology*. Wiley-VCH, Berlin, 2008.
- [16] C. Ruilliere. *Femtosecond Laser Pulses: Principles and Experiments*. Springer Science, 2003.
- [17] S. E. Irvine, P. Dombi, Gy. Farkas, and A. Y. Elezzabi. Influence of the carrier-envelope phase of few-cycle pulses on ponderomotive surface-plasmon electron acceleration. *Physical Review Letters*, 97(146801), 2006.
- [18] Dr John Tisch. Calculations and private communications. *Imperial College London*, 2007.
- [19] Eric Mevel, Pierre Breger, Rusty Trainham, Guillaume Petite, Pierre Agostini, Arnold Migus, Jean-Paul Chambaret, and Andre Antonetti. Atoms in strong optical fields: Evolution from multiphoton to tunnel ionization. *Phys. Rev. Lett.*, 70(4):406–409, 1993.

- [20] L. V. Keldysh. unknown. *Soviet Physics JETP*, 20:1307, 1965.
- [21] Popov V. S. Tunnel and multiphoton ionisation of atoms and ions in a strong laser field (keldysh theory). *Reviews of Topical Problems*, 47(9):855–885, 2004.
- [22] G. Ferrini, F. Banfi, C. Giannetti, and F. Parmigiani. Non-linear electron photoemission from metals with ultrashort pulses. *Nuclear Instruments and Methods in Physics Research A*, 601:123–131, 2009.
- [23] F. H. M. Faisal and G. Schlegel. Signatures of photon effect in the tunnel regime. *Journal of Physics B*, 38:L223–L231, 2005.
- [24] M. Bauer. Femtosecond ultraviolet photoelectron spectroscopy of ultra-fast surface processes. *Journal of Physics D: Applied Physics*, 38:R253–R267, 2005.
- [25] E. Zubritsky. Xps up close. *Anal. Chem.*, 73(9):279 A–283 A, 2001.
- [26] H. Petek and S. Ogawa. Femtosecond time-resolved two-photon photoemission studies of electron dynamics in metals. *Progress in Surface Science*, 56(4):239–310, 1997.
- [27] M. Weinelt. Time-resolved two-photon photoemission from metal surfaces. *J. Phys.:Condens. Matter*, 14:R1099–R1141, 2002.
- [28] H. Ueba and B. Gumhalter. Theory of two-photon photoemission spectroscopy of surfaces. *Progress in Surface Science*, 82:193–223, 2007.
- [29] J. Lehmann, M. Merschdorf, A. Thon, S. Voll, and W. Pfeiffer. Properties and dynamics of the image potential states on graphite investigated by multiphoton photoemission spectroscopy. *Physical Review B*, 60(24):17037, 1999.

- [30] T. Hertel, E. Knoesel, A. Hotzel, M. Wolf, and G. Ertl. Femtosecond time-resolved photoemission of electron dynamics in surface rydberg states. *J. Vac. Sci. Technol. A*, 15(3):1503, 1997.
- [31] T. Hertel, E. Knoesel, M. Wolf, and G. Ertl. Ultrafast electron dynamics at cu(111):response of an electron gas to optical excitation. *Physical Review Letters*, 76(3):535, 1996.
- [32] S. Xu, J. Cao, C. C. Miller, D. A. Mantell, R. J. D. Miller, and Y. Gao. Energy dependence of electron lifetime in graphite observed with femtosecond photoemission spectroscopy. *Phys. Rev. Lett.*, 76(3):483–486, 1996.
- [33] U. Hofer, I. L. Shumay, Ch. Reuss, U. Thomann, W. Wallauer, and Th. Fauster. Time-resolved coherent photoelectron spectroscopy of quantized electronic states on metal surfaces. *Science*, 277:1480, September 1997.
- [34] S. Ogawa, H. Nagano, H. Petek, and A. P. Heberle. Optical dephasing in cu(111) measured by interferometric two-photon time-resolved photoemission. *Physical Review Letters*, 78(7):1339, 1997.
- [35] D. Velic, A. Hotzel, M. Wolf, and G. Ertl. Electronic states of the c6hc/cu111 system: Energetics, femtosecond dynamics and adsorption morphology. *Journal of Chemical Physics*, 109(20):9155, 1998.
- [36] K. Boger, M. Roth, M. Weinelf, T. Fauster, and P-G Reinhard. Linewidths in energy-resolved two-photon photoemission spectroscopy. *Physical Review B*, 65(075104), 2002.
- [37] T. Mii H. Ueba. Theory of energy and time resolved two photon photoemission from metal surfaces - influence of pulse duration and excitation condition. *Applied Physics A*, 71:537–545, 2000.
- [38] W. L. Barnes, A. Dereau, and T. W. Ebbesen. Surface plasmon subwavelength optics. *Nature*, 424:824–830, 2003.

- [39] H. Raether. *Surface Plasmons on Smooth and Rough Surfaces and on Gratings*(*Springer Tracts in Modern Physics*). Springer, 1988.
- [40] S. E. Irvine and A. Y. Elezzabi. Ponderomotive electron acceleration using surface plasmon waves excited with femtosecond laser pulses. *Applied Physics Letters*, 86(264102), 2005.
- [41] J. Kupersztych, P. Monchicourt, and M. Raynaud. Ponderomotive acceleration of photoelectrons in surface-plasmon-assisted multiphoton photoelectric emission. *Physical Review Letters*, 86(22):5180–5183, 2001.
- [42] W. H. Weber and G. W. Ford. Optical electric-field enhancement at a metal surface arising from surface-plasmon excitation. *Optics Letters*, 6(3):122–124, 1981.
- [43] M. Huang, F. Zhao, Y. Cheng, N. Xu, and Z. Xu. Mechanisms of ultrafast laser-induced deep-subwavelength gratings on graphite and diamond. *Phys. Rev. B*, 79(125436), 2009.
- [44] S. Kim, J. Jin, Y-J Kim, I-Y Park, Y Kim, and S-W Kim. High-harmonic generation by resonant plasmon field enhancement. *Nature*, 453:757–760, 2008.
- [45] N. Kroo, Gy. Farkas, P. Dombi, and S. Varro. Nonlinear processes induced by the enhanced, evanescent field of surface plasmons excited by femtosecond laser pulses. *Optics Express*, 16(26):21656–21661, December 2008.
- [46] S. A. Maier. *Plasmonics: Fundamentals and Applications*. Springer, 2007.
- [47] K. Kim. Excitation of s-polarised surface electromagnetic waves in homogeneous dielectric media. *Optics Express*, 16(17):13354–13363, 2008.
- [48] R.-L. Chern and Y.-C.-Lan. Collective modes in metallic photonic crystals with subwavelength grooves. *Phys. Rev. B*, 80:033107, 2009.

- [49] O. Schmidt, G. H. Fecher, Y. Hwu, and G. Schönhense. The spatial distribution of non-linear effects in multiphoton photoemission from metallic adsorbates on si(111). *Surface Science*, 482-485:687–692, 2001.
- [50] M. Aeschlimann, C. A. Schmuttenmaer, H. E. Elsayed-Ali, R. J. D. Miller, J. Cao, Y. Gao, and D. A. Mantell. Observation of surface enhanced multiphoton photoemission from metal surfaces in the short pulse limit. *Journal of Chemical Physics*, 102(21):8606–8612, 1995.
- [51] N. Georgiev, D. Martinotti, and H.-J. Ernst. Enhanced photoemission from localized inhomogeneities on cu(001) characterized by laser-assisted photoemission electron microscopy and low-energy electron microscopy. *Phys. Rev. B*, 75(8):085430, 2007.
- [52] G. H. Fecher, O. Schmidt, Y. Hwu, and G. Schönhense. Multiphoton photoemission electron microscopy using femtosecond laser radiation. *J. Elec. Spec. Rel. Phenom.*, 126:77–87, 2002.
- [53] V. Shalaev, C. Douketis, T. Haslett, T. Stuckless, and M. Moskovits. Two-photon electron emission from smooth and rough metal films in the threshold region. *Phys. Rev. B*, 53(16):11193–11206, 1996.
- [54] M. I. Stockman. Femtosecond optical responses of disordered clusters, composites, and rough surfaces: “the ninth wave” effect. *Phys. Rev. Lett.*, 84(5):1011–1014, 2000.
- [55] C. Roopers, D. R. Solli, C. P. Schulz, C. Lienau, and T. Elsaesser. Localized multiphoton emission of femtosecond electron pulses from metal nanotips. *Phys. Rev. Lett.*, 98(043907), 2007.
- [56] Peter Hommelhoff, Catherine Kealhofer, and Mark A. Kasevich. Ultrafast electron pulses from a tungsten tip triggered by low-power femtosecond laser pulses. *Phys. Rev. Lett.*, 97(247402), 2006.

- [57] Bradley J. Siwick, Jason R. Dwyer, Robert E. Jordan, and R. J. D. Miller. An atomic-level view of melting using femtosecond electron diffraction. *Science*, 302(1382), 2003.
- [58] S. E. Irvine, A. Dechant, and A. Y. Elezzabi. Generation of 0.4 keV femtosecond electron pulses using impulsively excited surface plasmons. *Physical Review Letters*, 93(18):184801, 2004.
- [59] A. Belsky, P. Martin, H. Bachau, A. N. Vasil'ev, B. N. Yatsenko, S. Guizard, G. Geoffroy, and G. Petite. Heating of conduction band electrons by intense femtosecond laser pulses. *Europhysics Letters*, 67(2):301–306, 2004.
- [60] G. Petite, P. Agostini, R. Trainham, E. Mevel, and P. Martin. Origin of the high-energy electron emission from metals under laser irradiation. *Physical Review B*, 45(21):12210, 1992.
- [61] Gy. Farkas and Cs. Tóth. Energy spectrum of photoelectrons produced by picosecond laser-induced surface multiphoton photoeffect. *Phys. Rev. A*, 41(7):4123–4126, 1990.
- [62] GianPiero Banfi, Gabriele Ferrini, Marco Peloi, and Fulvio Parmigiani. Anomalous photoemission from Ag(100) in the femtosecond regime. *Phys. Rev. B*, 67(3):035428, Jan 2003. doi: 10.1103/PhysRevB.67.035428.
- [63] Peifen Lu, Jian Wu, Honxing Qi, and Heping Zeng. Ponderomotive electron acceleration by polarization-gated surface-enhanced optical fields. *Applied Physics Letters*, 93(201108), 2008.
- [64] D. M. Riffe, X. Y. Wang, M. C. Downer, D. L. Fisher, T. Tajima, J. L. Erskine, and R. M. More. Femtosecond thermionic emission from metals in the space-charge-limited regime. *J. Opt. Soc. Am. B*, 10(8):1424–1435, 1993.
- [65] A. N. Belsky, H. Bachau, J. Gaudin, G. Geoffroy, S. Guizard, P. Martin, G. Petite, A. Philippov, A. N. Vasil'ev, and B. N. Yatsenko. Observation

- of high energy photoelectrons from solids at moderate laser intensity. *Appl. Phys. B*, 78:989–994, 2004.
- [66] M. Nisoli, S. De Silvestri, and O. Svelto. Generation of high energy 10fs pulses by a new pulse compression technique. *Applied Physics Letters*, 68(20):2793, 1996.
- [67] S. E. Harris and A. V. Sokolov. Subfemtosecond pulse generation by molecular modulation. *Phys. Rev. Lett.*, 81(14):2894–2897, 1998.
- [68] A. Baltuska, Th. Udem, M. Uiberacker, M. Hentschel, E. Goulielmakis, Ch. Gohle, R. Holzwarth, V. S. Yakovlev, A. Scrinzi, T. W. Hänsch, and F. Krausz. Attosecond control of electronic processes by intense light fields. *Nature*, 421:611–616, 2003.
- [69] P. M. Paul, E. S. Toma, P. Breger, G. Mullot, F. Audebert, Ph. Balcou, H. G. Muller, and P. Agostini. Observation of a train of attosecond pulses from high harmonic generation. *Science*, 292:1689–1692, 2001.
- [70] R. Lopez-Martens, K. Varju, P. Johnsson, J. Mauritsson, Y. Mairesse, P. Salieres, M. B. Gaarde, K. J. Schafer, A. Persson, S. Svanberg, C-G. Wahlstrom, and A. L’Huillier. Amplitude and phase control of attosecond light pulses. *Phys. Rev. Lett.*, 94(033001), 2005.
- [71] N. Dudovich, O. Smirnova, J. Levesque, Y. Mairesse, M. Yu. Ivanov, D. M. Villeneuve, and P. B. Corkum. Measuring and controlling the birth of attosecond xuv pulses. *Nature Physics*, 2:781–786, 2006.
- [72] R. Kienberger, E. Goulielmakis, M. Uiberacker, A. Baltuska, V. Yakovlev, F. Bammer, A. Scrinzi, Th. Westerwalbesloh, U. Kleineberg, U. Heinzmann, M. Drescher, and F. Krausz. Atomic transient recorder. *Nature*, 427:817–821, 2004.

- [73] I. Christov, M. M. Murnane, and H. C. Kapteyn. High-harmonic generation of attosecond pulses in the “single-cycle” regime. *Phys. Rev. Lett.*, 78(7):1251–1254, 1997.
- [74] I. J. Sola, E. Mevel, L. Elouga, E. Constant, V. Strelkov, L. Poletto, P. Villoresi, E. Benedetti, J.-P. Caumes, S. Stagira, C. Vozzi, G. Sansone, and M. Nisoli. Controlling attosecond electron dynamics by phase-stabilized polarisation gating. *Nature Physics*, 2(5):319–322, 2006.
- [75] G. Sansone, E. Benedetti, F. Calegari, C. Vozzi, L. Avaldi, R. Flammini, L. Poletto, P. Villoresi, C. Altucci, R. Velotta, S. Stagira, S. De Silvestri, and M. Nisoli. Isolated single-cycle attosecond pulses. *Science*, 314:443–446, 2006.
- [76] E. Goulielmakis, V. S. Yakovlev, A. L. Cavalieri, M. Uiberacker, V. Pervak, A. Apolonski, R. Kienberger, U. Kleineberg, and F. Krausz. Attosecond control and measurement: Lightwave electronics. *Science*, 317:769–775, 2007.
- [77] M. Uiberacker, Th. Uphues, M. Schultze, A. J. Verhoef, V. Yakovlev, M. F. Kling, J. Rauschenberger, N. M. Kabachnik, H. Schröder, M. Lezius, K. L. Kompa, H. G. Muller, M. J. J. Vrakking, S. Hendel, U. Kleineberg, U. Heinzmann, M. Drescher, and F. Krausz. Attosecond real-time observation of electron tunnelling in atoms. *Nature*, 446(05648):627–632, 2007.
- [78] M. I. Stockman, M. F. Kling, U. Kleineberg, and F. Krausz. Attosecond nanoplasmonic-field microscope. *Nature Photonics*, 1:539–544, 2007.
- [79] R. Horlein, Y. Nomura, J. Osterhoff, Zs. Major, S. Karsch, F. Krausz, and G. D. Tsakiris. High harmonics from solid surfaces as a source of ultra-bright xuv radiation for experiments. *Plasma Physics and Controlled Fusion*, 50(124002), 2008.

-
- [80] F. H. M. Faisal, J. Z. Kaminski, and E. Saczuk. Photoemission and high-order harmonic generation from solid surfaces in intense laser fields. *Phys. Rev. A*, 72(2):023412, 2005.
- [81] M. J. Weida, S. Ogawa, H. Nagano, and H. Petek. Parallel excitation pathways in ultrafast interferometric pump-probe correlation measurements of hot-electron lifetimes in metals. *Appl. Phys. A*, 71:553–559, 2000.
- [82] M. Skibowski I. Schafer, M. Schluter. Conduction band structure of graphite studied by combined angle resolved inverse photoemission and target current spectroscopy. *Physical Review B*, 35(14):7663, 1987.
- [83] A. R. Law, M. T. Johnson, and H. P. Hughes. Synchrotron-radiation-excited angle-resolved photoemission from single-crystal graphite. *Phys. Rev. B*, 34(6):4289–4297, 1986.
- [84] Editorial. Graphene calling. *Nature Materials*, 6(3):169, March 2007.
- [85] A. K. Geim and K. S. Novoselov. The rise of graphene. *Nature Materials*, 6:183–191, March 2007.
- [86] A. G. Marinopoulos, Lucia Reining, Angel Rubio, and Valerio Olevano. Ab initio study of the optical absorption and wave-vector-dependent dielectric response of graphite. *Phys. Rev. B*, 69(24):245419, 2004.
- [87] R. C. Tatar and S. Rabii. Electronic properties of graphite: A unified theoretical study. *Physical Review B*, 25(6), 1982.
- [88] R. Claessen, H. Carstensen, and M. Skibowski. Conduction-band structure of graphite single crystals studied by angle-resolved inverse photoemission and target-current spectroscopy. *Phys. Rev. B*, 38(17), 1988.
- [89] G. S. Painter and D. E. Ellis. Electronic band structure and optical properties of graphite from a variational approach. *Phys. Rev. B*, 1(12):4747–4752, 1970.

- [90] A. Bianconi, S. B. M. Hagström, and R. Z. Bachrach. Photoemission studies of graphite high-energy conduction-band and valence-band states using soft-x-ray synchrotron radiation excitation. *Phys. Rev. B*, 16(12):5543–5548, 1977.
- [91] R. Ahuja, S. Auluck, J. M. Wills, M. Alouani, B. Johansson, and O. Eriksson. Optical properties of graphite from first-principles calculations. *Physical Review B*, 55(8):4999–5005, 1997.
- [92] F.-L. Shyu and M.-F. Lin. Plasmons and optical properties of semimetal graphite. *Journal of the Physical Society of Japan*, 69(12):3781–3784, 2000.
- [93] K. Ertel, U. Khol, J. Lehmann, M. Merschof, W. Pfeiffer, A. Thon, and G. Gerber. Time-resolved two-photon photoemission spectroscopy of hopg and ag nanoparticles on hopg. *Appl. Phys. B*, 68:439–445, 1999.
- [94] M. Breusing, C. Ropers, and T. Elsaesser. Ultrafast carrier dynamics in graphite. *Phys. Rev. Lett.*, 102(086809), 2009.
- [95] D. Strickland and G. Mourou. Compression of amplified chirped optical pulses. *Optics Communications*, 55(6):447–449, 1985.
- [96] P. K. Bates. *Optical Parametric Chirped Pulse Amplification in the Few-Cycle Regime*. PhD thesis, Imperial College London, 2008.
- [97] J. S. Robinson. *The Generation and Application of Intense Few-Cycle Laser Pulses*. PhD thesis, Imperial College London, 2006.
- [98] J.S. Robinson, C.A. Haworth, H. Teng, R. A. Smith, J. P. Marangos, and J. W. G. Tisch. The generation of intense transform-limited laser pulses with tunable duration from 6 to 30fs in a differentially pumped hollow fibre. *Appl. Phys. B.*, 85:525–529, 2006.

- [99] A. Suda, M. Hatayama, K. Nagasaka, and K. Midorikawa. Generation of sub 10 fs 5mj optical pulses using a hollow fiber with a pressure gradient. *Applied Physics Letters*, 86(111116), 2005.
- [100] C.-G. Whalstrom, J. Larsson, A. Persson, T. Starczewski, S. Svanberg, P. Salieres, Ph. Balcou, and A. L’Huillier. High-order harmonic generation in rare gases with an intense short-pulse laser. *Phys. Rev. A*, 48(6): 4709–4720, 1993.
- [101] Scientific and Technical Databases. <http://www.nist.gov/srd/index.htm>. *National Institute of Standards and Technology (NIST)*, 2008.
- [102] W. C. Wiley and I. H. McLaren. Time-of-flight mass spectrometer with improved resolution. *Rev. Sci. Instrum.*, 26(12):1150–1157, 1955.
- [103] E. de Hoffmann and V. Stroobant. *Mass Spectrometry*. Wiley-Interscience, 2007.
- [104] Kore Technology. *Operating Manual Kore Ion Detection Components*, 2005.
- [105] M. Lenner, A. Kaplan, and R. E. Palmer. Nanoscopic coulomb explosion in ultrafast graphite ablation. *Applied Physics Letters*, 90(15):153119, 2007.
- [106] A. Kaplan, M. Lenner, and R. E. Palmer. Emission of ions and charged clusters due to impulsive coulomb explosion in ultrafast laser ablation of graphite. *Phys. Rev. B*, 76(073401), 2007.
- [107] G. Mainfray and C. Manus. Multiphoton ionization of atoms. *Reports on Progress in Physics*, 54:1333–1372, 1991.
- [108] J. H. Eberly, J. Javanainen, and K. Rzazewski. Above-threshold ionization. *Phys. Rep.*, 204(5):331–383, 1991.
- [109] K. Varju, P. Johnsson, J. Mauritsson, T. Remetter, T. Ruchon, Y. Ni, L. Lepine, M. Kling, K. J. Schafer, M. J. J. Vrakking, and A. L’Huillier. Angularly

- resolved electron wave packet interferences. *J. Phys. B: At. Mol. Opt. Phys.*, 39:3983–3991, 2006.
- [110] J. W. McClure. Energy band structure of graphite. *IBM Journal*, page 255, July 1964.
- [111] A. R. Law, J. J. Barry, and H. P. Hughes. Angle-resolved photoemission and secondary electron emission from single-crystal graphite. *Phys. Rev. B.*, 28(9):5332–5335, 1983.
- [112] R. F. Willis, B. Fitton, and G. S. Painter. Secondary-electron emission spectroscopy and the observation of high-energy excited states in graphite: Theory and experiment. *Phys. Rev. B*, 9(4), 1974.
- [113] S. Samarin, O. M. Artamonov, A. D. Segeant, and J. F. Williams. Secondary emission from w(110) excited by spin-polarized electrons. *Surface Science*, 579(2-3):166–174, 2005.
- [114] W. Schülke, U. Bonse, H. Nagasawa, A. Kaprolat, and A. Berthold. Interband transitions and core excitation in highly oriented pyrolytic graphite studied by inelastic synchrotron x-ray scattering: Band-structure information. *Phys. Rev. B*, 38(3):2112–2123, 1988.
- [115] J. G. Fujimoto, J. M. Liu, E. P. Ippen, and N. Bloembergen. Femtosecond laser interaction with metallic tungsten and nonequilibrium electron and lattice temperatures. *Phys. Rev. Lett.*, 53(19):1837–1840, 1984.
- [116] S. Passlack, S. Mathias, O. Andreyev, D. Mittnacht, M. Aeschlimann, and M. Bauer. Space charge effects in photoemission with a low repetition, high intensity femtosecond laser source. *Journal of Applied Physics*, 100(024912), 2006.

- [117] S. Hellmann, K. Rosnagel, M. Marczyński-Buhlow, and L. Kipp. Vacuum space-charge effects in solid-state photoemission. *Phys. Rev. B*, 79(035402), 2009.
- [118] J. P. Barbour, W. W. Dolan, J. K. Trolan, E. E. Martin, and W. P. Dyke. Space-charge effects in field emission. *Physical Review*, 92(1):45–51, 1953.
- [119] Francesco Banfi, Claudio Giannetti, Gabriele Ferrini, Gianluca Galimberti, Stefania Pagliara, Daniele Fausti, and Fulvio Parmigiani. Experimental evidence of above-threshold photoemission in solids. *Phys. Rev. Lett.*, 94(037601), 2005.
- [120] F. H. M. Faisal and J. Z. Kaminski. Floquet-bloch theory of photoeffect in intense laser fields. *Phys. Rev. A*, 58(1):R19–R22, 1998.
- [121] M. Wegener. *Extreme Nonlinear Optics in Semiconductors (Optics of Semiconductors and Their Nanostructures Eds. H. Kalt and M. Hetterich)*. Springer, 2004.
- [122] M. Berndt, M. Rohmer, B. Ashall, C. Schneider, M. Aeschlimann, and D. Zerulla. Polarisation selective near-field focusing on mesoscopic surface patterns with threefold symmetry measured with peem. *Optics Letters*, 34(7):959–961, 2009.
- [123] F. Bisio, M. Nyvlt, J. Franta, H. Petek, and J. Kirschner. Mechanisms of high-order perturbative photoemission from cu(001). *Phys. Rev. Lett.*, 96(8):087601, 2006.
- [124] M. Wolf, A. Hotzel, E. Knoesel, and D. Velic. Direct and indirect excitation mechanisms in two-photon photoemission spectroscopy of cu(111) and co/cu(111). *Phys. Rev. B*, 59(8):5926, 1999.
- [125] T. Plakhotnik. Optical bloch equations and enhanced decay of rabi oscillations in strong driving fields. *Chemical Physics*, 321:337–340, 2006.

- [126] John Weiner and P.-T. Ho. *Light-Matter Interaction*, volume 1. John Wiley and Sons, 2007.
- [127] N. E. Karatzas A. T. Georges. Modeling of ultrafast interferometric three-photon photoemission from a metal surface irradiated with sub-10-fs laser pulses. *Physical Review B*, 77(085436), 2008.
- [128] R. Loudon. *The Quantum Theory of Light 2nd edition*. Oxford University Press, 1984 (reprint).
- [129] J.P. Gauyacq and A.K. Kazansky. Modelling of interferometric multiphoton photoemission. *Applied Physics A*, 89:517–523, 2007.
- [130] J. R. Ackerhalt and B. W. Shore. Rate equations versus Bloch equations in multiphoton ionization. *Phys. Rev. A*, 16(1):277–282, 1977.
- [131] J.-C. Diels, J. Stone, S. Besnainou, M. F. Goodman, and E. Thiele. Probing the phase coherence time of multiphoton excited molecules. *Optics Communications*, 37(1):11–14, 1981.
- [132] D. W. Chandler and P. L. Houston. Two-dimensional imaging of state-selected photodissociation products detected by multiphoton ionization. *J. Chem. Phys.*, 87(2):1445, 1987.
- [133] A. J. R. Heck and D. W. Chandler. Imaging techniques for the study of chemical reaction dynamics. *Annu. Rev. Phys. Chem.*, 46:335–372, 1995.
- [134] A. T. J. B. Eppink and D. H. Parker. Velocity map imaging of ions and electrons using electrostatic lenses: Application in photoelectron and photofragment ion imaging of molecular oxygen. *Rev. Sci. Instrum.*, 68(9):3477, 1997.
- [135] B. Whitaker, editor. *Imaging in Molecular Dynamics: Technology and Applications*. Cambridge University Press, 2003.

- [136] T. Kitsopoulos, C. R. Gebhardt, and T. P. Rakitzis. Photodissociation study of cs_2 at 193nm using slice imaging. *J. Chem. Phys.*, 115(21):9727–9732, 2001.
- [137] C. R. Gebhardt, T. P. Rakitzis, P. C. Samartzis, V. Ladopoulos, and T. N. Kitsopoulos. Slice imaging: A new approach to ion imaging and velocity mapping. *Rev. Sci. Instrum.*, 72(10):3848, 2001.
- [138] D. Townsend, M. P. Minitti, and A. G. Suits. Direct current slice imaging. *Rev. Sci. Instrum.*, 74(4):2530, 2003.
- [139] M. N. R. Ashford, N.H. Nahler, A. J. Orr-Ewing, O. P. J. Vieuxmaire, R. L. Toomes, T. N. Kitsopoulos, I. A. Garcia, D. A. Chestakov, S-M. Wu, and D. H. Parker. Imaging the dynamics of gas phase reactions. *Physical Chemistry Chemical Physics*, 8:26–53, 2006.
- [140] Stefan Kaesdorf. *Manual Velocity Mapping Instrument VMI1*. Stefan Kaesdorf, 2007.
- [141] B. Baguenard, J. B. Wills, F. Pagliarulo, F. Lépine, B. Climen, M. Barbaire, C. Clavier, M. A. Lebeault, and C. Bordas. Velocity-map imaging electron spectrometer with time resolution. *Rev. Sci. Instrum.*, 75(2):324, 2004.
- [142] A. Hoffman, G. L. Nyberg, and S. Prawer. High-energy angle-resolved secondary-electron emission spectroscopy of highly oriented pyrolytic graphite. *J. Phys.:Condens. Matter*, 2:8099–8106, 1990.